ORIENTATION DYNAMICS OF CHIRAL LIQUID CRYSTALLINE DISPERSIONS DURING PROCESSING

A Dissertation

by

MARTIN JOSEPH POSPISIL

Submitted to the Office of Graduate and Professional Studies of
Texas A&M University
in partial fulfillment of the requirements for the degree of

DOCTOR OF PHILOSOPHY

Chair of Committee,	Micah J. Green
Committee Members,	Zhengdong Cheng
	Mohammad Naraghi
	Hung-Jen Wu
Head of Department,	M. Nazmul Karim

August 2019

Major Subject: Chemical Engineering

ABSTRACT

Lyotropic chiral nematic liquid crystalline dispersions are a unique state of matter that can be exploited to create materials with directionally dependent optical properties. Because of their unique ability to undergo a phase transition and self-assemble into a helical microstructures, chiral nematic dispersions remain a model system in which fluid phase processing can be studied. They also have great potential for industrial applications since they are capable of being processed into thin films that rotate circularly polarized light for optical sensing, security encryption, and decorative coating applications. However, many challenges remain due to complex rheological behavior and consistency in mesogen properties during preparation.

In this dissertation, various aspects of processing liquid crystalline dispersions are investigated. Both external processing parameters and material parameters are explored and compared to their experimental counterparts. Confinement effects were discovered to greatly influence the orientation of the chiral microstructure in initially shear aligned dispersions. Chiral strength also altered the orientation of helical microstructures and the number of defects present in these initially shear aligned dispersions. The most uniform homeotropic helical microstructures were achieved at low chiral strength values and the tightest confinement applied by the shear apparatus. Surface anchoring, concentration, speed of drying and chiral strength were also studied in chiral liquid crystalline dispersions as they were made into optically active thin films. For these purposes, large

uniform areas of planar microstructures are desired for selective reflection applications. It was determined experimentally that biphasic dispersions formed the most uniform planar configurations when dried slowly in humid environments when placed between two anchoring surfaces. The computational work in this thesis also confirmed these results. The model was also able to show that the number of defects in the films was highly sensitive to the value of chiral strength, which generated more defects at larger values.

This work serves as a basis for comparison between lab-scale experiments and their respective theoretical simulations, and paves the way for future collaborative efforts to develop thin films for practical applications.

ACKNOWLEDGEMENTS

First and foremost, I would like to thank my advisor, Dr. Micah J. Green, for all the wisdom, encouragement, and guidance that he provided throughout this project. Your patience and understanding was unmatched in our afternoon meetings and I can't thank you enough for convincing me that the sky was not falling no matter how pessimistic I was. I also want to thank you for helping me establish a work-life balance and continually being flexible for all the personal issues that came up.

To my committee, thank you for the extra insight into my project and bearing through the committee meetings and this dissertation with me.

I also must thank many of my fellow graduate students in the department for helping me though the past four and a half years with the constant support and camaraderie. Special thanks goes to Jon, Jacob, Josh, Touseef, Smit, Dorsa, Melanie, Katie, Marc, and Alex. Without you guys, the time spent here would not have been as enjoyable.

Additional thanks goes to the Davis group from Auburn University. Without you guys this would not have been possible. To Dr. Virginia A. Davis, thank you for always questioning my ideas and always reminding that there is a complicated world outside of my models. To Zan, Partha, and Matt, thank you guys for all your great work and friendship. Conferences wouldn't have been the same without you.

To the Green group and all of our wonderful undergraduates, thank you for all the stimulating discussions and all of your contributions. I cannot express how helpful you guys were over the years especially listening to me go over the models constantly. I also want to thank our wonderful post-docs, Wanmei, Taruna, and Aniruddh, for your insight throughout the Ph.D. process.

I would also like to thank my undergraduate roommates, Brice, Aaron, and Collin for all the support and love this past semester. It takes a lot to put up with an old man like me. Best of luck to all of you in the future.

To my family, we did it. Thank you so much for all the love and support both financially and mentally. You guys mean the world to me and I couldn't have done it without you. You guys always had my back and pushed me to never quit.

To Ashton, you have seen it all, the ups and the downs. You never gave up trying to make me feel better when I hit a dead end in my research. I always appreciated how you tried to get me out of my mood and out of the house. Thank you for helping me realize there is more in this life than just work. I can't express how great you've been with your constant love and support.

CONTRIBUTORS AND FUNDING SOURCES

Contributors

This work was supervised by a dissertation committee consisting of Dr. Micah J. Green (advisor), Dr. Zhengdong Cheng, Dr. Hung-Jen Wu from the Artie McFerrin Department of Chemical Engineering, and Dr. Mohammad Naraghi from the Department of Aerospace Engineering.

Experimental results presented in this dissertation (Chapters 5 and 6) were provided by Dr. Virginia A. Davis' group at Auburn University; this data is marked appropriately. All simulation work conducted for this dissertation was completed independently by the student. The simulations in this thesis were completed using computing resources provided by the Texas A&M High Performance Research Computing (HPRC).

Funding Sources

Graduate study was supported by the National Science Foundation through-collaborative research grants CBET 1436637 and 1437073. Experimental work was funded in part by the Department of Education Graduate Assistantship in Area of National Need P2000A120228 and IGERT DGE 1069004.

TABLE OF CONTENTS

Page

LIST OF FIGURES

Page

CHAPTER I

INTRODUCTION

1.1 Motivation

Controllable orientation of anisotropic nanomaterials in smart composites and thin films has become a focal point of experimental and computational research in recent decades. These materials appear in everyday products and have led to increased electrical, thermal, and optical physical properties as well as mechanical strength and toughness. The process in which nanomaterials are organized into these films and composites often depends on the macroscopic application and typically requires specific orientation for improved properties. The generation of these novel materials is difficult due to the complexity of preferentially aligning nanoscale materials using macroscopic mechanisms such as fluid phase processing. Challenges in this industrially cost effective method stem from complex rheological phase behavior and colloidal stability on the macro scale due to interacting electrostatic behavior, thermal fluctuations, mechanical stress, and thermodynamically driven self-assembly.

The liquid crystalline phase is often regarded as the optimal intermediate state of matter used in the production of these smart products because they exhibits both fluidity and crystalline properties. Since their debut in the development of flat panel electronic

displays in the early 1960's, liquid crystalline systems have been an area of increased industrial and academic research.

Current literature has shown many potential applications of liquid crystals due to their unique abilities. These applications include but not limited to: mirrorless lasing, security encryption, and decorative coatings. [1-5] It has already been shown that composites made from liquid crystalline dispersions have been used in humidity sensors, tissue scaffolds, and shape memory polymers. .[6-8] However, non-uniformities continue to plague the manufacturing steps. These inconsistencies often lead to less desirable mechanical and optical properties in the final product. To combat these issues, many experimentalists rely on trial and error studies to gain empirical knowledge which lacks fundamental understanding of the physics. These methods, while successful, only aid in solving a particular system with set parameters and properties. If the system was to change, (i.e. contain different properties or different anisotropic nanomaterials) the same techniques could prove to be ineffective. It therefore becomes necessary to develop models derived from first principles to capture the effects seen in experiments so that correlations between microstructure and experimental parameters can be established. These correlations would limit the need for trial and error experiments, saving money, time, and allow for a universal methodology to be applied to many liquid crystalline systems.

1.2 Goals and Outline of the Dissertation

The aim of this this thesis is to explore the effects of processing parameters on the final microstructure of a self-assembling chiral liquid crystalline dispersion. The industrially relevant focus is on the exploitation of the unique optical properties exhibited by these dispersions for thin film technologies. This is made possible through the use of the dynamic Landau-de Gennes equation for chiral liquid crystals. The novelty of this work lies in the experimental validation of the theoretical claims made by these models and their use as predictive tools for further investigation of anisotropic systems. This thesis is organized as follows: Chapter 2 begins with an introduction into the basics of liquid crystals and their rheological behavior. Chapter 3 introduces the reader to the current and early theoretical models used to predict nanoscale behavior in liquid crystalline systems. Chapters 4 details the methods used to visualize the simulation results. Chapters 5-6 highlight different behavior caused by various processing parameters. Finally, Chapter 7 summarizes the takeaways from the previous results and suggests future work that will follow the work presented in this thesis.

1.2.1 Chapter II

Chapter 2 introduces the reader to the basics of liquid crystalline nomenclature by defining the different types of liquid crystalline dispersions based on the intensive parameters that induce the phase behavior. Next, the dispersions are further classified by

their mesogen ordering. A brief discussion of rheological behavior follows the introduction and highlights correlations between orientation and dispersion viscosity. The effects of dispersion concentration and microstructure seen within chiral liquid crystals is also mentioned. The remainder of Chapter 2 is dedicated the specifics of chiral liquid crystals. This includes the definition of chirality, helical pitch and the classification of helical configurations. The final sections of this chapter are dedicated to the specific system that was studied for this dissertation and explains how the anisotropic nanomaterial is manufactured and lists its nanoscale properties.

.

1.2.2 Chapter III

Chapter 3 outlines the previous theoretical treatments of nematic lyotropic liquid crystals and forms the basis for the work used in the subsequent chapters. These early models are derived from free energy and utilize relationships between thermodynamic entropy and structural elasticity. A brief mention of the features and shortcomings of each model is included. Chapter 3 finally concludes with a full derivation of the Landau-de Gennes model used throughout the rest of this work.

1.2.3 Chapter IV

Chapter 4 highlights the software used in solving the Landau-de Gennes model and illustrates how the modeling results can be visualized and compared to experimental

results. This chapter also provides the equations and explanation needed to develop the visualization maps.

1.2.4 Chapter V

Chapter 5 focuses on dispersion dynamics where shear relaxation experiments were conducted and modeled with the Landau-de Gennes formulation. The aim of this chapter is to highlight how different experimental parameters affect the equilibrium microstructure in liquid crystalline dispersion. Confinement effects were studied first and compared to experimental results that were generated using a Linkam shear cell and a Nikon cross-polarizing microscope. Results indicate that equilibrium helical configurations are heavily influenced by the proximity of the boundaries relative to each other. This is because dispersions above the critical liquid crystalline phase concentration exhibit strong elastic effects which compete against each other in the system. In order to minimize the free energy due to these large gradients, certain orientations become preferable. Next, chiral strength was studied under constant external confinement. Similar to the previous study, this study also exhibited different microstructural configurations based on the value of chiral strength. Finally, we show the development of helical microstructures using our dynamic model. We capture the formation of helical microstructures from a shear aligned state within the shear bands seen in experiments. We conclude that both confinement and chiral strength can be

treated as mutually exclusive, and that helical microstructure can be altered by influencing either of them.

1.2.5 Chapter VI

Chapter 6 focuses on the helical microstructures that develop in the gelation and drying of thin films. The goal of this work was to generate large uniform domains of planar helical microstructures for selective reflection applications. In addition to the Landau de Gennes model, we incorporated a mass transfer equation, and a differential height equation to study the dynamics of mesogen self-assembly. Our study focused on the effects of initial concentration, chiral strength, surface anchoring, speed of drying, and influence of initial shear alignment. Computational results were directly compared to previous experimental results. Conclusions in the experimental work verified the model, and it was found in both the experiment and the model that initially biphasic dispersions with no initial shear alignment generated the largest uniform planar domains when dried slowly with increased surface anchoring.

1.2.6 Chapter VII

Chapter 7 contains a summary of the work and results presented in this thesis. Based on the results presented, a few broad concepts related to controlling the self-assembly are

made. Finally, ideas related to the continued study of microstructure formation in chiral liquid crystalline dispersions for thin film production are described.

CHAPTER II

LIQUID CRYSTALS AND CELLULOSE NANOCRYSTALS

2.1 Introduction & Background

Liquid crystals are a special state of matter first discovered by Friedrich Reinitzer in 1888. Reinitzer's, interest was in the physicochemical properties of cholesterol derivatives, observed that cholesteryl benzoate had two melting points. Upon reaching the first melting point, a cloudy liquid formed. After continued heating, the cloudy liquid melted into a transparent liquid.[9] It was later found by Otto Lehmann, Reinitzer's colleague, that the intermediate "cloudy" liquid had crystalline properties and sustained flow. Lehmann later coined the term "liquid crystal" due to their fluidity and crystalline properties.[10] It has since been determined that, these systems are composed of constituents (mesogens) that are dispersed in a solvent, have large aspect ratios, and form anisotropic regions during a phase transition. The hierarchical ordering of these systems into anisotropic regions directly correlates to the exhibited macroscopic properties, and makes them interesting systems to study for industrial applications and academic inquiry.

2.2 Types of Liquid Crystals

Liquid crystals can be divided into three subgroups: thermotropic, lyotropic, and metallotropic. Each subgroup's phase transition is triggered by different system properties.

Thermotropic and lyotropic liquid crystals are composed of organic molecules that phase transition at critical temperatures and critical concentrations respectively. Metallotropic liquid crystals, on the other hand, are composed of organic and inorganic molecules that phase transition at a critical composition ratio. For the purpose of this thesis, we will focus exclusively on lyotropic liquid crystalline systems.

At low mesogen concentration, lyotropic liquid crystalline systems behave isotropically which means that the system does not exhibit any directionally dependent properties. As mesogen concentration is increased via the addition of more mesogen or evaporation of solvent (usually water), these dispersions shift into the biphasic regime in which both isotropic and local anisotropic phases coexist. For lyotropic systems, these newly formed anisotropic domains continue to grow and fuse as the mesogen concentration increases leading to a larger anisotropic volume fraction. At high enough concentrations, the equilibrium of the two phases shifts completely towards the anisotropic phase and the system is considered to be fully liquid crystalline. (See **Figure 2.1** for detailed schematic).

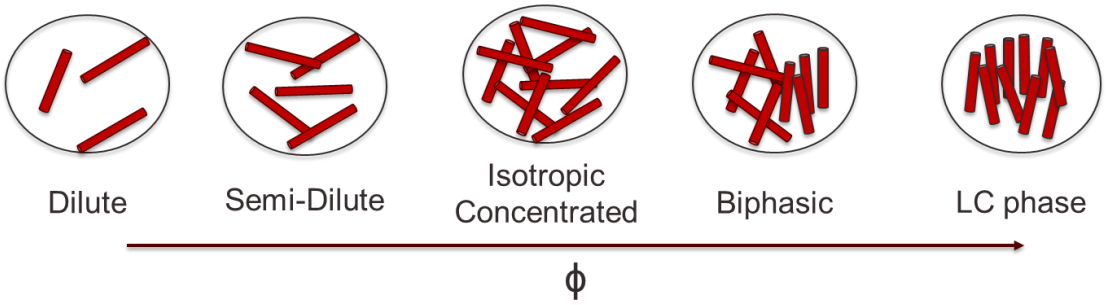

Figure 2.1: Schematic showing alignment of mesogen as a function of concentration

This entropic phenomenon is best elucidated by Onsager's the early work in which a relationship between orientational ordering to the anisotropic shape of rods was established.[11] His work derived a free energy functional to illustrate the competition between entropy and excluded volume. Chapter 2 has a detailed explanation of this work, but in summary, Onsager argued that as rotational entropy of the system decreased due to excluded volume effects, translational entropy increased to maximize the total entropy of the system, leading to an ordered state.[12] In reference to **Figure 2.1**, this theory explains that at low concentrations the rods are free to rotate but as concentration increases the molecules lose orientation space since no two molecules can intersect, leading to an ordered phase. Later work by Doi also explains the same phenomenon using a diffusion equation.[13] In his dynamic formulation, the orientation of molecules is represented by a probability distribution, *f*. For a system in which diffusion is the only driving force, higher order shift towards lower order to maximize the entropy. As a result, only isotropic systems would exist as the ordered states would disassemble. Physically, we know from Onsager's work that excluded volume effects force an ordered state. In light of this, Doi incorporates a mean field potential that captured the excluded volume effect. This term

competes with the diffusive force by "concentrating" the orientation so that the system remains ordered. The strength of this mean field potential is determined by the rod number density within the system. A high rod number density corresponds to a high potential and is therefore more ordered and vice versa for a low rod density.

Structure-property relationships of these lyotropic dispersions are most sensitive within the biphasic and liquid crystalline regimes to such a degree that minor changes in concentration or thermal fluctuations can cause radically different properties. This is due to the intricacies of the domain fusion process which is dependent on the surface tension of individual anisotropic domains. Incomplete fusion of the anisotropic domains cause local defects in the system which can serve as stress points in the material and may alter many of the properties including but not limited to: thermal and electrical conductivity, rheological properties, and both transmittive and reflective optical properties.[14]

2.3 Long Range Ordering

Liquid crystalline systems can also be classified by their long-range ordering. This long range ordering is heavily dependent on mesogen shape, intermolecular interaction, and charge. **Figure 2.2** depicts the different types of long range order commonly found in liquid crystalline systems and indicates the direction of the average orientational order via the director, ***n***.

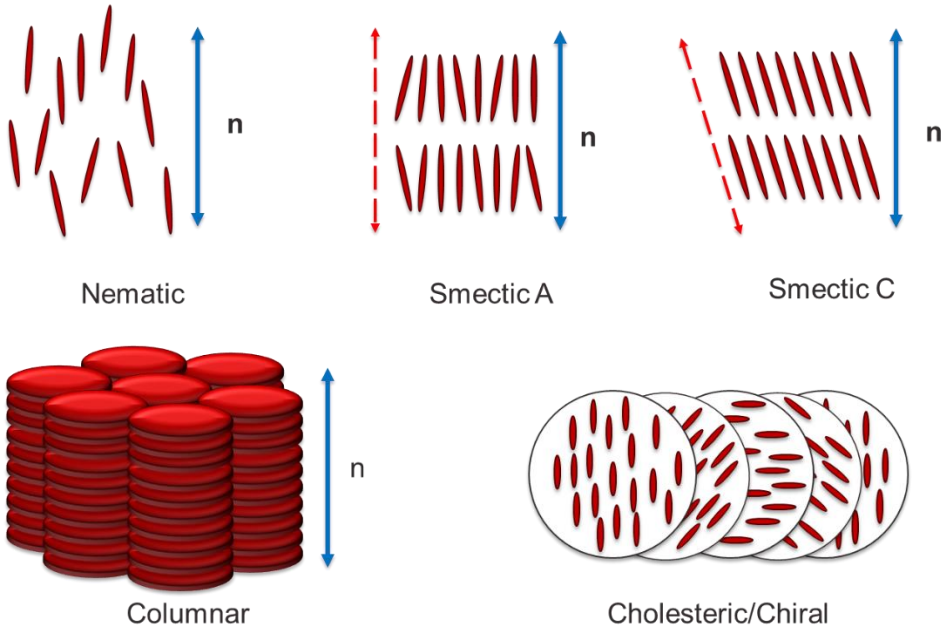

Figure 2.2: Schematic showing the ordered configurations found in liquid crystals

Columnar liquid crystals are the most ordered liquid crystalline phase and possess 2D positional order.[15] They are typically formed by disc-shaped mesogens or rod-like mesogens that have formed a micellar microstructure.[16] The molecular structure of these mesogens include large aromatic regions similar to carbonized graphitic substances or similar aromatic structures. The self-organization of these mesogens is a result of the steric packing due to entropy and the electrostatic interaction known as π-π stacking. Smectics (smectic-A and smectic-C are the most common) represent the next highest order as these systems exhibit a 1D positional order.[17] Mesogens present in this liquid crystalline phase align into distinct planes and have more translational motion than the columnar liquid crystals because individual planes are able slide past each other. Because the applications of these ordered systems are so widely known, the mesogens that follow this ordering are

also called smectogens.[18] Unlike the columnar liquid crystal mesogens, smectogens are not confined to one particular molecular shape. There is a wide variety of molecular templates that have been shown to support the smectic phase including bent, bowlic, cross shaped and even pyramidal.[18] While there are many different molecules that are able to form this type of ordered liquid crystal, the traditional smectogen constitutes a linear core with peripheral side groups.[18] The exact spacing and orientation of these side groups as well as the geometry of the molecule determines the type of smectic that is formed. Lastly, the nematic liquid crystals represent the least ordered form of the liquid crystalline phase and have no positional order, only orientational order.[15] This level of ordering is the classical hard rod system that has been extensively studied in recent years. Traditionally, mesogens that develop into this type of liquid crystal ordering can be of any anisotropic shape and are structurally rigid, but there are exceptions.[19] Another subset within this group of ordering are cholesteric or chiral liquid crystals. Columnar liquid crystals are capable of forming chiral structures, but for the purpose of this thesis we will focus on chiral systems formed by traditional nematic-like mesogens. Systems of this nature are often labeled as chiral nematics. These special subsystems develop nematic planes that self-assembly into helical microstructures giving them interesting optical and mechanical properties.

2.4 Rheological Behavior of Liquid Crystalline Dispersions

In continuum mechanics, there are two classifications of fluids, Newtonian and non-Newtonian. Newtonian fluids are characterized by a linear relationship between viscous stress due to flow and the local strain rate at every point (**Figure 2.3**).[20] This relationship is given by $\tau = -\eta\dot{\gamma}$ where η is a constant viscosity with respect to the shear rate $\dot{\gamma}$. This relationship can also be written in tenor notation as:

$$\tau_{ij} = \eta(\frac{\partial v_i}{\partial x_j} + \frac{\partial v_j}{\partial x_i}). \qquad 0\text{-}1$$

where v_i is the i^{th} component of the velocity and x_i is the i-coordinate. Common examples of Newtonian fluids include water, alcohol and air.

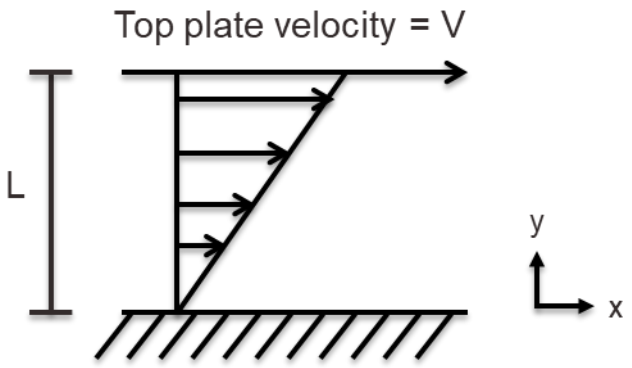

Figure 2.3: Schematic of simple shear for a Newtonian Fluid

In contrast, polymeric solutions, paints, and more importantly, liquid crystalline dispersions behave as non-Newtonian fluids. These fluids do not to have a linear relationship between viscous stress and shear rate (η is allowed to increase or decrease). In the case of liquid crystals, viscosity actually decreases with increasing shear rate classifying them as shear-thinning solutions. Non-Newtonian fluids also have nonzero first and second normal stress differences unlike their Newtonian counterparts.

$$\tau_{xx} - \tau_{yy} \equiv \Phi_1 \dot{\gamma}^2 \qquad 0\text{-}2$$

$$\tau_{yy} - \tau_{zz} \equiv \Phi_2 \dot{\gamma}^2 \qquad 0\text{-}3$$

Depending on the value of Φ_i, the system will either expand (if positive) or shrink (if negative). This phenomenon is depicted in **Figure 2.4**.

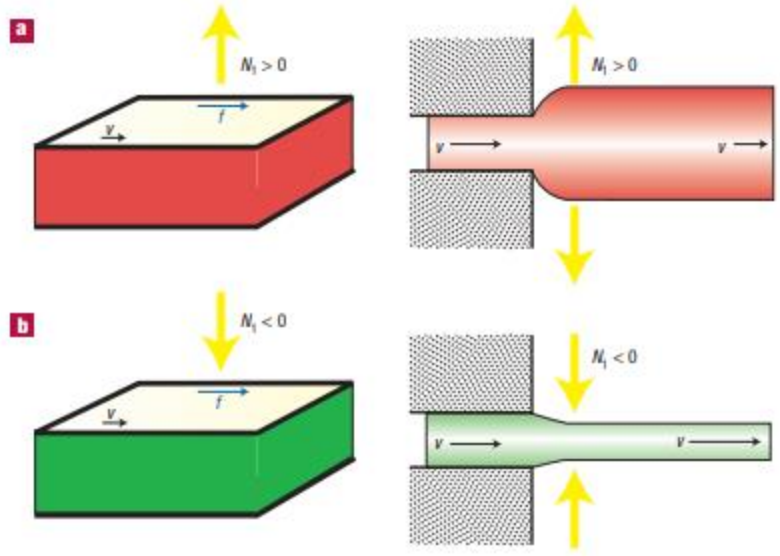

Figure 2.4: Illustration of non-Newtonian fluid behavior depending on the value of the first normal stress difference. (a) Fluid expands once exiting the shear region indicative of a positive normal stress coefficient. (b) Fluid shrinks once exiting the shear region indicative of a negative normal stress coefficient.(Reprinted with permission from Springer Nature: *Nature Materials* 3, 509-510, Swell Properties and swift processing , M. Pasquali, Copyright 2004 Springer Nature)[21]

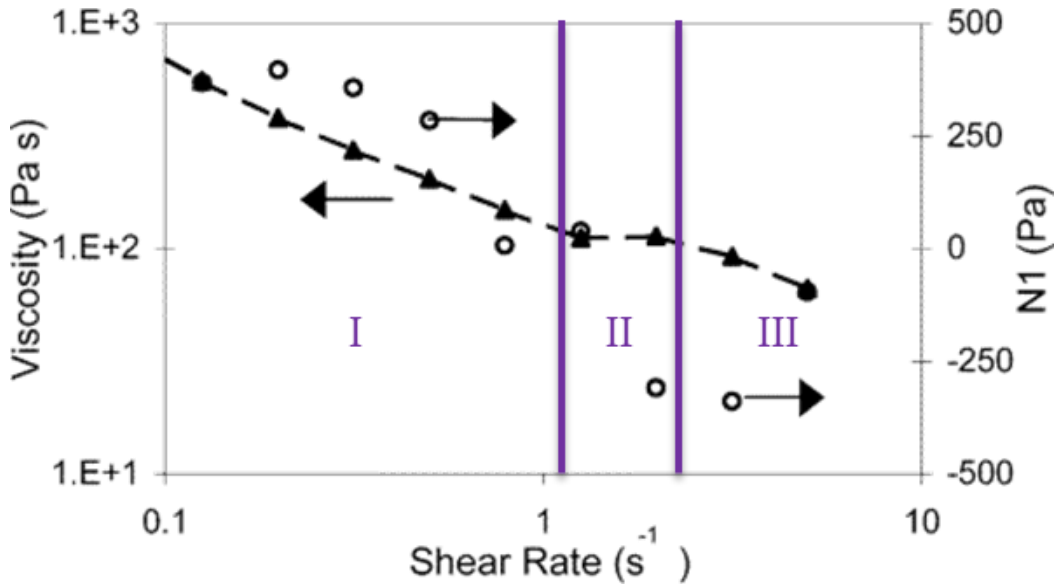

Figure 2.5: Rheological behavior of 4.5 vol% SWNT in superacid liquid crystalline systems. Left axis shows viscosity's nonlinear dependence of shear rate. Right axis shows the normal stress difference that is characteristic of liquid crystals (Adapted with permissions from American Chemical Society: *Macromolecules* 37, 1, 154-160, Phase Behavior and Rheology of SWNTs in Superacids, V. A. Davis, L. M. Ericson, A. N. G. Parra-Vasquez et al. Copyright 2004 American Chemical Society).[22]

Rheological behavior of liquid crystalline systems can be divided into three distinct regions as shown in **Figure 2.5**. The distinction of these regions is still highly controversial and an area of ongoing research, but for the purposes of this discussion we assume them to be valid. We therefore begin this discussion at very low shear rates where liquid crystalline dispersions adhere to an initial shear thinning behavior (Region I). This region has been attributed to the tumbling of mesogens in pure nematics.[23] For chiral nematics, it has been speculated, that this shear thinning behavior is due to polydomains sliding past each other rather than individual mesogen tumbling.[22,24]. At intermediate shear rates, the material viscosity reaches a plateau as the system reaches a transition state (Region II). In

this state, it is postulated that the individual mesogens exhibit a wagging behavior.[25] As the shear rate increases, the system enters the final shear thinning region (Region III) where the individual mesogens flow align.[22,26] This three region behavior is even more elucidated in biphasic systems. Surface tension effects between ordered and disordered domains cause regions of anisotropy to form into spherical droplets at zero shear. At the onset of shear, (Region I) these spherically ordered domains begin to elongate in the direction of flow. Increased shear (Region II) causes the domains to continually elongate and begin to fuse as surface energy penalties decrease. At high enough shear (Region III) all isotropic domains disappear as the anisotropic domains grow, forming a new shear induced metastable nematic state. The appearance of abrupt boundaries known as defects (or disclinations) also diminishes as shear is increased. The loss of defects is also attributed to the shear thinning nature of liquid crystalline systems as the removal of defects indicates more rod alignment leading to decreased viscosity. In addition to the viscosity shown above, the first normal stress difference, plotted as open circles in **Figure 2.5**, also indicates microscopic changes in the material. The negative first normal stress difference (seen just below 1 s^{-1}) is indicative of mesogen tumbling in which the nematic director is allowed to flip head-tail.[27,28] The change in the first normal stress difference from negative to positive seen in Region II is associated with a loss in rotational degrees of freedom as mesogens continue to align. In nematic systems, this change indicates a change in the movement of the mesogen from tumbling to wagging.[22] Finally, in Region III, flow alignment of the mesogens cause the first normal stress to become positive once again.[25,28-30] Chiral nematic systems are unique, as their first normal stress difference shows two

negative minimums, one in the low shear region and the other in the intermediate shear region. The first minimum, seen at low shear rates, has been attributed to the uncoiling of the helical microstructure whereas the second minimum is attributed to director tumbling of individual mesogens.[31]

2.5 Chirality

Chirality is a term that describes geometric entities that are distinguishable from their mirror images and are unable to be superimposed on themselves. Many naturally occurring objects whose length scales vary from molecular levels to macroscopic levels display this property. The human hands represent the most elementary example of chirality and are often used in describing the nature of chiral configurations. For the purposes of this thesis, we limit our discussion of chirality, or handedness, to the axial chirality seen in chiral nematics. The axial chirality exhibited by chiral nematic systems is caused by one of two conditions related to the electrostatics. The first condition applies to mesogens that have inherent broken charge symmetry caused by charge distribution or side chain arrangement along the individual molecules.[32] The second condition is when a chiral dopant is introduced into an otherwise achiral system.[33] In these cases, the dopant has an affinity for binding, usually through van der Waals forces, to the mesogen in such a way that the chiral dopant now displays the electrostatic symmetry breaking characteristic that causes the formation of the helical microstructure. In order to reduce the free energy contribution for the electrostatic interactions caused by these conditions the nematic layers subsequently

offset by a constant angle of rotation. The way in which this angle of rotation is propagated, i.e. clockwise or counterclockwise, through the sample determines the handedness of the microstructure and ultimately how circularly polarized light will interact with the material as seen in **Figure 2.6**.

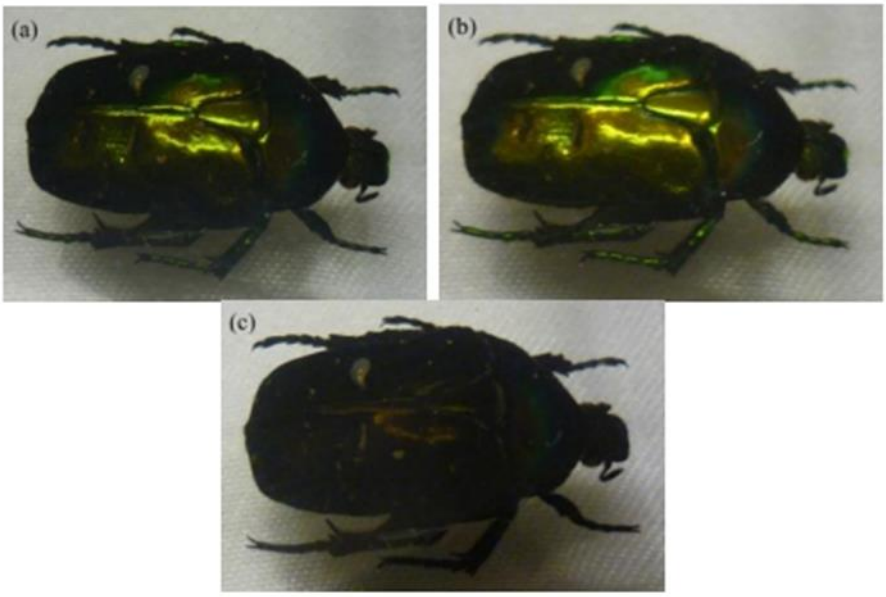

Figure 2.6: (a) A beetle selectively reflecting light due to the macroscopic chiral (left-handed) superstructure within its exoskeleton. (b) Reflection of left-circularly polarized light. (c) Reflection of right-circularly polarized light. Since chiral structure is left-handed beetle can only reflect back light of the same handedness, all else is absorbed. (Reprinted under the terms and conditions of the Creative Commons Attribution license. MDPI: *Symmetry* 6(2) 444-472, Chiral Liquid Crystals: Structures, Phases, Effects, I. Dierking Copyright 2014)[33]

In a pure substance, this microstructure dominates the entire system forcing all anisotropic regions to exhibit the same properties. In a mixture, different concentrations of the enantiomeric structures cause the overall system to exhibit different properties. It has been

shown experimentally that particular compositions of left-handed and right-handed cholesteric dispersions can even behave as purely nematic.[34] It has also been shown that temperature can alter the handedness of chiral systems. This phenomenon is known as the cholesteric twist inversion and is common in mixtures with different components, but has also been shown to occur in systems with a single chiral component.[35-39] Equally important to the chiral orientation, is the characteristic length scale known as the pitch, P, which is defined as the distance that encompasses a full rotation of the nematic director through the helical microstructure. **Figure 2.7** serves as a schematic illustration for defining the chiral pitch.

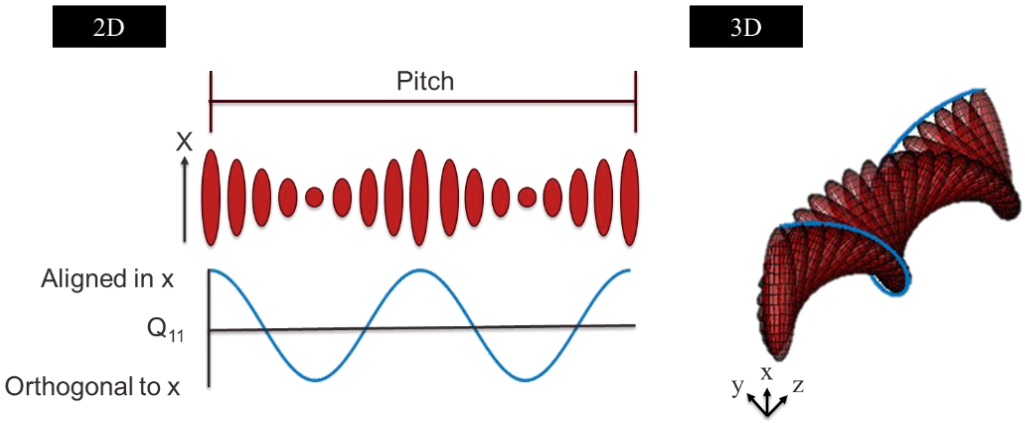

Figure 2.7: This schematic shows the rotation of the mesogen in a chiral system. The pitch is defined as the length required for a full rotation of the nematic director.

It is this characteristic length scale that determines the wavelength of light that is reflected by these systems and also gives rise to the fingerprint texture seen in cross polarized micrographs of these systems. Many factors influence the pitch length observed in chiral nematic systems. The most prominent ones include the aspect ratio, the ionic strength of the dispersion, the charge distribution along the mesogen or mesogen-dopant compound, the amount of mesogen, and the relative concentration of the dopant. For our purposes, we investigate the processing parameters based on a single component mixture, but work is still ongoing for dopant-mesogen systems.

The orientation of the helical microstructure also has an integral role in material design. There are two kinds of helical orientations that will be discussed further in this work. **Figure 2.8** displays both cases, the homeotropic and planar orientations.

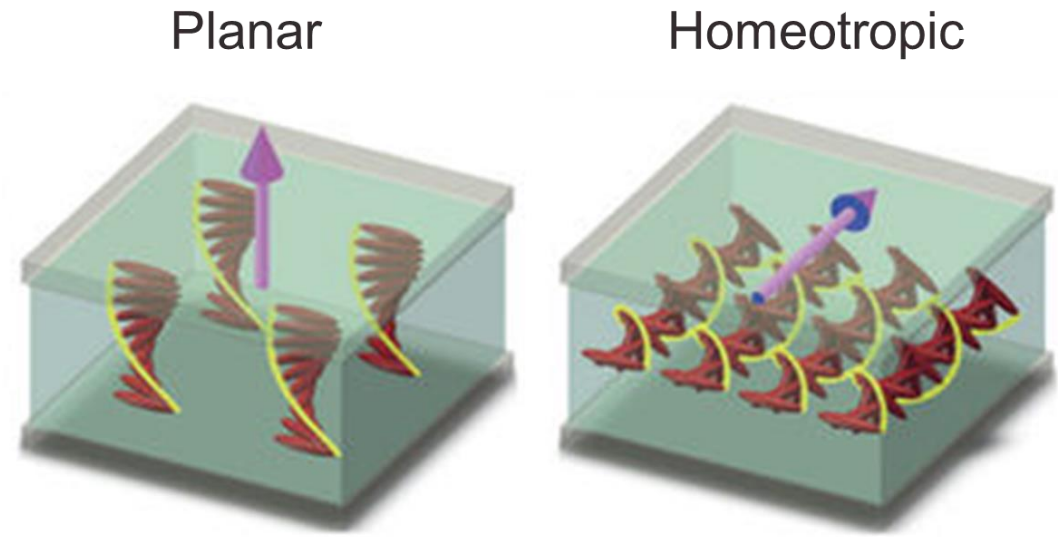

Figure 2.8: Schematic showing two different helical orientations. The planar orientation aligns the helical axis in the direction normal to the major axes of the material. The homeotropic orientation aligns the helical axis in plane of the major axes of the material. (Reprinted by permission from Springer Nature: *Nature* 531 352-356, Three-dimensional control of the helical axis of a chiral nematic liquid crystal by light, Z. Zheng, Y. Li, H. K. Bisoyi, L. Wang, T. J. Bunning et al., Copyright 2016 Springer Nature.[40])

Each orientation stems from either the build direction of other helices, random nucleation points within the sample, or geometric confinement. Due to the frustration induced by these factors defects often form within the liquid crystalline domain (**Figure 2.9**). It is also common to find such defects near the interface of two different helical configurations and or similar helical configurations that have different pitch lengths. Outside factors such as magnetic and electric fields have also been shown to introduce additional frustration into the system causing more defects to form.[41] In either case, the formation of enough defects

can destabilize the helical microstructure enough to generate highly complex 3D structures.

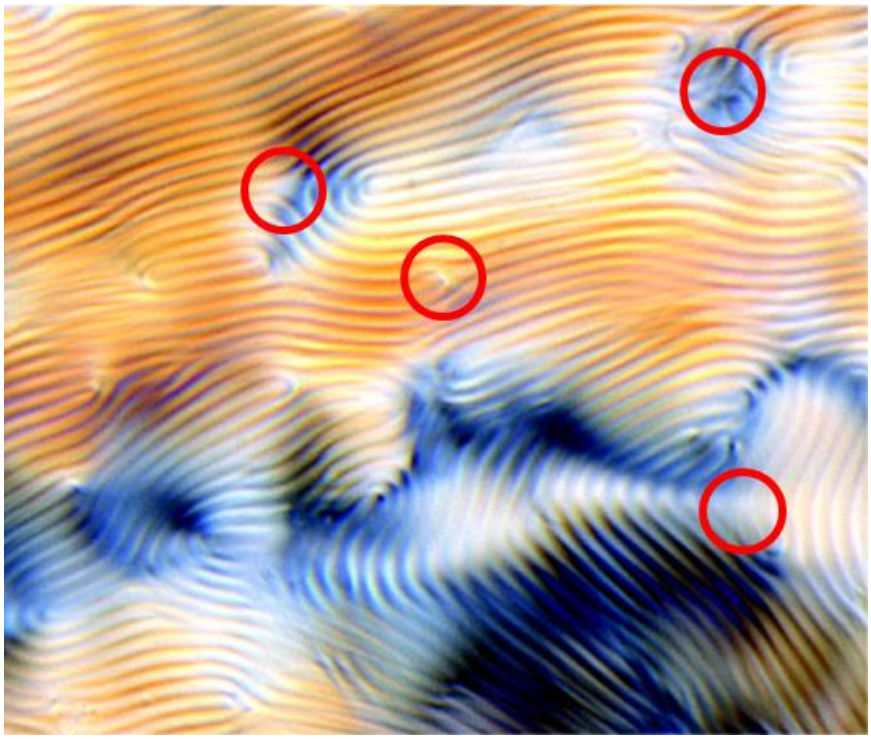

Figure 2.9: Cholesteric liquid crystal displaying defects. (Reprinted under ACS AuthorChoice/Editors' Choice Usage Agreement, *ACS Nano* 5, 2, 1450-1458, Cholesteric and Nematic Liquid Crystalline Phase Behavior of Double-Stranded DNA Stabilized Single-Walled Carbon Nanotube Dispersions, G. Ao, D. Nepal, M.. Aono, V. A. Davis.[42]

2.6 Cellulose Nanocrystals

We have elected to use cellulose nanocrystals (CNCs) as our model mesogen to study lyotropic liquid crystals both in our experiments and our simulations. These charged mesogens spontaneously self-assemble into a left-handed helical microstructures at high mesogen concentrations. These microstructures are responsible for the characteristic fingerprint texture exhibited by chiral nematics when viewed under cross polarizers (See **Figure 2.10**).

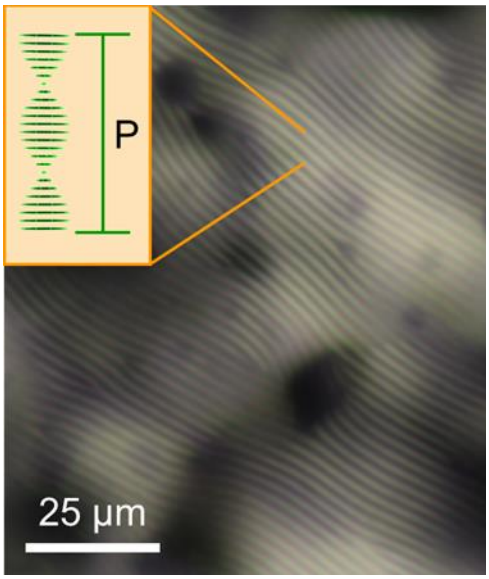

Figure 2.10: Cross-polarized optical micrograph showing cholesteric fingerprint. (Reprinted with permissions from American Chemical Society: *Langmuir* 34, 44, 13274-13282, Orientation Relaxation Dynamics in Cellulose Nanocrystal Dispersions in the Chiral Liquid Crystalline Phase, M. J. Pospisil, P. Saha, S. Abdulquddos, et al. Copyright 2018 American Chemical Society).[43]

Investigation of the natural cellulose feedstocks have shown that cellulose is comprised of both amorphous and crystalline regions[44]. The proportion and size of the crystalline regions depends on the biomass source used and proves to be a critical parameter in the production of CNCs. For our study, the CNCs were formed via sulfuric acid hydrolysis as shown in **Figure 2.11**. In this process, strong acid selectively hydrolyzes the amorphous regions which can cause different dimensions between different cellulose sources. Examples of viable cellulose feedstocks where CNCs can be extracted from include: cotton, wood, tunicate, and bacteria.[45] Aspect ratios for CNCs produced from these examples range between one to two orders of magnitude.[46] The type of acid used to generate the CNCs is also important because surface functionalization and dispersion properties will vary from acid to acid. Sulfuric acid hydrolysis places sulfate half esters (strong acid groups) on CNCs whereas hydrochloric acid hydrolysis does not. The strong acid groups present in the sulfuric hydrolysis effectively alters the electric double layer which influences colloidal stability and rheology, both of which are important factors in manufacturing.[47] Once the hydrolysis is complete, the final plank-like, non-toxic, biodegradable CNC that has the ability to form an optically active liquid crystal is ready for thin film and nanocomposite produciton.[45,48-50]

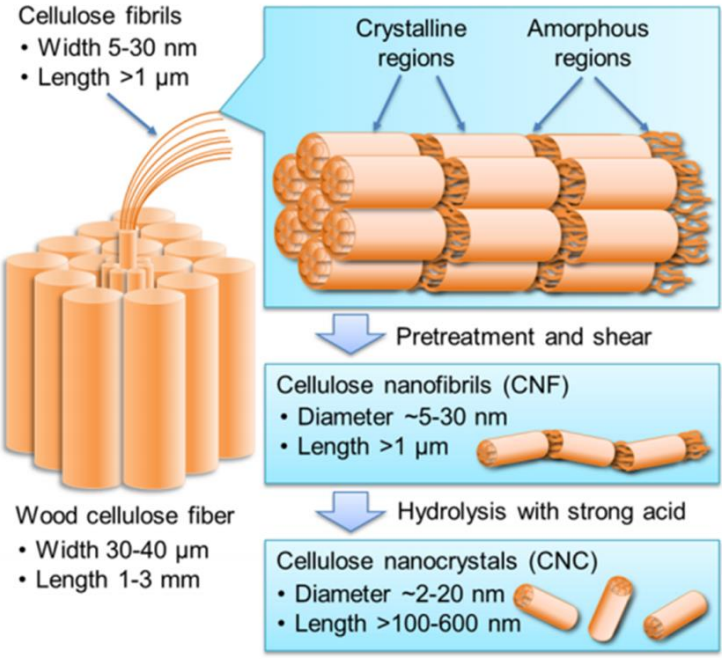

Figure 2.11: Schematic shows the manufacturing of CNCs from a cellulose feedstock. (Reprinted with permissions from American Chemical Society: *Applied Materials and Interfaces* 8, 24, 15607-15614, Cellulose Nanofibril Film as a Piezoelectric Sensor Material, S. Rajala, T. Siponkoski, E. Sarlin, et al. Copyright 2016 American Chemical Society)[51]

CHAPTER III

MODELING OF LIQUID CRYSTALLINE DISPERSIONS

3.1 Oseen-Frank Theory

Since their discovery in 1888 by Friedrich Reinitzer, scientists have tried to accurately predict the anisotropic-isotropic phase transition and capture the effects of molecular interactions in liquid crystalline systems.[9] The earliest continuum models for these systems neglected the contribution of electrostatic forces and utilized curvature-elasticity arguments to generate a structural theory. These models accurately predicted the three classical liquid crystalline types and the first singularities (or defects/disclinations).[52,53] They were first applied to nematic liquid crystals whose orientational order is characterized by uniaxial symmetry. In practice, the entire system was thought of as one large spatial continuum that had a well-defined uniform director which oriented parallel to the long axis of symmetry. The system is then discretized into infinitesimally small regions, each of which, has its own "local" director which designates the orientation of each point in the continuum.[54] From this framework, small perturbations can be approximated at each point by a differential. To account for these perturbations the free energy equation is rewritten to include the free energy of the perturbations (Δf) in addition to the initial free energy at equilibrium ($f_{equilibrium}$).

$$f_{current} = f_{equilibrium} + \Delta f \qquad 0\text{-}1$$

The new equilibrium state is then determined after minimizing equation 0-1. To perform this minimization, a power series expansion of the perturbation free energy (Δf) is applied, and only the even, lowest-order non-vanishing terms are retained (due to the "head" and "tail" of the nematic director representing the same state).[54] The result of this derivation leads to the expression postulated by the Oseen/Frank theory and is as follows:

$$F = \frac{1}{2}K_{11}(\nabla \cdot \boldsymbol{n})^2 + \frac{1}{2}K_{22}(\boldsymbol{n} \cdot \nabla \times \boldsymbol{n})^2 + \frac{1}{2}K_{33}(\boldsymbol{n} \times \nabla \times \boldsymbol{n})^2, \qquad 0\text{-}2$$

where $\boldsymbol{n}(\mathbf{r})$ is the director field that designates the orientation of a rod at position **r** and K_{11}, K_{22}, and K_{33} are the elastic constants that associated with splay, bend, and twist modes of distortion as shown in **Figure 3.1.** These constants are in units of energy. To accurately determine these values, a link between continuum theory and microscopic theory must be established, but this is outside the scope of this chapter.

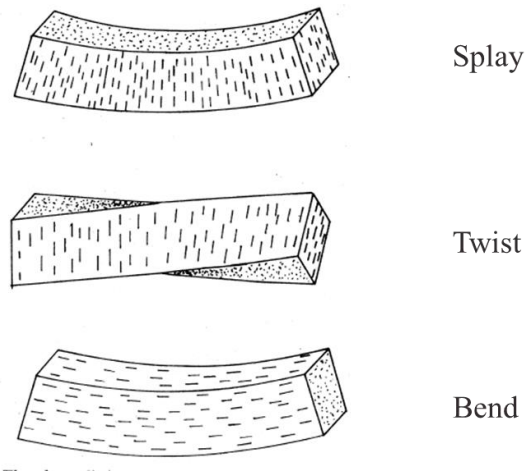

Figure 3.1: Splay, bend, and twist are the three modes of distortion in liquid crystalline systems (Reprinted with permission from American Physical Society: *Review of Modern Physics* 46, 4, 625, Physics of liquid crystals, M.J. Stephen and J.P. Straley. Copyright 1974 American Physical Society)[55]

3.2 Onsager Theory for rigid rods

Onsager's pioneering work on the phase transition of lyotropic liquid crystalline systems serves as the starting point for the development of many mean field phase transition and phenomenological theories. In his work, Onsager established the relationship between the critical aspect ratio of molecules and the onset of the isotropic to nematic phase transition as a result of electrostatic repulsion and excluded volume (**Figure 3.2**).[11]

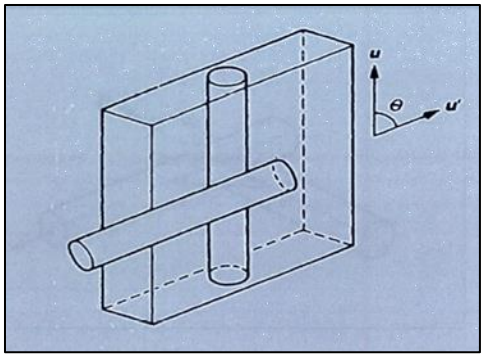

Figure 3.2: Excluded volume between two rods oriented at u and u'. The rod oriented in the direction of u is held constant. The excluded volume is the volume that is inaccessible to the center of mass of rod u' (Reproduced with permission of the Licensor through PLSclear, *The Theory of Polymer Dynamics* Doi and Edwards © 1986)[56]

3.2.1 Probability Distribution Function

In order to quantify for the vast number of molecules and orientations within these systems, it is beneficial to utilize a probability distribution function, *f*. A simple probability distribution function depicting minor fluctuations in orientation is shown in **Figure 3.3.** For perfectly isotropic systems, the orientation of individual molecules of any aspect ratio is completely random. If this molecule, under flow, was studied for an infinite amount of time, it would eventually display all possible entropic orientations. This corresponds to the frequency of rotation of all possible angles from the director, ***n,*** as equal. A graph of this probability would be a uniform flat line. Given the nature of liquid crystalline systems, and the ordering they obtain as a result of temperature and concentration, the frequency of rotation from the director decreases as the system behaves more anisotropically causing the probability peak to sharpen. In the limit of perfect alignment,

the angle of rotation from the director approaches zero and the probability of orientation in the direction of the director approaches unity.

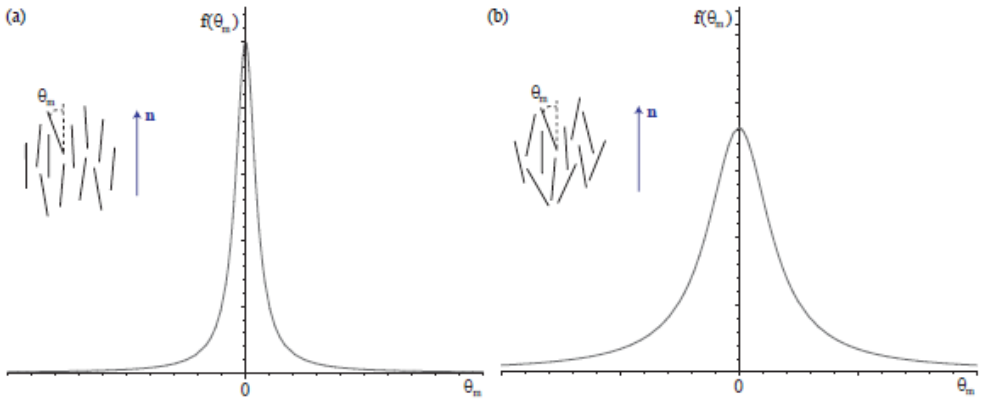

Figure 3.3: For a given position r and director n an angle, θ_m can be established that represents the angle between the director and individual rod. A) At higher order the probability distribution function f contains a sharp maximum with a small standard deviation indicating that large deviations from the director are discouraged by the system. B) In contrast lower ordered systems show a lower peak and a large standard deviation indicating that disorder is more tolerated. A completely isotropic system would show a uniform distribution (Reprinted from open access arXiv operated by Cornell University, Introduction to Q tensor, N.J. Mottram, C.J.P. Newton. Submitted 2014)[57]

This idea of a probable orientation as a function of rotation from the director can be extended into three dimensional space. Rather than define *f* purely as a function of one dimensional rotation, we can extend this using spherical angles such that $f(\boldsymbol{r}, \phi, \theta)$ where $\boldsymbol{r}$ is position and ϕ and θ represent the spherical angles of rotation away from the director $\boldsymbol{n}$. For readability and notational purposes, we elect to define $f(\boldsymbol{r},\boldsymbol{u})$ where $\boldsymbol{r}$ again defines position and $\boldsymbol{u}$ defines the unit vector that is oriented by the spherical angles ϕ and θ. The

integral of the function *f* over all orientations gives the local rod number density $\rho(\boldsymbol{r})$, and similarly, the integral over all orientations and positions gives the total number of rods in the system.

3.2.2 Shape Effects on Colloidal Particles

To develop his theory, Onsager utilized the entropy definition as it applies to possible configurations of particles in an ideal gas system. From that, he argued that liquid crystalline systems could be generalized as non-ideal solutions in which the potentials (repulsive/excluded volume) between particles could be captured in additional entropic terms. These terms when expanded generated cluster integrals which provided the correction terms, the first of which equals the volume denied to another particle due to the condition that two particles cannot intersect and the second which is widely ignored (In the limit of infinite *L/d*, the second virial approximation becomes exact). In their original form, these additional terms included rigorous summations and are replaced by the normalized probability distribution function *f* for convenience and is given by

$$\ln(B_p) = N_p\left\{1 + \ln(\frac{V}{N_p})\right\} - \int f(\boldsymbol{a}) \ln 4\pi f(\boldsymbol{a})\, d\Omega(\boldsymbol{a}) + \frac{N_p}{2V}\int \beta_1\left(cos^{-1}(\boldsymbol{a}\cdot\boldsymbol{a}')\right) f(\boldsymbol{a}) f(\boldsymbol{a}')\; d\Omega d\Omega' \quad \text{0-3}$$

where B_p is the system entropy, V is volume, N_p is the number of particles, $f(\boldsymbol{a})$ is the probability distribution function, and β_1 is the cluster integral. The first term in the

expression is the ideal solution entropy. The second term in the expression is the orientational entropy and the final term in the expression is the excluded volume entropy. Maximizing equation 0-3 and utilizing Lagrange's method, we arrive at the final form of Onsager's equation given by:

$$\ln(4\pi f(\boldsymbol{a})) = \lambda - 1 + \frac{N_p}{V}\int \beta_1(\boldsymbol{a}\cdot\boldsymbol{a}')f(\boldsymbol{a}')\ d\Omega' \qquad 0\text{-}4$$

From this expression, Onsager was able to determine the dimensionless critical concentration for the isotropic and nematic phase transitions.[11] Likewise, Onsager was also able to determine the critical aspect ratio needed for a given concentration to remain within a given phase.

3.3 Leslie-Ericksen

Shortly after Onsager and many years after Oseen, J.L. Ericksen and F.M. Leslie constructed a continuum theory that captured the dynamic viscoelasticity of LC solutions. This theory, known as the Leslie-Ericksen theory, relies on the continuum description first postulated by Oseen and Frank and assumes a perfect unidirectional mesogen orientation (perfectly ordered). Disclinations and inhomogeneities predicted in this theory are solely caused by variations in the director field ***n(r)***.[58-60] The total stress in a liquid crystalline systems is comprised of both elastic and viscous components. The elastic component, derived from the Frank elasticity, is given by:

$$\tau^{Elastic} = -\frac{\partial F_{Frank}}{\partial(\nabla \boldsymbol{n})}\cdot\nabla \boldsymbol{n}, \qquad 0\text{-}5$$

and the viscous component is calculated as:

$$\tau^{viscous} = \propto_1 (\boldsymbol{nn}:\boldsymbol{D})\boldsymbol{nn} + \propto_2 \boldsymbol{nN} + \propto_3 \boldsymbol{Nn} + \propto_4 \boldsymbol{D} + \propto_5 \boldsymbol{nn}\cdot\boldsymbol{D} + \propto_6 \boldsymbol{D}\cdot\boldsymbol{nn}, \quad \text{0-6}$$

where α_i's for i=1, 2, 3…,6 are the Leslie viscosity coefficients, $\boldsymbol{n}$ is the nematic director, $\boldsymbol{D}$ is the deformation tensor $\left(\boldsymbol{D} = \frac{1}{2}(\nabla v + (\nabla v)^T)\right)$ and $\boldsymbol{N}$ is the angular velocity vector of the director relative to the fluid which is defined as:

$$\boldsymbol{N} = \frac{d\boldsymbol{n}}{dt} + (v\cdot\nabla)\boldsymbol{n} + \boldsymbol{W}\boldsymbol{n}, \quad \text{0-7}$$

where $\boldsymbol{W}$ is the vorticity tensor given by $\left(\boldsymbol{W} = \frac{1}{2}(\nabla v - (\nabla v)^T)\right)$. It was found by Parodi *et al.* that only five of the α_i's are independent since $\alpha_2 + \alpha_3 = \alpha_6 - \alpha_5$.[61] Neglecting the external fields, the evolution of the director field can be determined by Oseen's equation[62]:

$$\rho_{Oseen}\frac{D^2\boldsymbol{n}}{Dt^2} = g - \nabla\cdot\pi^{surf}, \quad \text{0-8}$$

where:

$$g = \gamma_{Oseen}\boldsymbol{n} - \beta_{Oseen}\cdot\nabla\boldsymbol{n} - \frac{\partial F_{Frank}}{\partial \boldsymbol{n}} + (\alpha_2 - \alpha_3)\boldsymbol{n} + \frac{(\alpha_5 - \alpha_6)}{2}\boldsymbol{n}\cdot\boldsymbol{W}, \quad \text{0-9}$$

$$\pi^{surf} = \beta_{Oseen}\boldsymbol{n} - \frac{\partial F_{Frank}}{\partial(\nabla\boldsymbol{n})}. \quad \text{0-10}$$

where ρ_{Oseen}, β_{Oseen}, and γ_{Oseen} are constants. In practice ρ_{Oseen} is a known material constant, but the others are unknown and depend upon an arbitrary director. To remove this dependence, a cross product of the director, $\boldsymbol{n}$, and equation 0-8 is taken. The following set of equations encompasses the generalized Leslie-Ericksen theory:

$$v_t + (v \cdot \nabla v) = \nabla \cdot \tau, \qquad 0\text{-}11$$

$$\nabla \cdot v = 0, \qquad 0\text{-}12$$

$$n \times \left(\nabla \cdot \left(\frac{\partial F_{Frank}}{\partial (\nabla n)} \right) - \frac{\partial F_{Frank}}{\partial n} + (\alpha_2 - \alpha_3)\boldsymbol{n} + \frac{(\alpha_5 - \alpha_6)}{2} \boldsymbol{n} \cdot \boldsymbol{W} \right) = 0, \qquad 0\text{-}13$$

$$|n_i n_i| = 1, \qquad 0\text{-}14$$

$$(v, n, @t = 0) \ = (v_0, n_0). \qquad 0\text{-}15$$

Equation 0-11 is the Navier-Stokes equation, where $\boldsymbol{v}$ is the velocity and $\boldsymbol{\tau}$ is the total stress tensor. Equation 0-12 is the assumption of an incompressible fluid and equation 0-13 is the zero torque boundary that encompasses the Frank elasticity of the system.

Shortcomings of this model include the inability to predict the phase transition since the system is assumed to be perfectly ordered and the need to specify many phenomenological parameters that can only be determined empirically by experiments. This theory also lacks the ability to predict nonlinear viscoelastic behavior because of assumptions made on the linear stress dependence of shear rate.[63,64]

3.4 Doi Molecular Diffusive Theory

In contrast to the previous elastic theory, Doi developed the first dynamic micromechanical model that incorporated the excluded volume effect established by Onsager as well as the Brownian force and hydrodynamic force.[13,65,66] The mean field approximation postulated by Doi is as follows:

$$\frac{\partial f}{\partial t} = \nabla_{\boldsymbol{u}} \cdot \bar{D}_r \left(\nabla_{\boldsymbol{u}} f + \frac{f}{k_B T} \nabla_{\boldsymbol{u}} V \right) + \nabla_u \cdot \dot{\boldsymbol{u}} f, \qquad 0\text{-}16$$

where f is the probability distribution function, $\nabla_{\boldsymbol{u}}$ is the gradient operator on a unit sphere, $\dot{\boldsymbol{u}}$ is the velocity gradient, D_r is the rotational diffusivity, and $V(\boldsymbol{r}, \boldsymbol{u}, t)$ is the excluded volume molecular field. The first term in the brackets is the diffusive term of the probability distribution function that induces maximum entropy in the system and the second term is the hard rod excluded volume effects that negates certain entropic configurations. In the dilute limit the excluded volume effects becomes negligible and the diffusive term dominates the system. This removes all gradients in the probability distribution function broadening the peak in **Figure 3.3** as the system approaches maximum entropy which is associated with the isotropic configuration. If we neglect the effects of flow contribution in the equation above, Doi's theory reduces to the popular Cahn-Hilliard formalism that has been used to predict spinodal decomposition in systems with spatial and orientational degrees of freedom. Unlike the LE theory, the Doi model qualitatively captures the rheological behavior seen in regions II and III. Generally, Doi's model is applied to large liquid crystalline polymers whereas LE theory is applied to low molecular weight liquid crystals.

3.5 Combination of Doi and LE Theories

Efforts have been made to write a unifying theory that utilizes the qualities of both the LE and the Doi theories. Of those efforts, the Landau-de Gennes formulation proves to best incorporate these qualities since it reduces to both the LE and Doi theories in the

appropriate limits when hydrodynamic flow is applied. We will now turn our attention to the derivation of the static Landau de Gennes model. The follow up discussion in section 3.7 will highlight the inclusion of ideas in the previous theories present in the Landau de Gennes formulation and conclude with the hydrodynamic Landau de Gennes model.

3.6 Landau-de Gennes (LdG) Theory

The Landau-de Gennes formulation stems from the pioneering work by Landau who first postulated that, near a second order (continuous) phase transition, a relationship between an order parameter and the approximate form of free energy could be established. This relationship, a Taylor series expansion of free energy with respect to order parameter, was constructed in reference to the ferromagnetic-paramagnetic phase transition of a ferromagnetic system.[67] This idea greatly reduced the numerical complexity that was needed to compute the entropic contribution from all possible microstates which was previously determined by solving the Schrödinger equation. In the 1970s, de Gennes applied this idea to the anisotropic-isotropic phase transitions of liquid crystals (nematic-isotropic transition is weakly first order so it was treated as second order).[68] Following de Gennes' derivation, the order parameter for rod-like molecules can be written as:

$$S = < \frac{1}{2}(3\cos^2\theta - 1) >, \qquad \text{0-17}$$

where θ is given as the angle between the mesogens' major axis and the nematic axis (shown as ***n*** in **Figure 3.3**) and <> is the statistical average of the probability distribution function over all possible angles, $f(\theta)$. As it is defined, this microscopic order parameter

is limited to rigid rod-like (uniaxial) molecules and fails to predict mesogen behavior at defect cores. In an effort to predict biaxial systems and behavior at these defect cores, de Gennes defined a new tensor order parameter, $\boldsymbol{Q}$, such that:

$$\boldsymbol{Q} = \int \left(\boldsymbol{uu} - \frac{\boldsymbol{\delta}}{3}\right) f(\boldsymbol{u}) d\boldsymbol{u}^2, \qquad 0\text{-}18$$

which depicts the average orientation of a mesogen at a given position $\boldsymbol{r}$, where f in this equation is the probability distribution function of a mesogen being found in the direction of the unit vector $\boldsymbol{u}$. With this new more general definition, the free energy density expression postulated by de Gennes can be written in Einstein notation as:

$$F_{homogeneous} = \frac{A}{2}\left(1 - \frac{U}{3}\right) Q_{\alpha\beta} Q_{\beta\alpha} - \frac{AU}{3} Q_{\alpha\beta} Q_{\beta\gamma} Q_{\gamma\alpha} + \frac{AU}{4} \left(Q_{\alpha\beta} Q_{\beta\alpha}\right)^2, \qquad 0\text{-}19$$

where A is an energy density scale given by $A=ck_bT$ and U is the dimensionless phenomenological parameter called the nematic potential that controls the anisotropic-isotropic phase transition. According to Doi's theory, $U=3\phi/\phi^*$ where ϕ is the mesogen number density and ϕ^* is the critical mesogen number density in which the phase transition occurs.[13] In short, equation 0-19 represents the entropic free energy and thereby captures the effects of the excluded volume as seen previously in other molecular models, more of this discussion is included in section 3.7. In order to determine the elastic effects in which the order parameter will vary from point to point in the continuum space, an additional free energy density expression is required. This new expression can be given as:

$$F_{gradient} = \frac{1}{2}L_1\partial_\alpha Q_{\alpha\gamma}\partial_\beta Q_{\beta\gamma} + \frac{1}{2}L_2\partial_\alpha Q_{\beta\gamma}\partial_\alpha Q_{\beta\gamma}, \qquad 0\text{-}20$$

where L_1 and L_2 are defined as the Landau elastic coefficients and are described by the Frank elastic constants seen in the Oseen/Frank theory. For our model, we assume a uniaxial nematogen and therefore write the relationship between the Frank elastic constants and the Landau coefficients as:

$$L_1 = \frac{K_{22}}{2S^2}, \quad L_2 = \frac{K - K_{22}}{S^2} \quad \text{where} \quad K = K_{11} = K_{33}. \qquad 0\text{-}21$$

For mesogens that display cholesteric behavior, a final free energy expression must be defined to incorporate long range helical distortion. This final free energy density contribution is as follows:

$$F_{chiral} = q_0 L_q \epsilon_{\alpha\beta\gamma} Q_{\alpha\mu}\partial_\gamma Q_{\beta\mu}, \qquad 0\text{-}22$$

where $\epsilon_{\alpha\beta\gamma}$ is defined as the Levi-Civita; L_q is defined as the chiral Landau elastic constant, and q_o represents an inverse length scale and is qualitatively defined as $2\pi/p$ where p is the helical pitch. To arrive at the final expression for the tensor order parameter $\boldsymbol{Q}$, all free energy density expressions (equations: 0-19, 0-20 and 0-22) are summed and inserted into the Euler Lagrange equation given by:

$$\frac{\delta\mathcal{F}}{\delta Q_{\alpha\beta}} = \frac{\partial F_{total}}{\partial Q_{\alpha\beta}} - \nabla_\gamma \frac{\partial F_{total}}{\partial \nabla_\gamma Q_{\alpha\beta}} = 0 \qquad 0\text{-}23$$

where $\mathcal{F}$is the total free energy given by:

$$\mathcal{F} = \int_V F_{total} dr^3 = \int_V (F_{homogeneous} + F_{gradient} + F_{chiral}) dr^3 \qquad 0\text{-}24$$

Solving the nonlinear equation (equation 0-23) is often difficult and gives many steady state solutions which all depend heavily on the initial condition. In order to make the equation easier to solve, one can recognize that the $\boldsymbol{Q}$ tensor field is non-conservative and follows Langevin-type dynamics. This allows for a time derivative of $\boldsymbol{Q}$ to be written proportional to the functional derivative of the total free energy with respect to all perturbations in $\boldsymbol{Q}$. This analysis provides a pseudo-transient problem given by:

$$\omega \frac{\partial Q_{\alpha\beta}}{\partial t} = -\frac{\partial \mathcal{F}}{\partial Q_{\alpha\beta}}, \tag{0-25}$$

where ω is a time constant associated with the phenomenological system. In order to simplify the number of unknowns in the $\boldsymbol{Q}$ tensor, equation (0-25) can be transformed to ensure that the $\boldsymbol{Q}$ tensor remains symmetric and traceless via:

$$\omega \frac{\partial Q_{\alpha\beta}}{\partial t} = \left[-\frac{\partial \mathcal{F}}{\partial Q_{\alpha\beta}}\right]^{s}, \tag{0-26}$$

where

$$\left[\frac{\partial \mathcal{F}}{\partial \boldsymbol{Q}}\right]^{s} = \frac{1}{2}\left(\frac{\partial \mathcal{F}}{\partial \boldsymbol{Q}} + \frac{\partial \mathcal{F}}{\partial \boldsymbol{Q}}^{T} - \frac{2}{3} tr\left(\frac{\partial \mathcal{F}}{\partial \boldsymbol{Q}}\right)\right). \tag{0-27}$$

3.7 Combination of Theory exhibited in the Landau de Gennes equation

Further analysis of the Landau de Gennes equation shows a systematic inclusion of previous ideas presented in the micromechanical theory presented by Onsager, later redefined by Doi, and the continuum elastic theory presented by Oseen/Frank. As shown

in section 3.2 equation 0-2, Oseen/Frank derived a free energy contribution related to the elastic modes of deformation. The synonymous inclusion of this idea in the Landau de Gennes formulation is equation 0-20 and equation 0-22, if chiral deformation is included, and are defined by the same Frank elastic constants in the coefficients L_1 and L_2. Similarly, Onsager's work is synonymous with equation 0-19. This becomes readily apparent in the derivation by Doi in which he generalized the mean field potential using Onsager's solution to the free energy and converted the probability distribution function into a dynamic $\boldsymbol{Q}$ tensor using equation 0-18.[13]

In order to describe a flowing system in the Landau de Gennes framework, an additional term must be included in the dynamic equation which contributes to the alignment of the $\boldsymbol{Q}$ tensor based on an external flow. This provides a one way coupling to the fluid as the velocity term is allowed to influence the dynamic of the $\boldsymbol{Q}$ tensor. This addition allows the Landau de Gennes equation to reduce to the LE theory and Doi theory within the respective limits of (De $\rightarrow$ 0 or elastic effects become negligible respectively). The general form of the new dynamic $\boldsymbol{Q}$ tensor equation is:[69]

$$\frac{\partial \boldsymbol{Q}}{\partial t} + \boldsymbol{v} \cdot \nabla \boldsymbol{Q} + \boldsymbol{Q} \cdot \boldsymbol{\Omega} - \boldsymbol{\Omega} \cdot \boldsymbol{Q} = -\alpha \frac{\delta \mathcal{F}}{\delta \boldsymbol{Q}} + V_{\boldsymbol{Q}}(\boldsymbol{D}) \qquad 0\text{-}28$$

Where v is the velocity, α is the collective rotational diffusion constant and $V_{\boldsymbol{Q}}$ is given by:

$$\begin{aligned} V_{\boldsymbol{Q}}(\boldsymbol{D}) = (\beta \boldsymbol{D} + \boldsymbol{\Omega})\left(\boldsymbol{Q} + {}^{\boldsymbol{I}}/_{3}\right) + \left(\boldsymbol{Q} + {}^{\boldsymbol{I}}/_{3}\right)(\beta \boldsymbol{D} - \boldsymbol{\Omega}) \\ - 2\beta\left(\boldsymbol{Q} + {}^{\boldsymbol{I}}/_{3}\right) Tr(\boldsymbol{Q}\boldsymbol{W}), \end{aligned} \qquad 0\text{-}29$$

Where $\boldsymbol{W}$ is the velocity gradient tensor and $\boldsymbol{D} = (\boldsymbol{W}+\boldsymbol{W}^T)/2$ is the symmetric contribution and $\boldsymbol{\Omega} = (\boldsymbol{W}-\boldsymbol{W}^T)/2$ is the antisymmetric contribution.[70]

In order to completely describe the liquid crystalline system a two way coupling must be established in which the $\boldsymbol{Q}$ tensor influences the velocity of the fluid similar to the Leslie-Ericksen theory. This is accomplished by solving a system of equations that includes the dynamic $\boldsymbol{Q}$ tensor equation, the continuity equation, and the Navier-Stokes equation in which the stress tensor of the Navier Stokes equation is correlated to the $\boldsymbol{Q}$ tensor. Currently, there is no first principle derivation that relates the two together. In practice, constitutive equations are used to determine the $\boldsymbol{Q}$ tensor contribution to the symmetric and antisymmetric viscous stress tensors as well as the distortion stress tensor which is then utilized to solve the system of equations.[71,72] For the Landau de Gennes formulation, this constitutive equation takes the form of[71]

$$\tau^{viscous} = \nu_1 \boldsymbol{D} + \nu_2 \left[\boldsymbol{Q}\cdot\boldsymbol{D} + \boldsymbol{D}\cdot\boldsymbol{Q} - \frac{2}{3}(\boldsymbol{Q}:\boldsymbol{D})\boldsymbol{I}\right] + \nu_4[(\boldsymbol{Q}:\boldsymbol{D})\boldsymbol{Q} + \boldsymbol{D}\cdot\boldsymbol{Q}\cdot\boldsymbol{Q} + \boldsymbol{Q}\cdot\boldsymbol{D}\cdot\boldsymbol{Q} + \boldsymbol{Q}\cdot\boldsymbol{Q}\cdot\boldsymbol{D} + [(\boldsymbol{Q}:\boldsymbol{Q})\boldsymbol{D}]I], \quad \text{0-30}$$

where ν_i*'s* are the Landau viscosity coefficients which must be fitted to the specific liquid crystalline material. Regardless of the constitutive equation, many fitting parameters remain. Previous work has shown a connection between the Landau viscosity coefficients and the Leslie viscosity coefficients seen in equation 0-6. These correlations incorporate the second and fourth order Legendre polynomials, Mesowicz viscosities, dimensionless concentration, and numerical corrections factors.[25,71-74]

In the scope of the experiments with which the models presented in this thesis are validated, flow is assumed to be negligible. This allows for the dynamics presented to be completely described by equation (3-12).

CHAPTER IV

SIMULATION METHODOLOGY AND VISUALIZATION TECHNIQUES

4.1 Finite Element Analysis

COMSOL Multiphysics 5.2 (Los Angeles, CA) finite element software provided the numerical infrastructure used to solve the finite element formulation of the Landau-de Gennes equation. In these simulations, the General Form PDE underneath the Mathematics module is selected and the equations are programmed into it accordingly. The simulations are solved on a variety of square and tetrahedral meshes to ensure accuracy and obtain good results.

4.2 Visualization methods

Our finite element analysis of the Landau-de Gennes model derived in Chapter 3 section 2 computes the continuous $\boldsymbol{Q}$ tensor field that describes local average orientation of the mesogens at given times and locations in space. In order to get meaningful data from the orientation tensor, we have devised a series of numerical codes to generate ellipsoidal maps and simulated micrographs to visualize the textures and defects commonly seen in cholesteric nematics. The rest of this chapter will be devoted to explaining and deriving the equations needed to generate such figures.

4.2.1 Ellipsoidal Maps

To create each ellipsoid map, as shown in **Figure 4.1**, eigenvalue and eigenvector analysis of the $\boldsymbol{Q}$ tensor is performed at uniformly spaced locations within the simulation domain. To ensure the eigenvalues for the $\boldsymbol{Q}$ tensor remain positive for visualization we redefine the $\boldsymbol{Q}$ tensor as:

$$\boldsymbol{Q}(\boldsymbol{r},t) = \boldsymbol{Q}(\boldsymbol{r},t) + \boldsymbol{I}/_3, \qquad 0\text{-}1$$

where $\boldsymbol{I}$ is the identity matrix. The major axis of each ellipsoid represents the uniaxial director of the mesogen and is denoted by vector $\boldsymbol{n}$ which corresponds to the eigenvector whose eigenvalue is of the greatest magnitude.

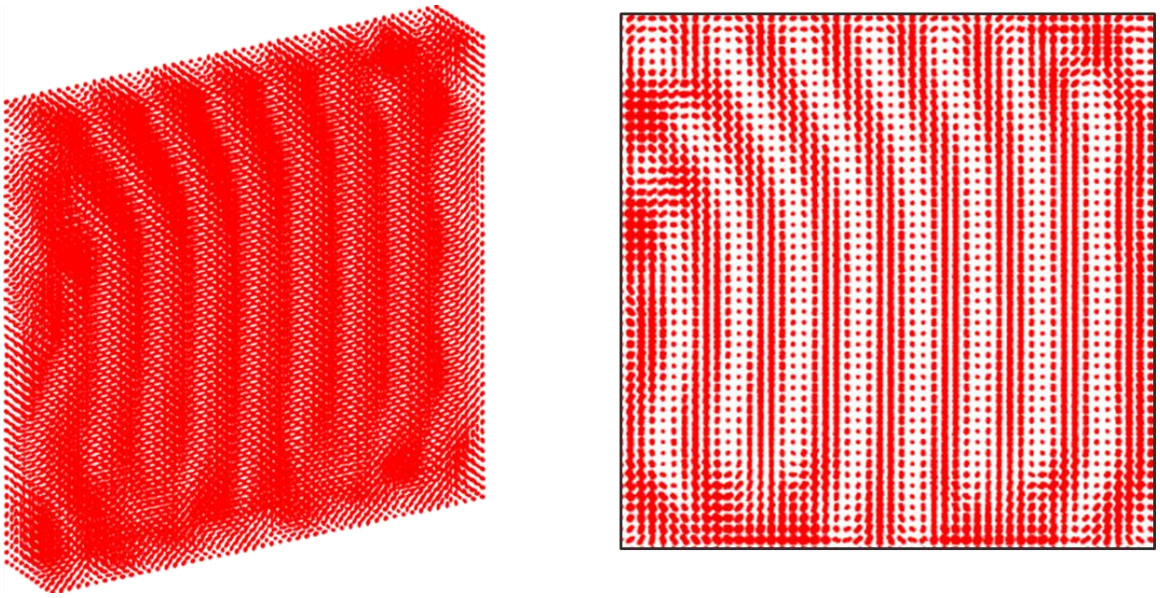

Figure 4.1: Example of a 3D ellipsoidal map showing local rod orientation. Note the fingerprint texture that is commonly seen in cholesteric liquid crystals. (Reprinted with permissions from American Chemical Society: *Langmuir* 34, 44, 13274-13282, Orientation Relaxation Dynamics in Cellulose Nanocrystal Dispersions in the Chiral Liquid Crystalline Phase, M. J. Pospisil, P. Saha, S. Abdulquddos, et al. Copyright 2018 American Chemical Society). [43]

The other two minor axes correspond to the remaining eigenvectors that correspond to the second largest and smallest eigenvalues and are denoted by vector ***m*** and ***l*** respectively. (See **Figure 4.2**) Each axis within the ellipsoid is scaled by its corresponding eigenvalue. Highly aligned mesogen regions will be represented by an elongated ellipsoid with directional alignment whereas isotropic regions will be characterized by spheroids with no alignment.

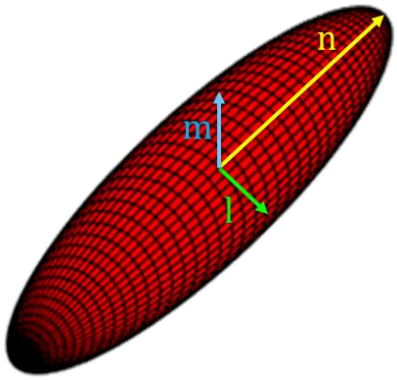

Figure 4.2: Representation of the Q tensor as an ellipsoid that is determined by the eigenvector-eigenvalue analysis. The vector n is the molecular director corresponding to the eigenvector corresponding to the largest eigenvalue.

In general there are three classifications of ellipsoids: isotropic, where there is no preferred alignment, prolate, where a preferred alignment exists, and oblate, where preferential alignment is equal in two directions but not in the third (**Figure 4.3**). It is worth noting that in the prolate and oblate cases, the degree of alignment is strongly correlated to the length of the minor axis of the ellipsoid. In the limit of perfect alignment, the ellipsoid is represented by a line as the eigenvalues that scale the minor axes are zero. In the limit of perfectly oblate, the probability of pointing in a given direction is zero and thus the eigenvalue corresponding to the minor axis oriented in that direction is also zero. The ellipsoid in the perfectly oblate case is therefore represented by a circle whose face is normal to the direction of zero probability.

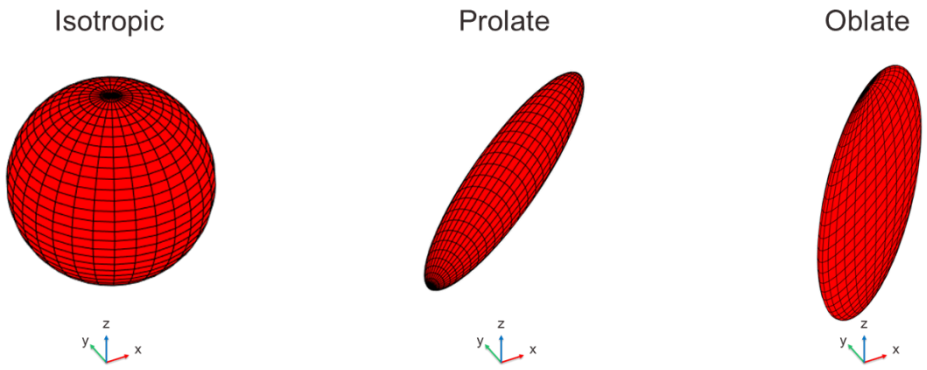

Figure 4.3: Extreme examples of the ellipsoids are shown. Note the oblate case has limited probability in the y direction**.**

4.2.2 Simulated Micrographs

The simulated micrographs were generated using a formalism developed by Ondris-Crawford *et al* which mimics the rotation and phase shift of polarized light as it passes through optically active liquid crystalline systems.[75] The formal definition for the intensity map is as follows:

$$I(x,y) = \left\| e_A \hat{P} e_P \right\|^2 \qquad 0\text{-}2$$

where e_A and e_p represent the analyzer orientation and the incident polarization. $\boldsymbol{P}$ represents the transformation matrix which is given formally as:

$$\hat{\boldsymbol{P}} = \hat{\boldsymbol{R}}_{\boldsymbol{N+1}} \boldsymbol{S}_{\boldsymbol{N}} \ldots \hat{\boldsymbol{R}}_{\boldsymbol{2}} \hat{\boldsymbol{S}}_{\boldsymbol{2}} \hat{\boldsymbol{R}}_{\boldsymbol{1}} \hat{\boldsymbol{S}}_{\boldsymbol{1}} \qquad 0\text{-}3$$

where $\boldsymbol{S}$ represents the phase shift of light as it moves through each subsequent nematic layer within the sample and $\boldsymbol{R}$ represents the rotation matrix for the polarization vector for each subsequent layer. To compute these matrices, first eigenvalue-eigenvector

analysis is performed on each ***Q*** tensor to determine the molecular nematic director for at each grid point, equivalent to the ellipsoidal mapping method. After the determination of the molecular directors, the plane of incidence is determined. This plane is determined by a reference vector $\boldsymbol{n}_D$ and the wave vector $\boldsymbol{k}_0$. The reference vector $\boldsymbol{n}_D$ should be carefully chosen to ensure that the nematic directors are cylindrically symmetrical about it. Since our adaptation is applied to a laboratory setup, we invoke the use of Cartesian coordinates, and set up the incident plane that corresponds to the plane normal to the viewing angle.

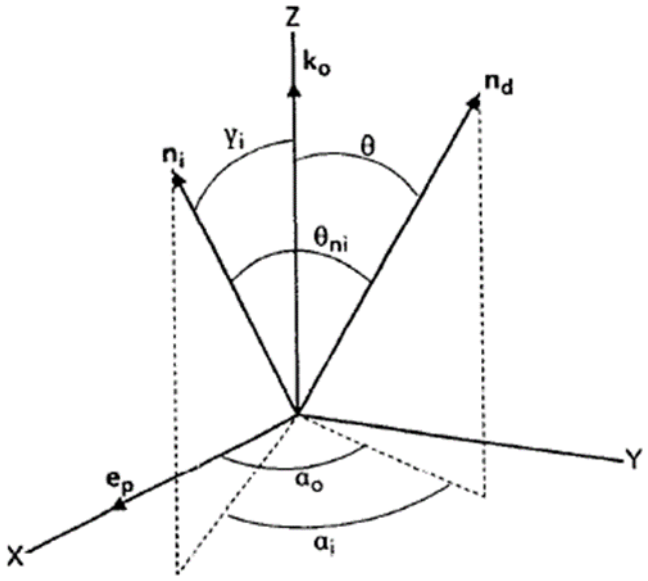

Figure 4.4: Illustration of the symbols and coordinates used in calculating the texture in a chiral nematic. This image indicates the n_D the reference vector, k_0 direction of incident light, n_i local nematic director, and ep the polarization vector (Reprinted with permission from AIP Publishing: *Journal of Applied Physics* 69, 9, 6381, Microscope textures of nematic droplets in polymer dispersed liquid crystals, R. Ondris-Crawford, E. P. Boyko, B. G. Wagner, et al. Copyright 1991 AIP Publishing).[75]

From our established incident plane and incident of polarization, we are able to determine the first angle, α_0. From these values every sequential term can be determined for both the ***R*** and ***S*** matrices which are as follows:

$$R_i = \begin{bmatrix} \cos(\alpha_i - \alpha_{i-1}) & -\sin(\alpha_i - \alpha_{i-1}) \\ \sin(\alpha_i - \alpha_{i-1}) & -\cos(\alpha_i - \alpha_{i-1}) \end{bmatrix} \quad \text{0-4}$$

$$S_i = \begin{bmatrix} e^{2\pi\delta n_o\sqrt{-1}/\lambda_0} & 0 \\ 0 & e^{2\pi\delta n_e(\gamma_i)\sqrt{-1}/\lambda_0} \end{bmatrix} \quad \text{0-5}$$

where n_o and $n_e(\gamma_i)$ are the ordinary and extraordinary indices of refraction respectively. In the above expression, the extraordinary index of refraction, $n_e(\gamma_i)$, depends on the angle between the optical axis (nematic director) and the wave vector k_0 and is formally defined as:

$$n_e(\gamma_i) = \frac{n_o n_e{}'}{(n_o \sin(\gamma_i))^2 + (n_e{}' \cos(\gamma_i))^2} \quad \text{0-6}$$

The other constants seen in equations 0-5 and 0-6 include the wavelength of incoming light, λ_0, the spacing between nematic layers δ, and the constant n_e' which represents the pure index of refraction (typical ranges for the ordinary and extraordinary indices of refractions for CNC systems are between 1.576 and 1.595 and 1.527 and 1.534 respectively).

By setting the angle α_0 to $\pi/2$, we ensure that the vector n_D lies in the correct plane and is angles counterclockwise to the x-axis. From this reference point and the initial wave vector k_0, the angles α_i and γ_i can be computed for every node in dataset. α_i is defined as the angle between the local nematic director given by the eigenvector-eigenvalue

analysis and the vector n_D. γ_i represents the angle between the local nematic director and the wave vector of incident light, k_0. For our simulated micrographs three different wavelengths of incoming light were chosen, 685 nm corresponding to red, 532.5 nm corresponding to green, and 445 nm corresponding to blue, and were converted into a final greyscale image.

CHAPTER V

ORIENTATION RELAXATION DYNAMICS IN CELLULOSE NANOCRYSTAL DISPERSIONS IN THE CHIRAL LIQUID CRYSTALLINE PHASE[*]

5.1 Introduction

Fluid phase ordering of lyotropic liquid crystals has proven to be one of the most scalable and cost-efficient strategies to produce aligned nanostructured materials for tailored macroscopic applications.[76,77] Lyotropic dispersions typically consist of a rigid anisotropic mesogen dispersed in a solvent and possess both fluidity and crystal-like ordering. At low concentrations, lyotropic systems exhibit isotropic ordering where material properties are uniform in all directions. As concentration is increased, these dispersions become biphasic; both isotropic and anisotropic phases coexist. These newly formed anisotropic phases are the result of the alignment-induced gains in translational entropy and the simultaneous losses in rotational entropy. This entropic phenomenon causes the new phase to exhibit orientational order and alignment dependent material properties. Additionally, these newly formed anisotropic domains continually grow and fuse throughout the biphasic region as concentration is continually increased. At sufficiently high

[*] Reprinted with permissions from American Chemical Society: *Langmuir* 34, 44, 13274-13282, Orientation Relaxation Dynamics in Cellulose Nanocrystal Dispersions in the Chiral Liquid Crystalline Phase, M. J. Pospisil, P. Saha, S. Abdulquddos, et al. Copyright 2018 American Chemical Society

concentrations, the volume fraction of the isotropic regions becomes infinitesimally small and the biphasic dispersions completely develop into a fully liquid-crystalline phase.

Chiral nematic liquid crystals, also known as cholesteric liquid crystals, represent a special subclass of the liquid crystalline phase in which mesogens self-assemble into helical microstructures due to their interactions. The presence of this hierarchical structure is what gives chiral nematic systems their interesting optical properties.

Cellulose nanocrystals (CNCs) extracted from woody biomass using sulfuric acid hydrolysis represent a model charged chiral nematic system. CNCs, extracted in this manner, have a combination of sulfate half esters and hydroxyl surface groups that allow them to readily disperse in water and exhibit lyotropic cholesteric phase behavior. Furthermore, the phase transitions that occur due to the changes in the volume fraction of the CNCs are easily identified using polarized optical microscopy.[78] **Figure 5.1** displays left-handed helical microstructures and characteristic fingerprint textures that form as a result of mesogen ordering in the biphasic CNC dispersion.

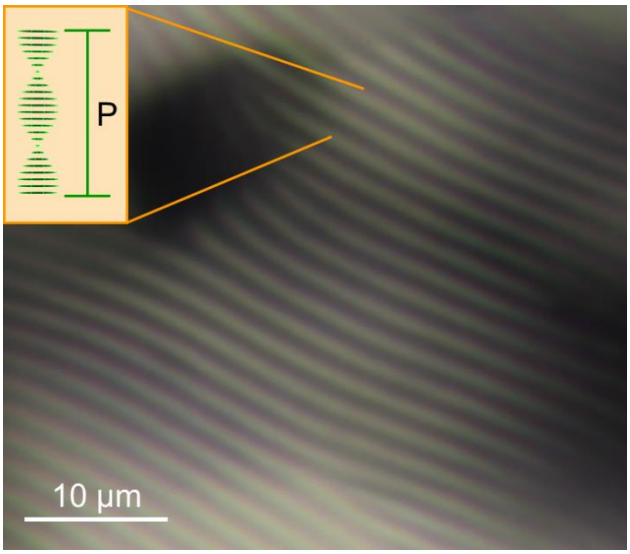

Figure 5.1: Cross-polarized transmitted light microscopic image of 5.14 vol% dispersion of CNCs in water. (Reprinted with permissions from American Chemical Society: *Langmuir* 34, 44, 13274-13282, Orientation Relaxation Dynamics in Cellulose Nanocrystal Dispersions in the Chiral Liquid Crystalline Phase, M. J. Pospisil, P. Saha, S. Abdulquddos, et al. Copyright 2018 American Chemical Society) [43]

This non-toxic, biodegradable mesogen also has a high Young's modulus and is easily extracted from a variety of abundant cellulose sources via acid hydrolysis.[45,48-50] Because of these characterisitcs, CNCs possess a broad range of desirable properties that can be incorporated into many thin film applications, but only if structure-property relationships are understood in both lab-scale experimental design and industrial scale-up.

Prior studies have shown that both the macroscopically chiral and achiral mesogen orientations in CNC thin films have useful properties. Recent results have indicated that aligned CNC films exhibit reduced stress concentrations, resulting in mechanically robust structures and unique thermal properties.[45,79-82] Meanwhile, chirally oriented mesogens produce films that exhibit photonic properties by shifting the Bragg reflections into the

visible spectra which can be used in optical sensing applications such as selective reflection, mirrorless lasing, bioimaging, and security encryption. [1-5]

However, manufacturing hurdles such as the introduction of defects and other non-uniformities during film drying can make it difficult to obtain the desired mechanical or optical properties.[83] To meet these challenges in processing, the scientific community has developed methods to control mesogen orientation dynamics. Recent work by Park *et at.* and Ličen *et al.* have shown that orbital shear creates a more uniform planar alignment in dried films. This uniform configuration is a result of shear-induced elongated regions fusing as a consequence of changes in interfacial energy during drying.[84,85] Similarly, homogenous planar configurations have also been shown to appear in samples that were subjected to a strong magnetic field.[86,87] In this case, the negative diamagnetic anisotropy of the CNCs cause the chiral nematic axis to preferentially align perpendicular to the field. However, there has been relatively little work to show how theory and modeling can capture these effects.

Models for hard-rod dispersions are typically described by nematogen theories that incorporate short range potentials and long range elasticity. One such formalism based on the Landau-de Gennes (LdG) theory has successfully predicted defect formation and portrayed tumbling of achiral discotic mesogens in two dimensional systems.[88-91] In order to describe chiral nematic systems, a chiral force term was later added to this formulation to induce helical distortion.[92] This distortion is a result of the competition between spatial

gradients caused by chiral forces and the elastic terms that penalize those gradients. In our prior study, we utilized this chiral formulation to conduct dynamic simulations on rod-like mesogens with the aim of tuning experimental flows to generate desired conformations.[93] These simulations allowed helical microstructures to form in two dimensions and focused on the effects of boundary anchoring and initial mesogen orientation under flow.[93] At low shear rates, the chiral force term and elastic terms prevented the rods from responding to flow. However, at high shear rates, the rods tumbled and formed unique chiral structures as the flow and chiral forces competed. Phase diagrams were generated from these results to give an overview of the dynamic behavior exhibited by these rod-like mesogens under applied shear. Later work by Noroozi *et al.* used the same formulation in conjunction with a constitutive equation to show the dependence of steady shear viscosity on shear rate in concentrated CNC dispersions.[71] Their results accurately mapped the same shear regions that have been observed in previous experimental results.[71] A recent study by Rey *et al.* used a slightly different LdG formulation to model CNC thin film formation.[94] Their model coupled the local rod orientation to a time-dependent spatially varying concentration function to simulate drying effects. They predicted three different microstructural textures due to diffusion rates of the mesogen and the solvent. Their results showed that below a critical drying rate (where helical microstructure development is much faster than solvent loss), dispersions developed a domain characterized by non-uniform helical orientation. On the other hand, above the critical drying rate, (where helical microstructure development is much slower than solvent loss) the system generated defect-laden films due to destabilized helical formation.

In an effort to further understand the microstructural response of cholesteric dispersions, we report a combination of experiments and modeling to study the relaxation dynamics of CNCs after shear cessation. Since CNC systems spontaneously develop into helical microstructures, the CNC dispersions were shear aligned on a parallel plate geometry to mimic the preferential alignment induced by thin film processing and remove pre-existing microstructure. Our samples were imaged during their relaxation using rheo-optics. To compare with experiments, a finite element analysis was conducted using COMSOL Multiphysics that captured the relaxation of mesogens from a shear aligned initial state. Our 3D model avoids the assumption of uniformity in the vorticity (normal to flow and shear) direction and allows chiral microstructures to develop uninhibited throughout the entire system, in contrast to previous models that were simplified to two dimensions and restricted complex helical formations.

5.2 Experimental Setup

5.2.1 Dispersion preparation

Aqueous cellulose nanocrystal dispersions were obtained from the U.S. Department of Agriculture Forest Product Lab (batch 2016-FPL-CNC-098) with a specified sulfur content of 0.95 wt% and supplied by the University of Maine (Orono, ME). Characterization of electrolytic properties of the dispersions were obtained on the stock gel dispersion using a VWR International (Radnor, Pennsylvania) Traceable Expanded

Range Conductivity Meter, yielding conductivity of 1348 μS/cm, Ionic Strength: 6.87 x 10^{-3} M, pH: 5.86 and Charge density: 234 C/g_{CNC} or 375 C/mL_{CNC}. The average aspect ratio (L/D) measured by AFM was 30.7 (σ = 9.8). As received, the dispersions were 7.97 vol. % but were diluted to 4.48 vol. %, 5.14 vol. %, and 5.81 vol. % CNC for the purposes of this research (reference density for the vol. % is 1.6 g/cm^3 for the CNC mesogens and 0.992 g/cm^3 for water). Anisotropic volume fractions for the 4.48 vol. %, 5.14 vol. %, and 5.81 vol. % CNC dispersions were approximately 60 vol. %, 90 vol. %, and 100 vol. % respectively. Samples were diluted with ultrapure water (purified using Thermo Scientific Auto Dispenser, Millipore water, pH 6.5, and conductivity 0.95 μS/cm at 23.3 ^oC), vortex mixed, and allowed to mix overnight on a bottle roller to ensure uniform mixing. Before shearing, the dispersions were allowed to rest for 1 hour to make sure no air bubbles were present. These concentrations corresponded to a biphasic, highly concentrated biphasic that lies just below the biphasic-liquid crystalline phase transition, and liquid crystalline dispersion, respectively.

5.2.2 Optical microscopy

Cross-polarized optical microscopy was performed with a Nikon Eclipse 80i microscope with an LU Plan Fluor 20x/0.45NA Nikon objective. For static samples, sample preparation was as follows: approximately 100 μL were placed between a 120 μm adhesive spacer on a pre-cleaned glass slide and a coverslip placed on top for optical imaging. For microscopy post-shear relaxation studies, the microscope was equipped with

a Linkam CSS450 Optical Rheology System and a L Plan SLWD 20x/0.35NA Nikon objective were used, the setup is shown in **Figure 5.2.** Polarizers were oriented at 0° or 45° with respect to the flow direction. The quartz windows of the shear cell were cleaned with water, isopropanol and lint-free tissues prior to each experiment. All dispersions were sheared on a parallel plate geometry using the Linkam Optical Rheology System at room temperature with a shear rate of 100 s^{-1} for 5 minutes to ensure complete rod alignment in the flow direction. The shear was then stopped, and the dispersion was allowed to relax. During shear relaxation, a time lapse was captured. The automated time lapse consisted of taking images every 10 s for 15 min, then every 30 s for 45 minutes to 1.5 hours. To avoid the effects of evaporation that occur at the edges of the sample, all results were taken from the center of the sample where such effects were negligible throughout the duration of the experiments. All the images were captured and adjusted (exposure and gain) using Nikon Elements software. Images were not taken after 90 min due to concerns about sample drying.

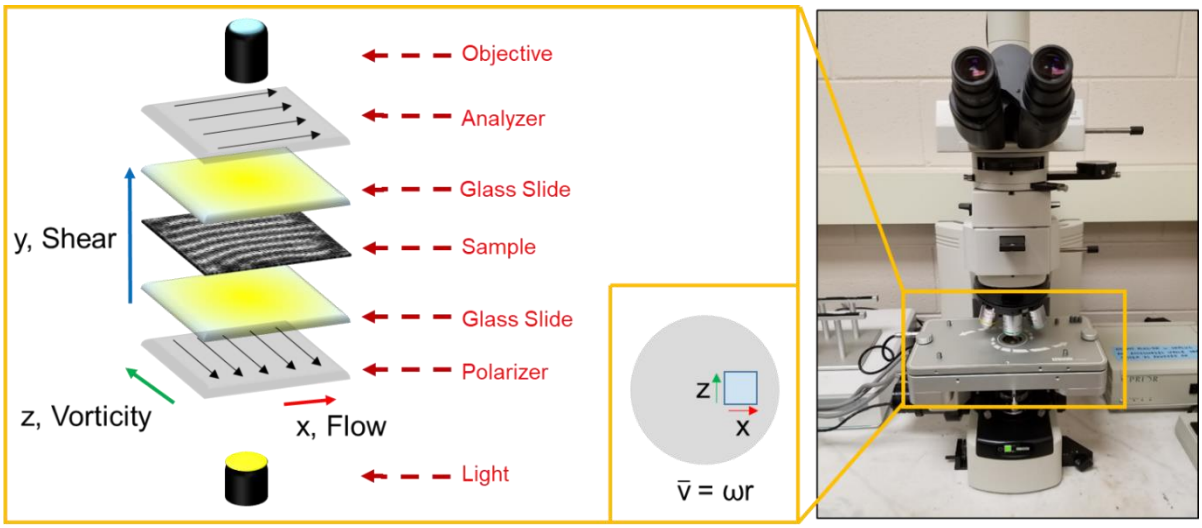

Figure 5.2: The Nikon Eclipse 80i and the Linkam shear cell that were used in the experiments are shown on the right. An illustration of the shear cell apparatus is shown on the left. The inset shows the viewing window at a radial distance r to capture the image. (Reprinted with permissions from American Chemical Society: *Langmuir* 34, 44, 13274-13282, Orientation Relaxation Dynamics in Cellulose Nanocrystal Dispersions in the Chiral Liquid Crystalline Phase, M. J. Pospisil, P. Saha, S. Abdulquddos, et al. Copyright 2018 American Chemical Society).[43]

5.3 Model Formulation

Our purpose is to investigate the effects of experimental parameters on helical microstructure formation in all three spatial dimensions during the relaxation of CNC liquid crystalline dispersions. Local representation of the microstructure is captured in the second moment of the orientation distribution function, ***f(u)***, written as the second order traceless tensor ***Q***,

$$\boldsymbol{Q} = \int \left(\boldsymbol{uu} - \frac{\delta}{3}\right) f(\boldsymbol{u}) d\boldsymbol{u}, \qquad 0\text{-}1$$

where $\boldsymbol{u}$ is a unit vector describing the rod orientation. We utilize the same dimensionless LdG formalism as Venhaus *et al.*[93]

$$\begin{aligned}\frac{d\boldsymbol{Q}}{dt} &= \boldsymbol{W}\cdot\boldsymbol{Q}-\boldsymbol{Q}\cdot\boldsymbol{W}+\frac{2}{3}\beta\boldsymbol{A}+\beta\left[\boldsymbol{A}\cdot\boldsymbol{Q}+\boldsymbol{Q}\cdot\boldsymbol{A}-\frac{2}{3}(\boldsymbol{A}\colon\boldsymbol{Q})\boldsymbol{I}\right]\\ &-\frac{1}{2}\beta\left[(\boldsymbol{A}\colon\boldsymbol{Q})\boldsymbol{Q}+\boldsymbol{A}\cdot\boldsymbol{Q}\cdot\boldsymbol{Q}+\boldsymbol{Q}\cdot\boldsymbol{A}\cdot\boldsymbol{Q}+\boldsymbol{Q}\cdot\boldsymbol{Q}\cdot\boldsymbol{A}-\left((\boldsymbol{Q}\cdot\boldsymbol{Q})\colon\boldsymbol{A}\right)\boldsymbol{I}\right]\\ &-\frac{6R}{Er}\left[(1-\mathrm{U}/3)\boldsymbol{Q}-U\boldsymbol{Q}\cdot\boldsymbol{Q}+U(\boldsymbol{Q}\colon\boldsymbol{Q})\left(\boldsymbol{Q}+\frac{\boldsymbol{I}}{3}\right)\right]\\ &+\frac{1}{Er}\left[\nabla^2\boldsymbol{Q}+\frac{1}{2}\frac{L_2}{L_1}\left(\left(\left(\nabla(\nabla\cdot\boldsymbol{Q})\right)+\left(\nabla(\nabla\cdot\boldsymbol{Q})^T\right)\right)\right.\right.\\ &\left.\left.-\frac{2}{3}tr(\nabla(\nabla\cdot\boldsymbol{Q})\boldsymbol{I})\right)\right]-\boldsymbol{P}\end{aligned} \qquad 0\text{-}2$$

where $\boldsymbol{W}$ and $\boldsymbol{A}$ are the vorticity and strain tensors, respectively. U is the dimensionless nematic potential which controls the phase transition between an isotropic or nematic system ($U_{critical}$ = 3). L_1 and L_2 represent the first and second Landau elastic moduli respectively. $\beta = (p^2\text{-}1)/(p^2+1)$ is a shape factor that approaches unity for rods of infinite aspect ratio, and $\boldsymbol{P}$ is the chiral force contribution to the system.

Important dimensionless numbers include the Ericksen number, *Er*, which represents the ratio of inertial to elastic forces, and the dimensionless quantity *R*, which represents the ratio of short-range interactions to long-range elasticity.

$$Er = \frac{\tau H^2 ckT}{6L_1 D_r}. \qquad 0\text{-}3$$

$$R = \frac{H^2 ckT}{6L_1}. \qquad 0\text{-}4$$

The quantity c is the rod number density; H is the gap height of the shear cell; D_r is the rotational diffusivity of the rods, and τ is the timescale of the experiment given as

$$\tau = \frac{6L_1 D_r}{H^2 c k_B T}. \quad \text{0-5}$$

The chiral interaction term posited by Cui and Calderer is written in Einstein notation as

$$P_{ij} = \frac{\theta}{Er}\left(\epsilon_{mik} Q_{mj,k} + \epsilon_{mjk} Q_{mi,k}\right), \quad \text{0-6}$$

where ϵ is the Levi-Civita symbol. The dimensionless chiral strength, θ, is defined as the ratio of chiral strength (the elastic strength of helical distortions) to Frank elasticity and is given by equation 0-7.[92]

$$\theta = \frac{H\hat{L}_q}{6L_1}, \quad \text{0-7}$$

where $\hat{L}_q$ represents a combined physical constant that is the product of the chiral elastic moduli, L_q, and an inverse length q_0. Qualitatively, q_0 is defined as $2\pi/p$ where p is the helical pitch.[68] Experimentally, many factors have been shown to influence chiral strength including concentration of rods, ionic strength, aspect ratio, and charge distribution along the rod. [95,96] All of these factors are collectively captured in θ. Theoretical studies have been done to decouple the factors that influence θ, but their results are derived from infinitely thin helical particles and have not been confirmed experimentally for CNC systems. [32] For the purpose of this study, we will continue to encompass all effects in the dimensionless chiral strength parameter, θ.

Visualization of results: From our COMSOL solutions, textures and defects similar to those seen in experiments can be identified using ellipsoid maps and/or simulated micrographs. These ellipsoid maps, that represent local orientation of the mesogen, are generated from eigenvalue-eigenvector calculations that are performed on ***Q*** tensors which are uniformly spaced in the simulation domain. For each ellipsoid, the major axis is scaled by the largest eigenvalue and lies in the direction of the corresponding eigenvector which represents the molecular director. The other minor axes of the ellipsoid are drawn from the remaining two eigenvalues and eigenvectors. The simulated micrographs of the solution are also generated by ***Q*** tensors that are uniformly spaced in the solution space. Similar to the ellipsoid maps, an eigenvalue-eigenvector analysis is performed on each ***Q*** tensor to obtain the molecular directors. These directors are then used in a Jones Matrix formalism proposed by Ondris-Crawford *et al.*[75] to create the final images. These visualization methods readily display desired textures and defects as shown in **Figure 5.3**. See Supporting Information for more details on the visualization of these systems.

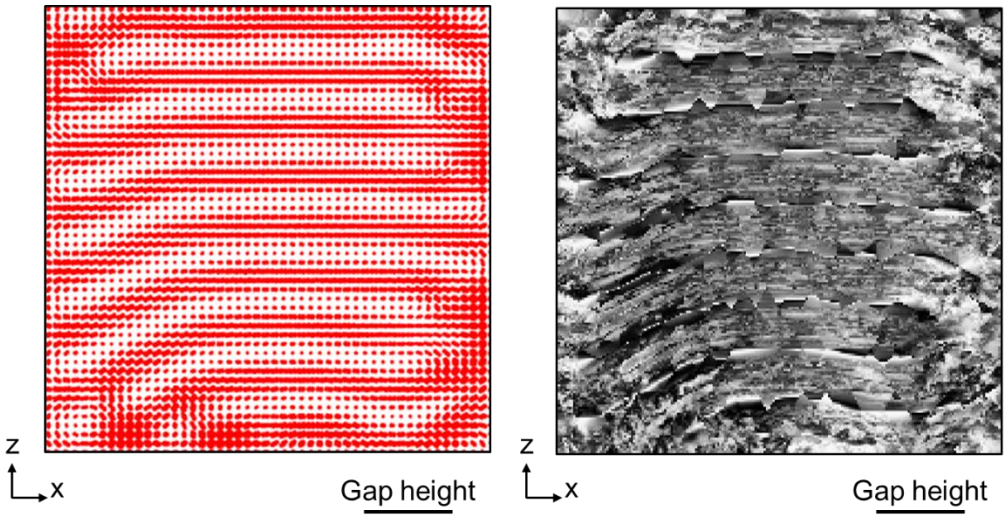

Figure 5.3: Left: The local rod orientation generated from a COMSOL solution is visualized using ellipsoids where the different radii of the ellipsoid correspond to the eigenvalues of the Q tensor. Right: Simulated Micrograph of a COMSOL solution generated from the method proposed by Ondris-Crawford et al.[75] (Reprinted with permissions from American Chemical Society: *Langmuir* 34, 44, 13274-13282, Orientation Relaxation Dynamics in Cellulose Nanocrystal Dispersions in the Chiral Liquid Crystalline Phase, M. J. Pospisil, P. Saha, S. Abdulquddos, et al. Copyright 2018 American Chemical Society). [43]

5.3 Simulation Methods

To mimic the cessation of shear in experiment, we aligned the system in the flow direction and assumed all inertial effects due to shear were negligible. The aspect ratio of the solution box was set to 5 where the shear dimension was the shortest in order to minimize confinement effects in the flow and vorticity directions. All boundary conditions for the system were set to isotropic in order to prevent any preferred orientation at the surface of the glass slides and at the edges of the dispersion. The initial condition for the system was assumed to be flow-aligned which corresponds to the high degree of flow alignment seen

in previous Rheo-optic, Rheo-SANS, and Rheo-SAXS experiments that also used CNC mesogens at the same shear rate of 100 s^{-1} and above.[24,97,98] The finite-element method (FEM) utilized by COMSOL Multiphysics was used to solve equation 0-2 in three dimensions. Each simulation consisted of at least ~162,000 degrees of freedom and was allowed to achieve steady state. Further analysis with higher degrees of freedom were conducted on the simulations to ensure numerical accuracy and convergence. The following results and discussion section show how chirality and shear cell confinement alter helical microstructure formation in a system where all directional degrees of freedom are present. It is important to note that in our current study, many of the parameters of the model are not known experimentally. In practice, we use the Landau-de Gennes equation to generate simulated microstructures so that the experimental and simulated microstructures (and pitch/gap height values) can be compared and real trends relating to chiral strength and other parameters can be determined.

5.4 Results & Discussion

Time-dependent simulations whose initial state was flow-aligned were created and run until steady state was reached. In our simulations, we parametrically varied gap spacing and chiral strength since these have clear experimental analogs. In experimental settings, the chiral interaction between the nematic mesogens can be tuned by pH, concentration, and counter-ion choice. Similarly, confinement effects in the experiment can be varied by changing the distance between the shear plates in the shear cell.

First we examine how confinement affects the steady state of the system. Then we show how chiral interactions affect the steady-state of the system. Finally we show how a flow aligned state develops into a steady-state homeotropic configuration. For the purpose of comparison, we explicitly use the 5.14 vol% sample because it is less prone to drying due to a shorter relaxation time when compared to a fully liquid crystalline sample. Our previous work also indicates that highly concentrated biphasic samples just below the biphasic-liquid crystalline phase transition generate better thin films for applications.[99]

5.4.1 Gap Height

Our data indicates that increasing the gap height causes a loss in microstructure uniformity and the development of more complicated helical configurations**.** According to **Figure 5.4**, given a small enough gap height, H, homeotropic configurations dominate the system. These xz-slices in the 1H case exhibit a large constant pitch in which helical directors orient exclusively in the xz-plane as indicated by the black dashed line. Furthermore, the yz-slices show little defect formation indicative of uniformity in the shear direction. As the gap height is increased to 2H, the system appears to show two dominant helical directors as the upper and lower halves of the system are offset by a small angle of rotation ($y = 0.35$ and $y = 0.65$). Due to the competing helical directors, uniformity is lost in the yz-slices which indicates the transition from strict homeotropic configurations to more defect-laden structures. At large enough gap heights, 4H, complex configurations appear as fingerprint textures develop in both the shear and flow directions as is evident

in the xz and yz-ellipsoid maps. The 4H case also shows lots of defects and no average helical director is established.

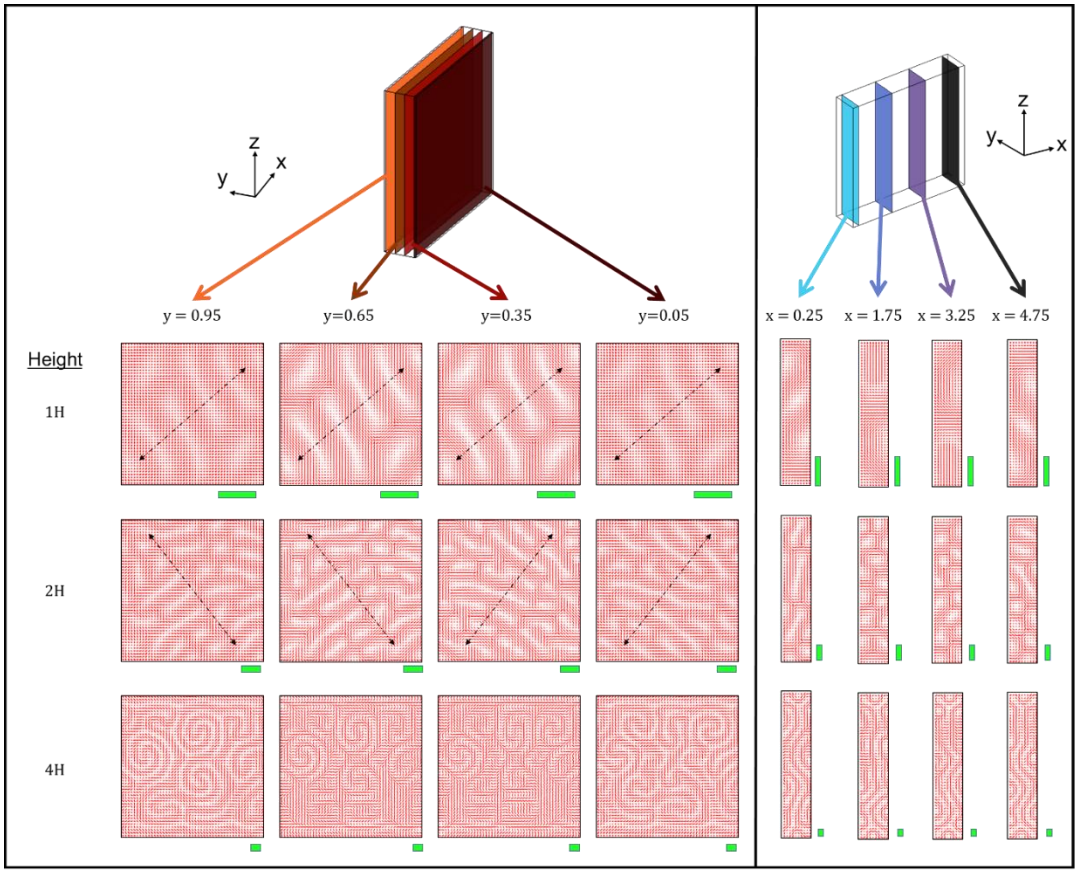

Figure 5.4: Ellipsoid maps that show local rod alignment taken at discrete slices within the 3D model. The dashed black arrows indicate the average helical director in each slice. These results indicate distinct uniform homeotropic helical orientations develop at very low gap heights and transition into much more complex 3D structures at larger gap heights. The green scale bars are equal to dimensionless gap height H. (Reprinted with permissions from American Chemical Society: *Langmuir* 34, 44, 13274-13282, Orientation Relaxation Dynamics in Cellulose Nanocrystal Dispersions in the Chiral Liquid Crystalline Phase, M. J. Pospisil, P. Saha, S. Abdulquddos, et al. Copyright 2018 American Chemical Society).[43]

We now discuss the steady state configurations of the simulations seen in **Figure 5.4** in terms of thermodynamic penalties associated with the system. Homeotropic helices form at small gap heights (1H xz-ellipsoid maps of **Figure 5.4)** due to the close proximity of the shear boundaries. This homeotropic orientation is the preferred orientation of the system because the thermodynamic penalty associated with non-uniformity next to the boundary is more easily overcome by the chiral strength term than the thermodynamic penalty associated with the confinement of the system. At larger gap heights, 2H, the thermodynamic penalty associated with confinement is decreased and causes the system to have more rotational freedom which allows two helical directors to form, while still maintaining homeotropic structures. At sufficiently large gap heights, complex microstructures develop as local helical directors form in all directions due to the smaller roles played by penalties associated with confinement and non-uniformity near the boundaries.

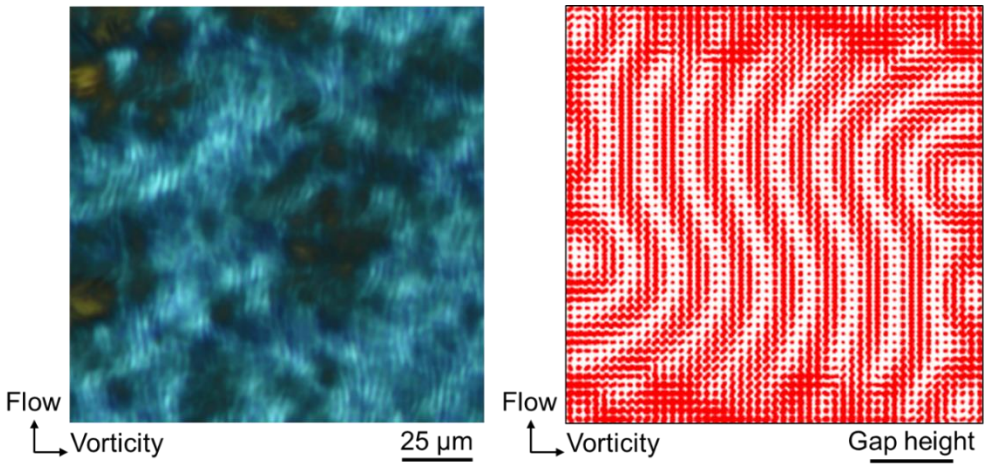

Figure 5.5: Experimental cross-polarized transmitted micrograph of a 5.14 vol. % CNC dispersion with a shear cell gap of 50 µm and simulated ellipsoid map at the smallest gap height show texture alignment in the flow direction.[43] (Reprinted with permissions from American Chemical Society: *Langmuir* 34, 44, 13274-13282, Orientation Relaxation Dynamics in Cellulose Nanocrystal Dispersions in the Chiral Liquid Crystalline Phase, M. J. Pospisil, P. Saha, S. Abdulquddos, et al. Copyright 2018 American Chemical Society).[43]

While our experimental setup is limited in identifying complex three-dimensional helical configurations, the experimental results show that under the smallest experimental gap height (50 µm), the dispersion displays uniform homeotropic helices at equilibrium, a result which is verified by the simulation (**Figure 5.5**). Even though the equilibrium pitch varies between the experiment and the simulation, a result of unknown parameter fitting, the similarity in texture indicates the model's accuracy in predicting similar microstructure formation in the dispersion.

5.4.2 Increasing chiral strength

Our results also indicate that chiral strength influences helical orientation. The chiral strength term, θ, is a function of the chiral Frank elastic constant K_t and is analogous with the magnitude of chiral interactions. Dispersion pH, ionic strength, temperature, concentration, and counter-ion choice are all factors that affect these chiral interactions. In general, the equilibrium pitch decreases with increasing chiral interactions (chiral twist power$\propto$ 1/pitch).[96] These interactions are caused by the electric double layer that surrounds each individual rod, which is formed by the charge carried on the mesogen and the ions that are present in the solvent. It has been shown experimentally that additional electrolyte in these dispersions suppresses these double layers and creates a smaller equilibrium pitch due to stronger chiral interactions.[96] Likewise, increased concentration causes stronger chiral interactions as rod spacing decreases and results in an increased twist in the chiral nematic.[100] It has also been shown that counter-ion choice alters the size of the double layer and causes different microstructural responses upon shear due to electroviscous effects.[101] In order to probe these experimental parameters, we varied the value of K_t in our model by increasing θ, and then generated ellipsoid maps to display the different configurations in each steady state (**Figure 5.6**).

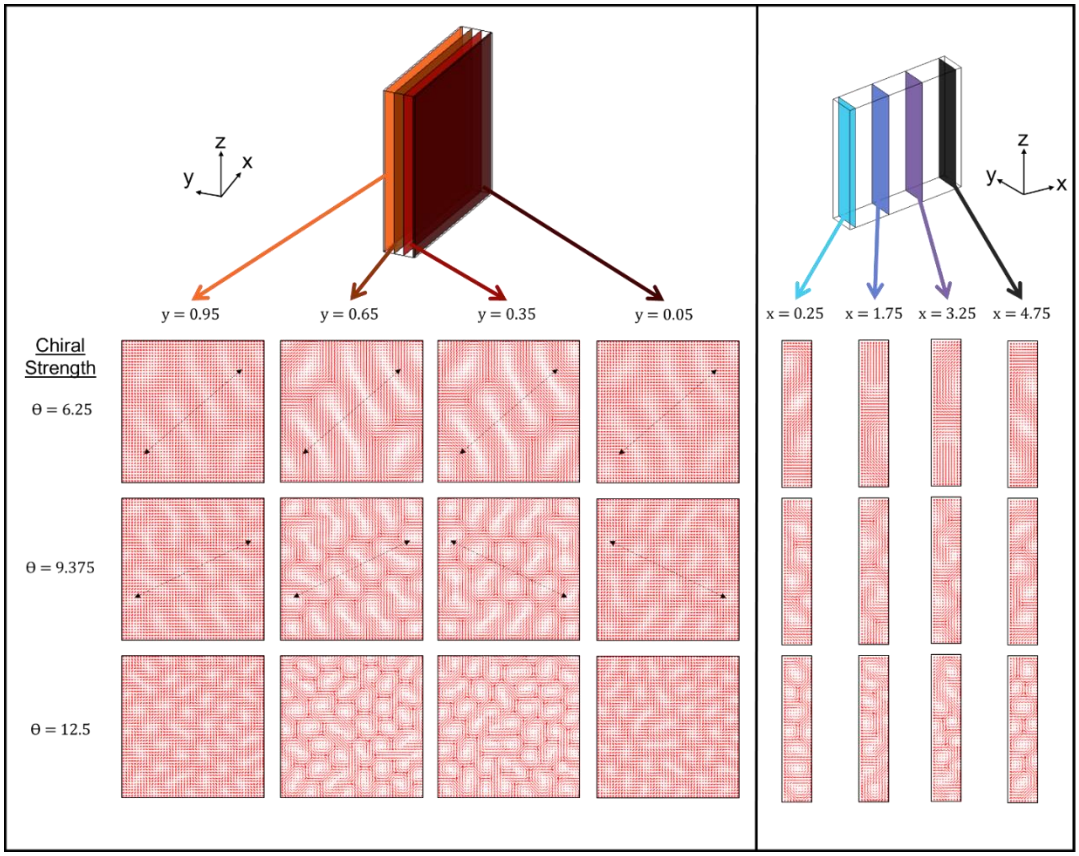

Figure 5.6: Increasing chiral interactions via increased θ causes a shift from a uniform homeotropic configuration to a complex 3D structure. Images are individual slices of the solution space that show ellipsoid maps which are representative of local rod orientation. The dashed black arrows indicate the average helical director in each slice. R = 28.125 for all simulations shown above. The green scale bars are equal to dimensionless gap height H. (Reprinted with permissions from American Chemical Society: *Langmuir* 34, 44, 13274-13282, Orientation Relaxation Dynamics in Cellulose Nanocrystal Dispersions in the Chiral Liquid Crystalline Phase, M. J. Pospisil, P. Saha, S. Abdulquddos, et al. Copyright 2018 American Chemical Society) [43].

At θ = 6.25 homeotropic helices form and have directional uniformity as shown in **Figure 5.6**. As chiral strength increases (θ = 9.375), shorter striations in texture can be seen, and the pitch length decreases. Directional uniformity in consecutive zx-slices is also not as prevalent as it was in the θ = 6.25 case. This suggests that the system undergoes a transition

from homeotropic to a more complex three dimensional structure as chiral strength is increased. At large theta values (θ = 12.5), the system is characterized by even more defects in the xz and yz-planes. According to the ellipsoid images, this transition from homeotropic to complicated 3D microstructures occurs within a very small chiral strength range. It is evident that in lower θ ranges fingerprint texture is apparent, but above a threshold value, the system beings to form defects in order to dissipate the increased spatial inhomogeneities, which results in no average helical director.

In the same way gap confinement results were presented, we now discuss how the same thermodynamic penalties apply to chiral strength. Small values of θ correspond to an increased double layer which by default increases the size of the helical microstructures. As a result of this increase, the penalty associated with helical formation normal to the shear boundaries becomes larger than the penalty associated with non-uniformity near the boundaries. This causes the homeotropic configuration to become the preferred orientation state. As θ is further increased (θ = 9.375), the double layer size begins to shrink and chiral interactions increase and cause a decrease in helical microstructure size (attributed to smaller pitch). The decreased double layer size also allows for more interactions between homeotropic layers which explains the rotation of the helical director in the middle of the sample. Finally, at large values of θ (θ = 12.5), strong chiral interactions develop as the double layer continually shrinks which causes unrestricted helical formation leading to complex 3D structures and a considerable number of defects as shown in **Figure 5.6**.

5.4.3 Dynamics

We now turn our attention to the fluid-phase ordering that occurs in the shear relaxation experiments. Our experimental and theoretical studies primarily focus on the development of microstructures that precede cholesteric fingerprint texture formation. In our shear cell experiment, the dispersion initially exhibited uniform birefringence as shown in **Figure 5.7** (0 min). The initial appearance of a banded texture began at 10 min and fully developed within the range of 20-25 minutes after cessation of shear. White areas represent mesogen alignment in the flow direction and dark areas represent mesogen alignment ±45° to the flow direction. A similar texture has been seen in hydroxypropyl cellulose and poly(-γ-benzylglutamate) dispersions prepared by Vermant *et al.*[102] Originally, this banded texture, seen in the 20-25 min images of **Figure 5.7**, was thought to be dependent on shear rate, but our results show that mesogen alignment occurs and band formation follows upon relaxation even at sufficiently high shear rates. A previous experiment also verified the banded texture to be independent of shear in nematic systems. Experiments conducted by Lonberg *et al.* utilized a magnetic field, rather than mechanical shear, to induce rod alignment and observed a similar band formation even after its removal.[103] In our experiment, the banded texture further relaxed and led to a homeotropic cholesteric texture 75 minutes after cessation of shear. This result shows that the fingerprint texture can be recovered, given adequate relaxation time, even after high shear.

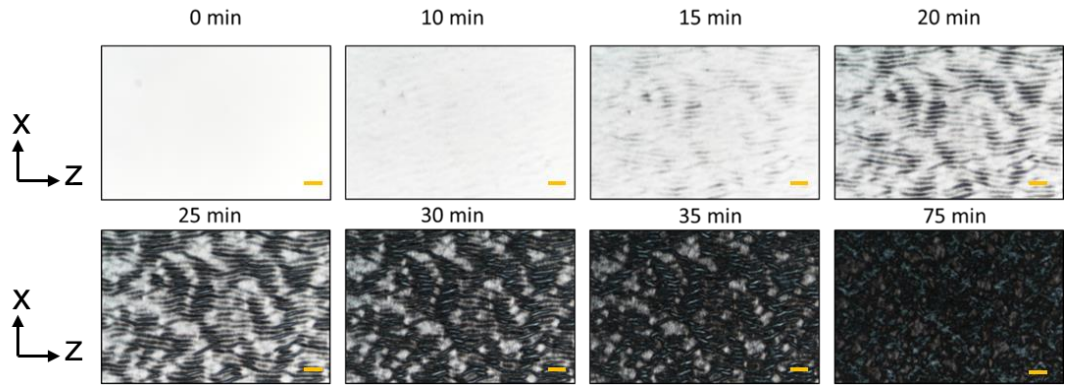

Figure 5.7: 5.14 vol% CNC dispersion after cessation of 100 s^{-1} shear with a 50 µm gap height. The system initially shows uniform birefringence that yields to a banding texture before reaching the steady state fingerprint texture characteristic of chiral nematics. The orange scale bar is equal 50 µm. (Reprinted with permissions from American Chemical Society: *Langmuir* 34, 44, 13274-13282, Orientation Relaxation Dynamics in Cellulose Nanocrystal Dispersions in the Chiral Liquid Crystalline Phase, M. J. Pospisil, P. Saha, S. Abdulquddos, et al. Copyright 2018 American Chemical Society) [43].

To compare simulations with the experiments, we chose a parameter set that resulted in a homeotropic orientation and examined the system's dynamics. To emulate the pre-aligned state seen in our experiments and those observed in the experiments of Lonberg *et al.*, we assumed a flow aligned initial state.[103] The simulation was allowed to relax in time and the dynamics of the simulation were captured for comparison. **Figure 5.8** shows the simulation's transition from a perfectly shear aligned state to the homeotropic helical case.

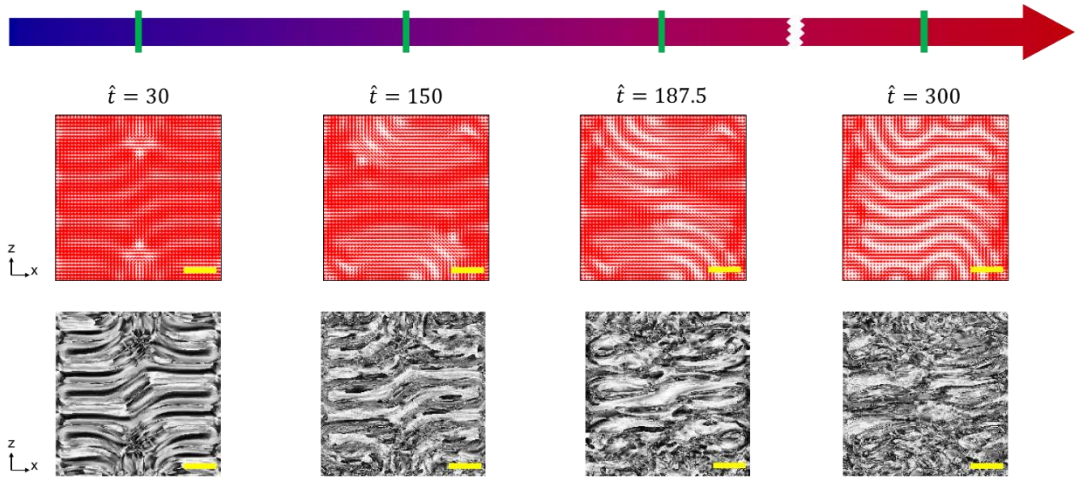

Figure 5.8: Top: Ellipsoid maps showing banding patterns and fingerprint texture of solution at values of $\hat{\mathbf{t}}$ ($\hat{\mathbf{t}} = {}^{\mathbf{t}}/_{\boldsymbol{\tau}}$). Bottom: Simulated micrographs of solution showing similar banding patterns and fingerprint textures at values of $\hat{\mathbf{t}}$. The yellow scale bars are equal to dimensionless gap height, H. (Reprinted with permissions from American Chemical Society: *Langmuir* 34, 44, 13274-13282, Orientation Relaxation Dynamics in Cellulose Nanocrystal Dispersions in the Chiral Liquid Crystalline Phase, M. J. Pospisil, P. Saha, S. Abdulquddos, et al. Copyright 2018 American Chemical Society).[43]

As shown in **Figures 5.7** and **5.8**, both the experiment and simulation show the formation of a cholesteric texture with well-defined pitch. The characteristic feature size in the simulation starts at a large value $\hat{t}$ = 30 and then drops off until steady state is reached ($\hat{t}$ = 300). In the experimental results, mesogens generate large banded structures (10-25 min) that continually shrink in width until equilibrium pitch (75 min) is established. While the simulation appears to form banded texture perpendicular to the experiment, the bands shown in the early simulation (**Figure 5.8**, $\hat{t}$ = 30 - 187.5) do not represent the same ones seen in the 10-25 min range of our experiments. Rather, the bands seen in the dynamic simulation represent the formation of helices due to mesogen alignment that occurs shortly

after the cessation of shear in the experiment. Similar helical formation is seen occurring in between banded texture of the experiment as it moves in time.

5.5 Conclusion

In this work, we utilized a Landau-de Gennes formalism to capture the relaxation dynamics of a lyotropic cholesteric liquid crystalline dispersion upon the cessation of shear. Our formalism takes into account both short-range and long-range elastic effects with an added chiral force term to cause helical distortions. Both homeotropic and complex 3D configurations were shown to develop under different parameters as a result of the competition between increased spatial distortion and gradient-penalizing elastic terms. From our simulation results, we created ellipsoid maps that show the possible helix orientations as functions of gap height and chiral strength. Our dynamic simulations also probed the banding textures seen in the relaxation of chiral liquid crystalline systems and displayed an initial banding texture prior to the equilibrium fingerprint texture. Our simulation and experimental results hold importance for controlled microstructure formation in shear processing of cholesteric liquid crystalline films.

CHAPTER VI

MODELING OF CELLULOSE NANOCRYSTAL ASSEMBLY IN LIQUID CRYSTALLINE FILMS

6.1 Introduction

Cellulose nanocrystals (CNC) are a biodegradable, cost effective, readily abundant nanomaterial that have gained interest due to their ability to form photonic thin films. These nanomaterials are derived from biomass and extracted via sulfuric acid hydrolysis. Depending on the biomass source, acid hydrolysis generates nanocrystals varying between 3-20 nm in width and 50-1000 nm in length and places negatively charged sulfate half esters and hydroxyl groups on the surface of the nanocrystals.[1,51,104] The addition of these charged functional groups on the surface induces a zeta potential of ~ -40 (mV) allowing them to remain stable in colloidal suspension and spontaneously self-assembly into chiral nematic phases at significantly high concentrations.[105] For these chiral nematic systems, the local orientation of the (CNC) mesogens can be described by a director ***n***, which rotates counter-clockwise in a helical fashion. This forms a left handed helical microstructure which is oriented normal to the director. The distance required to complete a full rotation defines the helical pitch length, P, which represents the characteristic length scale of the system. Depending on the ambient conditions and processing parameters, different helical configurations are possible, leading to different optical properties as shown in **Figure 6.1.**

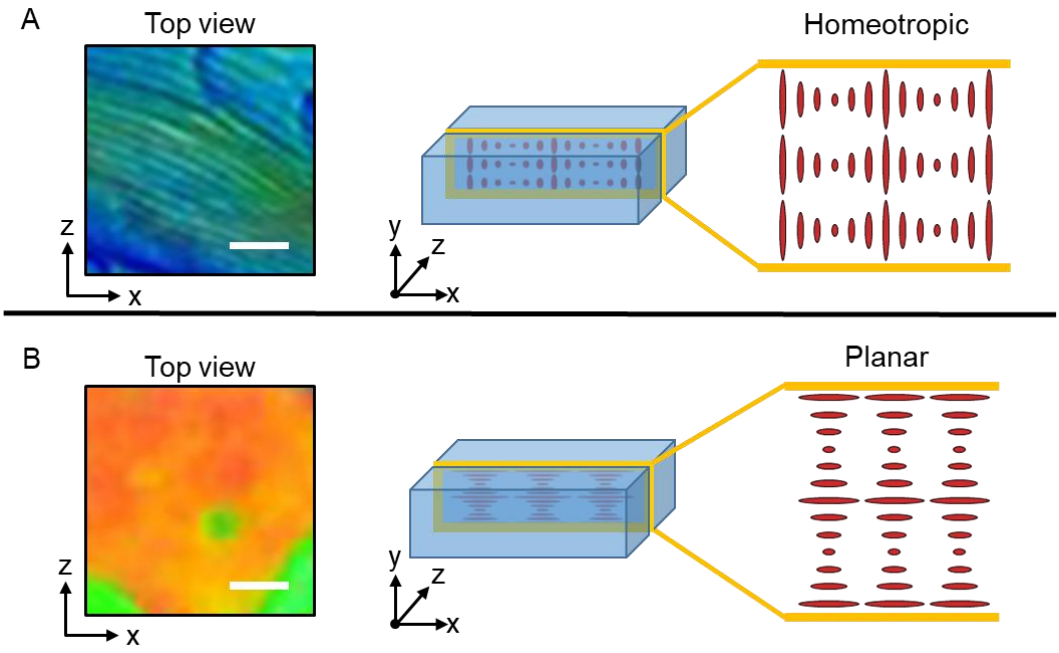

Figure 6.1: (A) Experimental selective reflection micrograph that shows the characteristic fingerprint caused by homeotropic helical orientation of CNC nematic phases. (B) Experimental selective reflection micrograph that shows uniform coloration caused by planar helical alignment of CNC nematic phases. Scale bar is 10 μm. (Experimental images adapted with permissions from American Chemical Society: *ACS Applied Nano Materials* 1, 5, 2175-2183, Photonic Properties and Applications of Cellulose Nanocrystal Films with Planar Anchoring, P. Saha, V. A. Davis. Copyright 2018 American Chemical Society).[106]

Helices that orient in plane of the sample are defined as homeotropic helices and generate the characteristic fingerprint texture shown in **Figure 6.1**. Helices that form normal to the sample are defined as planar helices and are able to reflect circularly polarized monochromatic light with the same handedness as the helical microstructure as shown in **Figure 6.1**. Helical configurations that represent a tilted planar helix are referred to as focal conic and exhibit irregularly spaced fingerprint textures. Variations in reflected

colors in planar helical configurations are directly related to helical microstructure and obey Bragg's formula given by[107,108]:

$$\boldsymbol{\lambda_{max}} = nP \cdot sin(\alpha) \qquad 0\text{-}1$$

where λ_{max} is the maximum wavelength reflected, n is the average index of refraction for the material (1.56 for CNC[109]), and α is the angle of incident circularly polarized light.

Because of their ability to selectively reflect polarized light, a considerable amount of research has been recently undertaken to generate films for tailored optical applications. These applications include mirrorless lasing, photonic reflectors, and optical sensing apparatuses such as humidity sensors for food spoilage. [1,5,7,109]. However, the challenge of producing large defect free photonic thin films on an industrial scale remains. Common causes of defect formation in the fluid phase processing of these films has been associated with incomplete fusion of chiral domains, complex vitrification, and polydispersity of the mesogens. Additionally, random helical orientations lead to complex 3D structures that form mosaic-like domains.[109] To address these issues, many parameters in the processing of thin films have been studied. Work by Park *et al.* studied the effects of orbital shear and concluded that orbital shear induces elongated anisotropic domains that fuse as a result of changes in the interfacial energy and lead to larger more uniform planar domains.[84] Other work by Wilts *et al.* studied the effects of slowly drying via a humidity controlled chamber and concluded that slower drying correlated to more uniform planar domains.[110] A recent work by Saha *et al.* studied the combined effects of both Park *et al.* and Wilts *et al.'s* results in addition to mesogen concentration and surface anchoring.[106] This work

concluded that a combination of the above parameters created the most uniform planar domains in CNC thin films.[106] Even though many of these parameters have been shown to create more uniform domains, domains are still on the order of tens of microns.[84,106]

While these results show remarkable improvement in the selective reflection of CNC films, these findings remain largely empirical. In an effort to inform upon these empirical findings, some theoretical modeling work has been accomplished. In recent work by Silvestre *et al.* wetting of a cholesteric liquid crystal was studied using a Landau de Gennes formulation. Their results showed that if the interface of the dispersion and the substrate did not distort the chiral layers the system wets similar to a nematic liquid crystal. On the other hand, if the layers become distorted topological defects form near the surface.[111] Previous work by Aguilar Gutierrez *et al.*, utilized a similar Landau de Gennes formulation to simulate drying effects in thin films. They predicted three different microstructural textures as a result of drying.[94] Their result showed that below a critical relaxation rate relative to water diffusion, mesogens self-assembled into complex non-uniform helical structures. On the other hand, systems that were above this critical ratio, destabilized the helical formation and formed films with many defects. In our prior study, the effects of confinement and chiral strength were studied on initially shear aligned liquid crystals. These simulations indicated that in a highly confined system, homeotropic helical microstructures developed whereas in spacious systems, defect laden 3D structures developed. Similarly the degree of chiral strength was shown to influence the orientation of helical microstructure. At low values of chiral strength homeotropic helices were

preferred in confined spaces, but as the value increased, 3D structures dominated the system.[43]

In an effort to further understand the formation of defects as a result of processing parameters, we report a series of 2D models for direct comparison with current experiments and the work accomplished by Saha *et al*.[106] To build upon the previous model disclosed by Aguilar Gutierrez *et al.*, we remove the following fundamental assumptions from our model: the ignored relationship between chiral strength and local concentration, the use of zero torque boundary conditions on no slip glass boundaries which do induce surface anchoring, and the use of a varying Sherwood number to induce drying in both humid and ambient atmospheres.[112]

6.2 Experiment

Previous experimental results depicted in **Figures 6.1, 6.3, 6.6** and **6.7** are taken from Saha *et al.* and we refer the reader to that work for the experimental setup.[106] For the remaining figures, a similar procedure was followed with minor exceptions. In the case of **Figure 6.5** the sample did not receive the initial orbital shear treatment followed by Saha *et al*, but rather was immediately deposited on the glass slide, covered with a coverslip and placed in the Petri dish which maintained the relative humidity.[106] For **Figures 6.8** and **6.9**, an initial shear alignment step was implemented before the sample was placed into

the petri dish. This initial shear was applied using a Gardco doctor blade coater where the shear was determined to be 1000 s^{-1}.

6.3 Formulation of Model

Our investigation studies how different parameters and methods of drying induce various helical configurations in the thin film processing of CNC dispersions. Our model consists of a Landau de Gennes formulation that captures the local representation of the second moment of the orientation distribution function, ***f(u)***, written as the second order traceless tensor ***Q***

$$\boldsymbol{Q} = \int \left(\boldsymbol{uu} - \frac{\delta}{3}\right) f(\boldsymbol{u}) d\boldsymbol{u}, \qquad 0\text{-}2$$

where ***u*** is a unit vector describing the rod orientation. We utilize a dimensionless LdG formalism similar to *Pospisil et al*.[43]

$$\frac{d\boldsymbol{Q}}{dt^*} = -6\left[(1 - \mathrm{U}/3)\boldsymbol{Q} - U\boldsymbol{Q}\cdot\boldsymbol{Q} + U(\boldsymbol{Q}\!:\!\boldsymbol{Q})\left(\boldsymbol{Q} + \frac{\boldsymbol{I}}{3}\right)\right]$$
$$+\frac{1}{R}\left[\nabla^2\boldsymbol{Q} + \frac{1}{2}\frac{L_2}{L_1}\left(\left(\left(\nabla(\nabla\cdot\boldsymbol{Q})\right) + \left(\nabla(\nabla\cdot\boldsymbol{Q})^T\right)\right) - \frac{2}{3}tr(\nabla(\nabla\cdot\boldsymbol{Q})\boldsymbol{I})\right)\right] \qquad 0\text{-}3$$
$$-\boldsymbol{P}$$

where *U* represents the dimensional nematic potential that controls the isotropic to nematic phase transition in the system and is a function of concentration, *c*. L_1 and L_2 represent the first and second Landau elastic moduli and are functions of the Frank elasticity constants. $\beta = (p^2\text{-}1)/(p^2\text{+}1)$ is a shape factor that approaches unity for rods of infinite aspect ratio and ***P*** is the chiral force contribution to the system and is written in Einstein notation as:

$$P_{ij} = \frac{\theta}{R}\left(\epsilon_{mik}Q_{mj,k} + \epsilon_{mjk}Q_{mi,k}\right), \qquad 0\text{-}4$$

where ϵ is the Levi-Civita symbol.[92]

Important dimensionless parameters derived in this model include the dimensionless quantity, *R*, and the chiral strength term, θ. These parameters are defined as:

$$R = \frac{H^2 ckT}{6L_1}. \qquad 0\text{-}5$$

$$\theta = \frac{H\hat{L}_q}{6L_1}, \qquad 0\text{-}6$$

In equation 0-5, *c* defines the rod number density; *H* defines the initial average height of the dispersion. In equation 0-6 $\hat{L}_q$ represents a combined physical constant that is the product of the chiral Landau elastic moduli and an inverse characteristic length, q_0, which is defined as 2π/pitch. Time is made dimensionless in the model via D_r which represents the rotational diffusivity of the rods. This relationship is given by:

$$t^* = D_r t \qquad 0\text{-}7$$

For modeling chiral systems, the dimensionless parameter,θ, defines the ratio of chiral strength to Frank elasticity and is responsible for the formation of distinct helical microstructures. Experiments have shown that many factors influence this term including concentration, aspect ratio, charge distribution along the mesogen, and the ionic strength of the dispersion.[95,96] It is not clear however, how each factor affects the value chiral strength individually. Many theoretical studies have been undertaken to decouple these effects, but rely on physical approximations and have yet be confirmed for CNC systems.

For the purpose of this work, we will assume that all effects are collectively encompassed in the chiral strength parameter and scale linearly with concentration.

To mimic the effects of drying a liquid crystalline dispersion, we utilized the same solvent mass transfer equation posited by Aguilar Gutierrez *et al.*[94] The equation is given as:

$$\frac{\partial c_w}{\partial t} = -\nabla \cdot \boldsymbol{j}_w; \tag{0-8}$$

$$\boldsymbol{j}_w = -(D_{iso}\nabla c_w + D_{ani}\boldsymbol{Q} \cdot \nabla c_w) \tag{0-9}$$

$$D_{iso} = \frac{D_{\parallel}+2D_{\perp}}{3} \tag{0-10}$$

$$D_{ani} = D_{\parallel} - D_{\perp} \tag{0-11}$$

where c_w is the water concentration in the dispersion, $\boldsymbol{j}_w$ is the water flux vector, and D_{iso} and D_{ani} are the isotropic and anisotropic diffusivities that are assumed to be constant and of equal magnitude and will hereafter be denoted as *D*. After nondimensionalization, the following equation represents the coupled relationship between the local rod orientation tensor $\boldsymbol{Q}$ and the spatially varying dimensionless concentration profile c_w*.

$$\frac{\partial {c_w}^*}{\partial t^*} = \Pi\nabla \cdot (\nabla^* {c_w}^* + \boldsymbol{Q} \cdot \nabla^* {c_w}^*) \tag{0-12}$$

Where Π is another dimensionless time scale ratio that defines the speed of nanocrystal rotational time to water translational time and is given by:

$$\Pi = \frac{D_t}{D_r H^2} \tag{0-13}$$

The resultant change of the film thickness *h(t)* is determined by the total water mass balance equation across the boundaries where water is evaporating, and after nondimensionalization, is given by:

$$\frac{\mathrm{d}h^*}{\mathrm{d}t^*} = \Pi\left(\frac{< j_w{}^*|_{bnd} > (t^*)}{\rho_w l^*}\right) h^*(t^*) \qquad \text{0-14}$$

where $h^*(t^*)$ is the dimensionless height, $< j_w{}^*|_{bnd} > (t^*)$ is the total dimensionless average flux evaluated at all open surface boundaries, l^* is the length of the boundary, and ρ_w is the density of water. We must note that equation 0-14 assumes a uniform height over the entire sample and is therefore the average height of the system in the vertical direction. Simulations that begin with a lower volume fraction of mesogen will naturally shrink more due to the loss of more water.

6.4 Visualization of Results

From the time dependent solution of the LdG theory, helical configurations and textures can be identified using ellipsoidal mappings and compared with experimental results. These maps represent the local orientation of the mesogen, and are generated from eigendecomposition of uniformly spaced Q tensors within the solution domain. The major axis of each ellipsoid represents the molecular director which corresponds to the scaled eigenvector whose eigenvalue is of the largest magnitude. The minor axes are drawn from the remaining eigenvectors and are scaled by their corresponding eigenvalues.

6.5 Simulation Methods

Using the previous experimental work undertaken by Saha *et al.* as the basis of our comparison, we too varied the initial concentration of the dispersion, the use of surface anchoring in the form of glass coverslips, and the effects of relative humidity through the use of initial and boundary conditions.[106] The initial concentration in the simulations were altered by the dimensionless nematic potential variable, U, which is a function of concentration. In relation to free energy, the particular value of U determines the stable thermodynamic state of the system with preference to being either isotropic, anisotropic, or both. A value of $U = 3$ corresponds to the critical concentration (5.8 vol% in the experiment) in which the isotropic phase becomes unstable. Likewise, a value of $U<8/3$ corresponds to the critical concentration in which the anisotropic phase becomes unstable. Between these critical values, both the isotropic and anisotropic domains are stable and the overall system is determined by boundary effects and thermal fluctuations.[13] (Refer to SI for more theoretical details on the thermodynamic states for binary systems). To remain consistent with the thermodynamic states of U, the isotropic initial condition is defined as $U = 2$; $c_w^* = c_w^{iso}$, and $\boldsymbol{Q} = 0$, to correspond with random alignment. Similarly, the biphasic initial condition is defined as $U = 2.9$; $c_w = c_w^{bip}$, and $\boldsymbol{Q} = 0$, so that preferential bias would not be present within the system. Lastly, the nematic initial condition is defined by $U = 3$; $c_w = c_w^{nem}$, and $\boldsymbol{Q}$ equals an aligned state that is oriented in the direction of the boundary (This is representative of a flow aligned initial dispersion). All simulations were run until the local concentrations reached the gelation threshold ($U^{gel} = 4.1$). Anchoring is applied

on appropriate boundary conditions in which a coverslip or the glass slide is present and is given by the following:

$$\boldsymbol{Q} = S^{gel}\left(\boldsymbol{n}^x\boldsymbol{n}^x - \left({}^{\boldsymbol{I}}/_3\right)\right), \tag{0-15}$$

where $\boldsymbol{n}^x$ is the unit vector oriented parallel to the boundary (x-axis) and S^{gel} is the constant order parameter given by: $S^{gel} = \frac{1}{4} + \frac{3}{4}(1 - \frac{8}{3U^{gel}})^{0.5}$. Free surfaces in the model impose a zero torque boundary for the $\boldsymbol{Q}$ tensor equation and is given by:

$$\boldsymbol{v} \cdot \frac{\partial f}{\partial(\nabla \cdot \boldsymbol{Q})} = 0, \tag{0-16}$$

where $\boldsymbol{v}$ is unit normal vector.

Finally, the flux boundary conditions for the mass transfer equation are given as:

$$j_{\boldsymbol{open}}{}^{*} = -Sh_{eff}\Pi(c_w{}^{*}) \tag{0-17}$$

$$j_{\boldsymbol{closed}}{}^{*} = 0 \tag{0-18}$$

where j_{open}* and j_{closed}* are the fluxes for a free surface and closed surface respectively. Sh_{eff} represents the effective Sherwood number that encompasses the effects of the relative humidity in the sample. The relationship between the effective Sherwood number and the real Sherwood number is given by:

$$Sh_{eff} = Sh * \frac{(1 - \gamma_{min})}{(1 - \gamma_{max})}, \tag{0-19}$$

where γ_{max} and γ_{min} represent the maximum and minimum values of the relative humidity used in the experiment respectively. The minimum value of the relative humidity is taken

to be the relative humidity of an air conditioned room (~ 40%). All simulation results are given in terms of Sh_{eff}**.**

The finite element method (FEM) utilized by COMSOL Multiphysics was used to solve eqs 3, 12 and 14 simultaneously. Each simulation shown consisted of at least ~92,000 degrees of freedom. Further analysis with more degrees of freedom was conducted to ensure numerical accuracy and convergence. The following Results and Discussion section show how concentration, surface anchoring and the degree of chiral strength alter the orientation of the helical microstructures in the final thin film. It is important to note that many of the parameters in this model are not known experimentally. In practice, these results are to be compared to real trends and used as qualitative guides for future manufacturing.

6.6 Results & Discussion

Time dependent simulations of the coupled LdG formulation and mass transfer equation were created and run to study the effects of processing parameters on microstructure self-assembly. Parameters of interest included: initial concentration of the dispersion, chiral strength, surface anchoring, and speed of drying. All simulations were run until the local concentration within the sample reached the gelation threshold (U^{gel} = 4.1 corresponding to 8 vol%). To mimic the experiment, surface anchoring was varied by inclusion of a coverslip on the top boundary as shown in **Figure 6.2** in which the mesogen assumes an aligned state and water is unable to evaporate through the boundary.

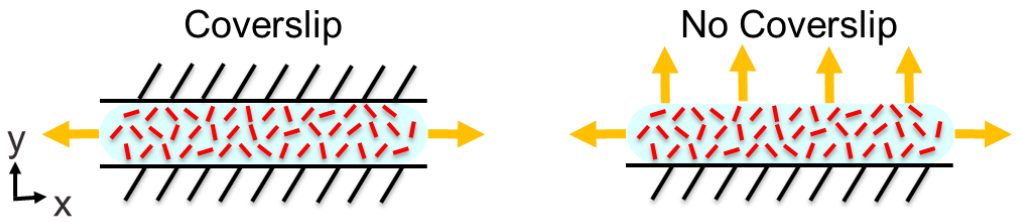

Figure 6.2: A schematic showing the free boundaries at which water is evaporated in both coverslip and no coverslip systems.

Chiral strength within the dispersion is tuned by pH, aspect ratio, and concentration. Lastly, speed of drying is altered by the dimensionless effective Sherwood number which encompasses the effects of relative humidity. It is important to note that the experiments were dried until a solid film was produced whereas the simulations were stopped when the local concentration reached a value just above the gelation threshold. We assume that once kinetic arrest has occurred as a result of vitrification, the only change in the helical pitch is the result of capillary compression caused by the evaporation of water. Similarly, we assume helical orientation is fixed at the gelation concentration since mesogens are frozen and unable to reorient. Lastly, Saha *et al*'s experimental results used an orbital shear to induce preferential alignment.[106] Based on our experimental results that did not use orbital shear, we find the need of orbital shear to form large uniform planar domains be inconclusive. For this reason, the influence of orbital shear will be ignored and will remain the subject for future work.

The experimental work we aim to compare with is our current experiments and those previously reported by Saha *et al.* and Park *et al.*[49,106] We acknowledge that both Saha *et al.* and Park *et al.* used different initial concentrations and had conflicting views as to which initial concentration preformed the best to create uniform selective reflectance. [49,106] Previous experiments from Saha *et al.* found that highly concentrated biphasic dispersions were the optimal starting dispersion to develop uniform planar microstructures. In contrast, Park *et al*. found that fully liquid crystalline dispersions performed better.[84,99,106] With our model, we will not only show similarities between our results and the experiments, but also shed light on the discrepancy between the experiments.

6.6.1 Concentration Studies

To understand the effects of concentration, experiments and simulations of three dispersions with different initial concentrations were studied. As shown in **Figure 6.3**, our data indicates that initial concentration of the dispersion heavily influences the number of defects and the types of helical configurations that are possible.

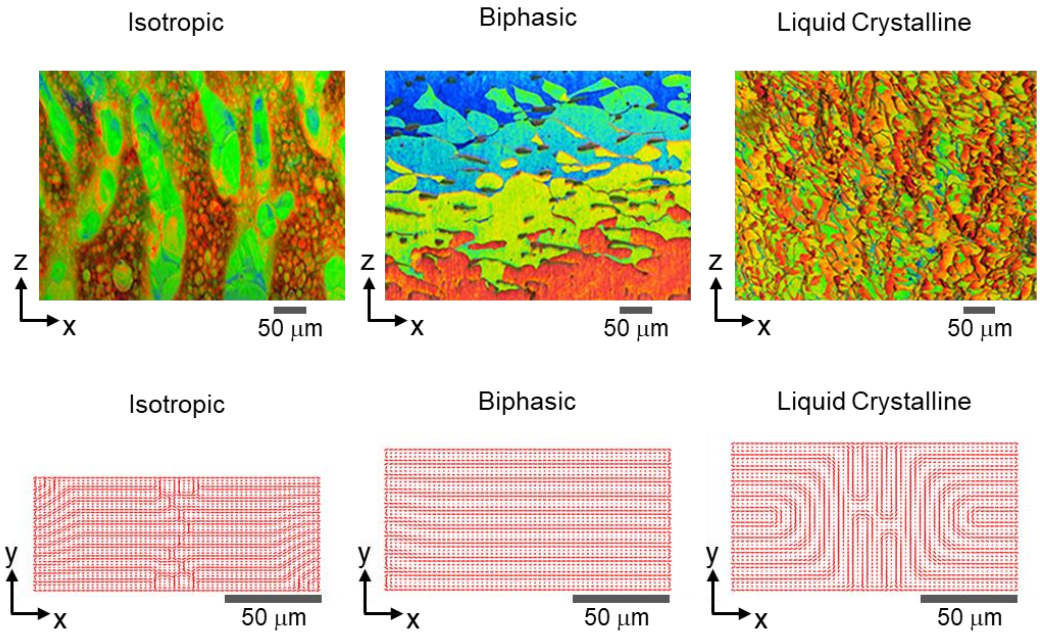

Figure 6.3: Top: Reflective microscopy of dried CNC films made from isotropic, biphasic, and liquid crystalline CNC samples. Bottom: Ellipsoidal maps depicting microstructures and textures of gelating dispersions from various concentrations. The coverslip method is applied to both the simulations and experiments shown. (Experimental images adapted with permissions from American Chemical Society: *ACS Applied Nano Materials* 1, 5, 2175-2183, Photonic Properties and Applications of Cellulose Nanocrystal Films with Planar Anchoring, P. Saha, V. A. Davis. Copyright 2018 American Chemical Society).[106]

As shown, the films in the experiment were prepared from 2.0 wt% (1.3 vol%), 6.5 wt% (4.2 vol%) and 8.0 wt% (5.1 vol%) CNC dispersions and are classified as isotropic, biphasic, and fully liquid crystalline dispersions respectively. To mimic the experiments, our simulation initially started with the nematic potentials equal to 2, 2.9, and 3 and were run until gelation. These potentials correspond to isotropic, biphasic and liquid crystalline respectively. In the experiment, the dispersion that initially starts out isotropic develops many defects and exhibits both homeotropic and planar helices. The elongated regions in

the isotropic sample of **Figure 6.3** show a distinct green reflectance which indicates that planar helices are present and exhibit a relatively constant pitch length. The rest of the image is full of smaller regions with varying reflectance. Some of these regions have the characteristic fingerprint exhibited by homeotropic helices. The loss of uniformity in selective reflectance has been associated with incomplete fusion of tactoid regions.[84] Disruption of tactoid fusion is often associated with higher viscosities in the dispersions due to the evaporation of water. This allows kinetic arrest to commence due to slow relaxation of the CNCs relative to the speed of drying. In comparison, the simulation also shows an incomplete fusion of chiral domains. These regions of planar helical formation begin as a result of the local concentration increasing beyond the threshold in which the nematic phase is stable. As the system dries, a competition between the internal elastic forces, boundary elastic forces and chiral elastic forces develop. Based on the results, it is evident that the planar helical orientation is preferred, but as the drying fronts approach each other (from the edges towards the center) the system exhibits distortion due to the inability to remove the elastic energy as gelation occurs and arrests the mesogens during their relaxation. This comparison indicates that the isotropic phase is subject to many defects due to slow relaxation relative to kinetic arrest and incomplete fusion of domains. It has been shown computationally that in the limit that rod relaxation time is fast relative to the drying speed, isotropic systems develop into uniform samples.[94]

The large bands of uniform color seen in the film generated from drying the biphasic sample indicates large uniform domains of planar helices. This phenomenon is caused by

more complete fusion of tactoids in the dispersion. This is likely due to the decreased number of fusion events since tactoids with constant pitch lengths are larger. Similarly, the simulation also shows uniform planar structures. Early dynamics of the biphasic simulation show nucleation of the chiral phase from the boundary which grows normal to the coverslip. With the higher concentration in the biphasic phase, the elastic effects induced by the boundary overcome nucleation due to the drying front. This causes only two fronts to form and approach each other. As these two fronts eventually meet at the center, the symmetry of the system due to the coverslip generates the uniform texture shown. This is in contrast to the isotropic case where fronts approach from the boundaries and the drying fronts. As the local concentration approaches the gelation point, these fronts intersect. The additional frustration caused by multiple fronts interacting with limited relaxation time causes incomplete fusion. In this simulation, the chiral front approaches the center from the directions normal to the free surface as the elastic effects induced by the boundary are weaker than the elastic effects stemming from the nucleation on the drying front. As internal concentration continues to increase, the boundary elastic effect inevitably overcomes the drying front and forms two new fronts normal to the glass slide and the coverslip. As they meet, defects develop as shown. This comparison indicates that as the number of fusion events increase the likelihood of defects also increase.

Lastly, the experimental liquid crystalline phase shows the most defects and had the smallest domains out of all the samples tested. This has been attributed to increased viscosity and less time for the relaxation to occur since the initial concentration is much

closer to gelation. For the simulation that represents an initial liquid crystalline phase, the initial condition was assumed to be aligned in the vorticity direction (normal to the glass slide and into the page). We recognize that in a true liquid crystalline phase, the orientation of individual mesogens would naturally have more variation, but we argue that the comparison suffices as the system is predisposed to form a planar helix due to elastic boundary effects. From the simulation results, uniform planar helices form along the edge due to the choice of initial conditions but quickly turn into defect laden structures in the center. These defects are a result of the competition between the elastic effects present in the system and are the result of kinetic arrest before the system is able to reorient.

In summary, the experimental and simulation results indicate that the most uniform planar structures are generated from biphasic dispersions due to decreased fusion events and longer relaxation times. This is in contrast to the experimental work done by Park *et al*. who observed that the liquid-crystalline phases resulted in the largest domains in experiments done without a coverslip.[84] It was argued by Saha *et al.* that this was the result of faster drying times and the use of a different cellulose feedstock with a different counter-ion.[106] It has been shown experimentally that the choice of feedstock has been shown to vary the aspect ratio by one to two orders of magnitude.[46] Similarly, the choice of counter-ion has been shown to alter the Debye radius and even the ionic strength at high enough concentration. These electrostatic interactions directly affect the spacing of CNCs relative to each other.[95,96] In order to probe these effects seen in the experiments, we now turn our attention to chiral strength which is the analogous parameter in the model.

6.6.2 Chiral strength

In an effort to address the influence of chiral strength, simulations that employed double surface anchoring (coverslip) and varied chiral strength and concentration were run until local gelation was reached throughout the sample. Results are shown in **Figure 6.4**.

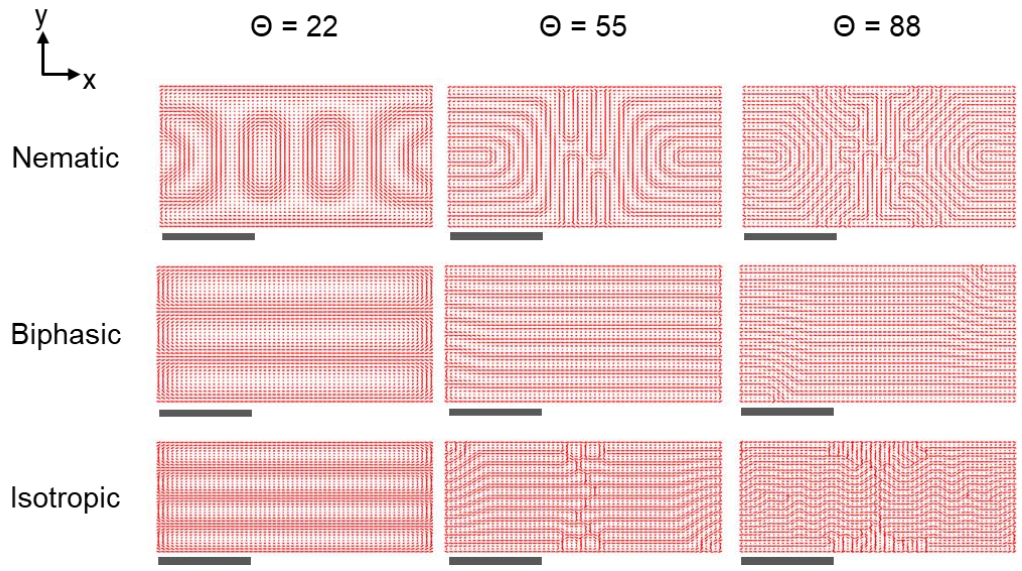

Figure 6.4: Ellipsoidal maps that depict helical structures of gelated films generated from various initial concentrations as a function of increased chiral strength. These simulations are modeled with double surface anchoring (coverslip). Scale bar is 50 μm. $Sh_{eff} = 3$.

For the nematic case (in which the initial alignment is in the vorticity direction), it is evident that the value of chiral strength greatly alters the helical orientation in the final microstructure. At low θ values it appears that the preferred helical orientation is the homeotropic configuration. This indicates that confinement effects dominate the system in which the helical director of the chiral nematic must orient parallel to the glass slide

and coverslip. This minimizes the free energy increase from the thermodynamic penalty associated with the competition of the boundary and the gradient penalizing elastic forces against the chiral elastic forces. As chiral strength is increased, the pitch length decreases and the system overcomes the penalty associated with the competition of elastic effects along the boundary and forms planar helices on the edges. The center of the gel still contains defects, but these are due to kinetic arrest as the mesogens are unable to relax completely. At high θ values, the system shows an even smaller pitch with increased distortion and defects as chiral elastic forces begin to dominate both the gradient penalizing and boundary elastic forces. The biphasic simulations all appear to exhibit relatively uniform planar structures regardless of the chiral strength. This is likely due to the nucleation and growth of the chiral fronts normal to the glass boundaries. There are, however, minor defects at the edges of the sample at higher values of chiral strength. This is due to increased distortion which is likely eliminated with a slower relaxation time. Lastly, the low θ isotropic simulation shows uniform planar helices. Defects are not present in this simulation because the chiral strength is strong enough to overcome the gradient penalizing elastic forces, but not strong enough to form defects. This is in contrast to the larger θ values that form defects as the chiral strength becomes sufficiently high enough to generate a different chiral front as concentration increases. From these results, it is evident that chiral strength does in fact alter the final helical orientation and the number of defects present. We refer the reader to the SI for the simulations completed without a coverslip.

6.6.3 Surface Anchoring

Experiments where biphasic dispersions were dried with and without a coverslip were undertaken and compared against their corresponding simulations to determine the effects of surface anchoring. To minimize the effects of drying, the experimental samples were allowed to evaporate slowly in 98% relative humidity environment. The results are shown in **Figure 6.5**.

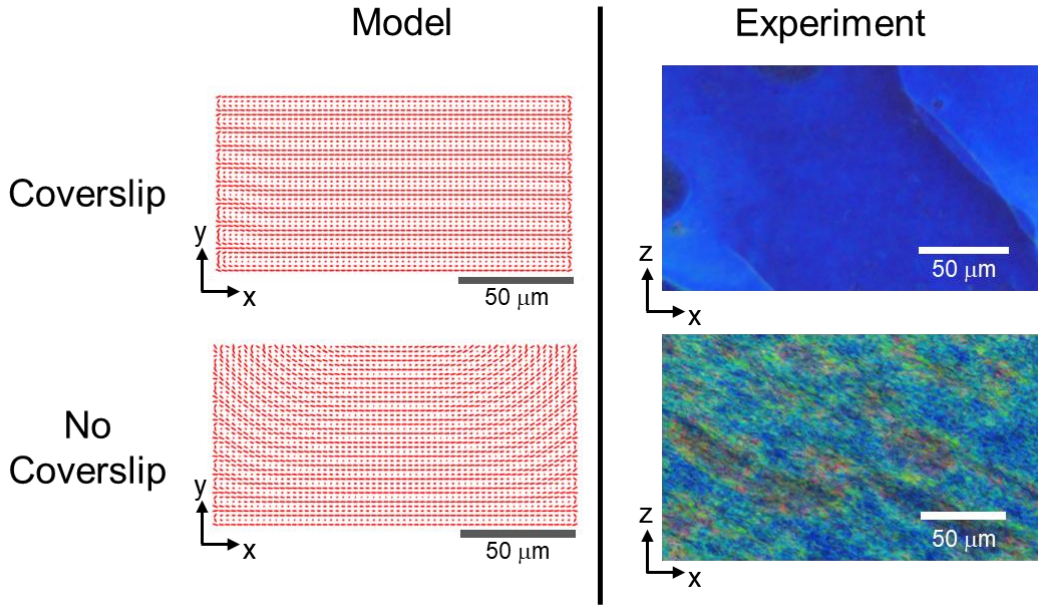

Figure 6.5: Model: Ellipsoid maps depicting helical microstructures of gelated films as different coverslip methods are applied. Experiment: Reflective microscopy of films generated from a biphasic CNC dispersion are shown with different coverslip methods. $Sh_{experimental}$ ~ 0.5 – 2.5 and Sh_{eff} = 3.

Experimental results show that surface anchoring greatly influences the size of the uniform planar domains as indicated by the consistent blue hues shown in the experiment in which the coverslip is applied. The experiment in which no coverslip, is applied however, shows a variation of colors and hues which indicates that there is less uniform planar structures than the coverslip experiment. This coincides with similar results presented by Saha *et al.* in which the experiment with no coverslip also had less planar microstructures as the sample exhibited mostly homeotropic helices with many defects.[106] The simulation in which double surface anchoring (coverslip) is applied also shows relatively uniform planar structures. The simulation in which single surface anchoring (no coverslip) is applied also appears to form some uniform planar helices in the center, but the orientation of the microstructure appears to tilt towards the edge. Experimentally this would appear as irregularly spaced fingerprints and have variation in colors as the angle of reflection off the helix varies due to the tilt.[106] This is due to the chiral front approaching from the top and sides of the sample. The center of the simulation develops uniform planar texture due to the nucleation and growth from the boundary, but as the drying front moves towards the center from the top and the sides the helix is tilted to minimize distortion caused by vitrification. These tilted orientations are seen in all simulations in which single surface anchoring is applied and can been seen in all of the figures and the SI that study no coverslip scenarios.

6.6.4 Speed of Drying/Relative Humidity

Experiments that varied the use of a coverslip were completed to elucidate the effects of drying on the formation of helical microstructures form initially biphasic dispersions. The speed of drying in these experiments was controlled by the relative humidity of the environment, and a range of Sherwood numbers was determined. Similarly, the speed of drying in the simulation was also controlled by a ratio of the relative humidity and an effective Sherwood number (Sh_{eff}) was applied. As the Sherwood numbers increase, the speed of drying increases. Results for the double surface anchoring case are shown in **Figure 6.6**.

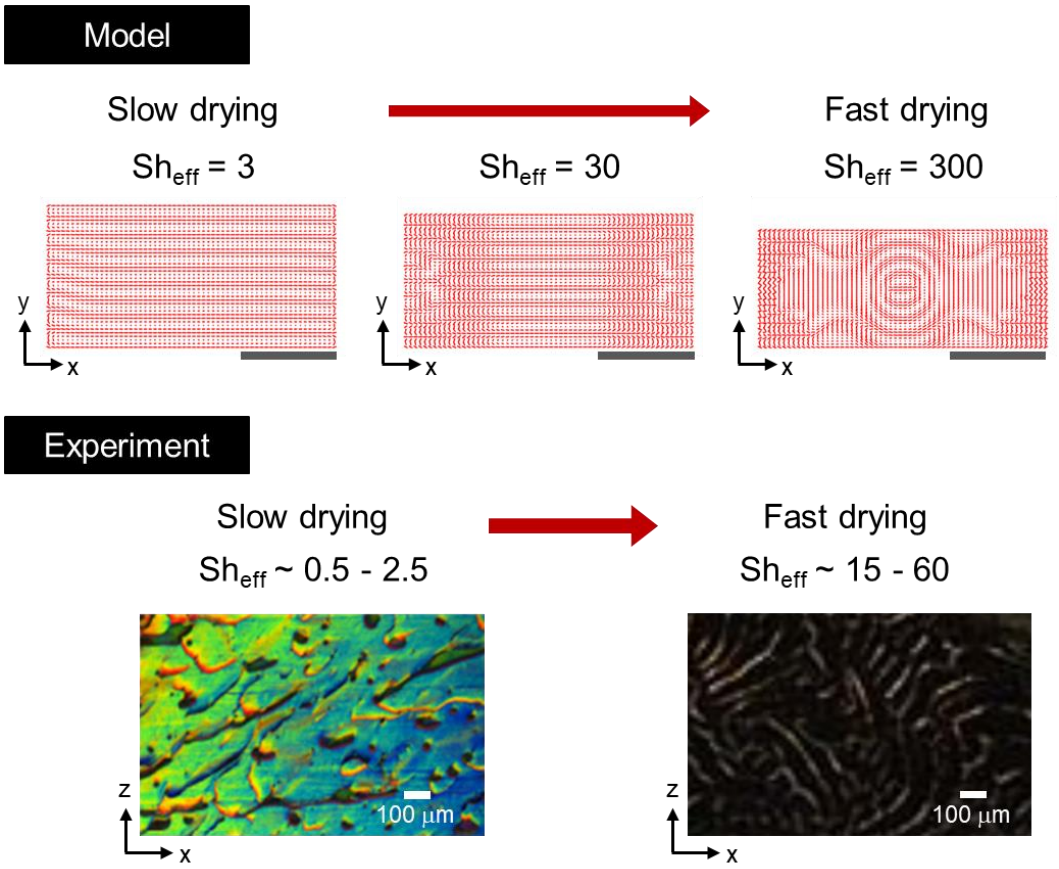

Figure 6.6: Model: Simulated ellipsoid maps of an initially biphasic CNC dispersion that show the final helical microstructure as a function of drying speed. Scale bar is 50μm. Experiment: Reflective micrograph of a biphasic CNC film showing the effects of drying on uniformity and planar helical configuration. Both experiment and simulation were generated using the coverslip method**.** (Experimental images adapted with permissions from American Chemical Society: *ACS Applied Nano Materials* 1, 5, 2175-2183, Photonic Properties and Applications of Cellulose Nanocrystal Films with Planar Anchoring, P. Saha, V. A. Davis. Copyright 2018 American Chemical Society).[106]

Experimental samples dried with a coverslip and a high relative humidity (98%) generated larger uniform planar domains with less defects than those dried with a lower relative humidity (40%). This is evident in the images of **Figure 6.6**. At slow drying conditions, pitch variation is minimal as there is only a slight blue shift from the green color in the

sample. The areas of red indicate defects, but the uniform domains are on the other of tens of microns. This is in contrast to the quick-dried sample which appears black and has the characteristic fingerprint texture associated with homeotropic helices. This is due to the onset kinetic arrest of the CNCs before they are able to relax into planar helical microstructures. This claim is verified by the simulations. At a high relative humidity, the biphasic sample is able to form uniform planar helices with a constant pitch length. The slight differences in the uniformity between the experiment and the simulation is attributed to the polydispersity of the CNCs and the increased viscosity. Regardless, the system shows large domains of uniformity. Simulations with faster drying rates show more defects as the system has less relaxation time. At Sh_{eff} = 30, uniform planar helices are show in the center of the sample, however, the edges contain minor defects. These defects indicate the premature formation of planar helices forming along the edges with a slightly smaller pitch. The fastest quick-dried simulations show even more defects and exhibits complex 3D structures as the nanocrystals in the system freeze.

Similar effects are also seen in experiments without the coverslip as shown in **Figure 6.7**. Again, both the experiment and the simulation show the highest degree of uniformity at high relative humidity and the most defects at low relative humidity. Similar to the discussion of **Figure 6.5**, while the simulations look more uniform with single surface anchoring, helices do tilt as a result of the drying front. This causes less uniformity in color. Interestingly, the fastest quick-dried simulation captured differences in chiral pitch as the as well large areas of defects at the edges.

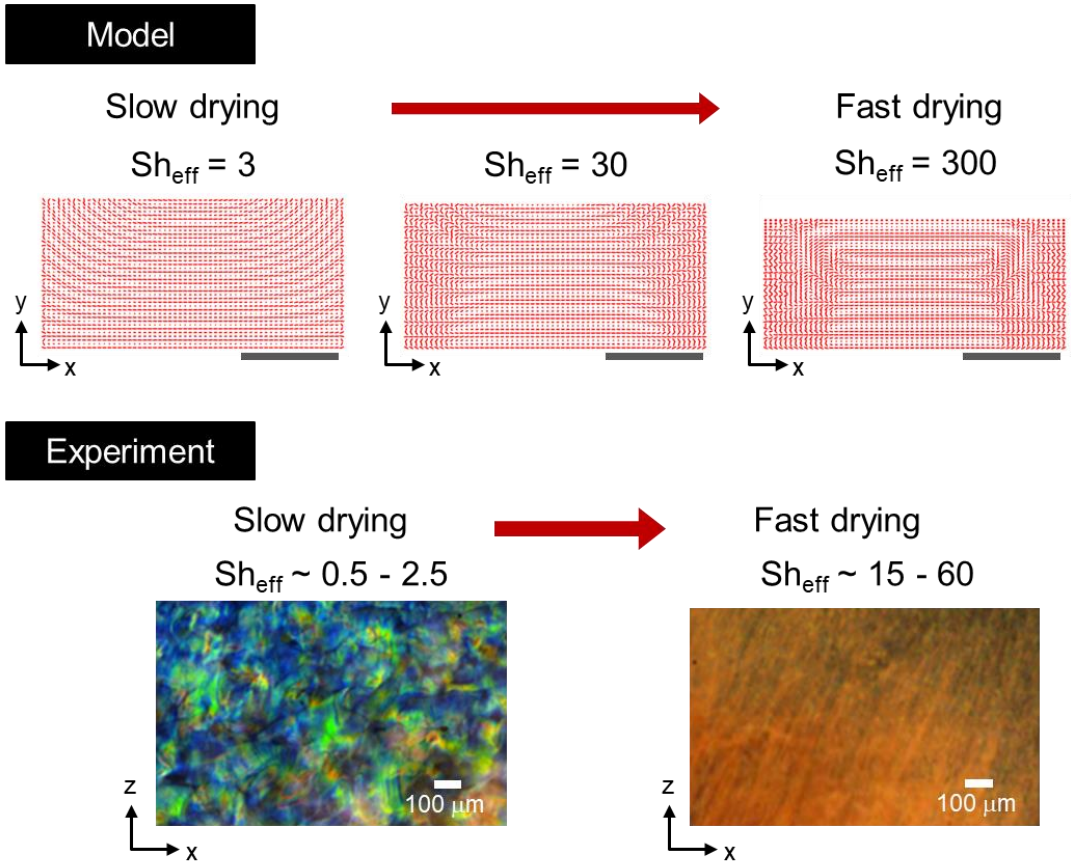

Figure 6.7: Model: Simulated ellipsoid maps of an initially biphasic CNC dispersion that show the final helical microstructure as a function of drying speed. Scale bar is 50 μm. Experiment: Reflective micrograph of a biphasic CNC film showing the effects of drying on uniformity and planar helical configuration. Both experiment and simulation were generated using the single surface anchoring (no coverslip). (Experimental images adapted with permissions from American Chemical Society: *ACS Applied Nano Materials* 1, 5, 2175-2183, Photonic Properties and Applications of Cellulose Nanocrystal Films with Planar Anchoring, P. Saha, V. A. Davis. Copyright 2018 American Chemical Society).[106]

More simulations that initially started with isotropic concentrations were run to compare, but results showed that the degree of defects increased and led to even less uniformity.

6.6.5 Shear Alignment Study

The effects of initial shear alignment was studied on films that were dried with and without a coverslip. Biphasic dispersions were used in the study since they appear to develop the most uniform planar helices. Mesogens are initially aligned in the flow direction and then left to dry in a 98% relative humidity environment. Similarly, simulations whose initial mesogen orientations are aligned in the flow direction were computed to predict the final microstructure. **Figure 6.8** shows the effect of a coverslip on an initially biphasic shear aligned sample.

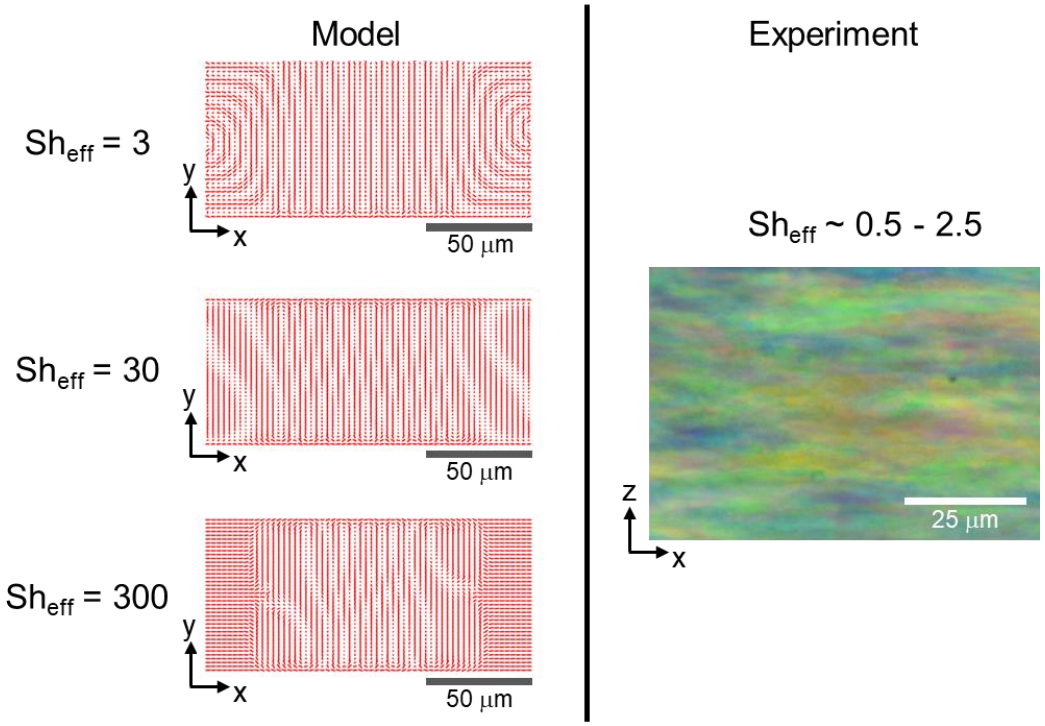

Figure 6.8: The final microstructure of initially shear aligned biphasic simulations produced using double surface anchoring (coverslip) are depicted at various drying speeds.

From the micrograph shown, it is evident that many defects developed in the microstructure based on the amount of color variation. It does appear however that there are small domains of uniform alignment, as is shown in the areas of the same color, but they appear to be on the order of a few microns. In comparison, the simulation with a similar effective Sherwood number also shows defects as well as tilted helical structures. Variation in microstructure is also present in the center of the simulation as the stripes do not appear to be perfectly normal the glass slide and coverslip. Based on these results, the simulation would show similar defective non-uniform domains of many colors and textures. As the speed of drying is increased, the amount of distortion between successive drying rates increases. Variation normal to the glass slides also increases with increased drying rates. Lastly, the fastest dried simulation shows little to no change from the initial alignment at the edges. Based on these results, flow aligned samples require more relaxation time compared to the nematic samples shown in **Figure 6.3.** This indicates that any sample that is not in an initially flow aligned state will relax faster and form larger domains of planar helices as shown in **Figure 6.3**.

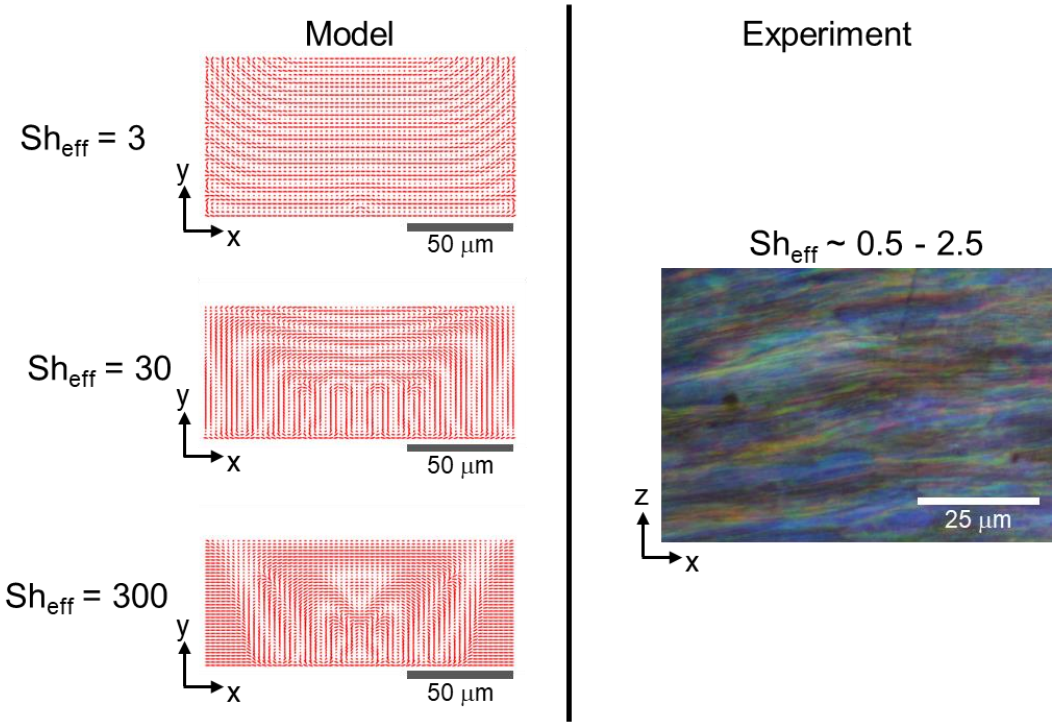

Figure 6.9: The final microstructure of initially shear aligned biphasic simulations produced using single surface anchoring (no coverslip) are depicted at various drying speeds.

Figure 6.9 shows the effects of single surface anchoring on an initially biphasic shear aligned sample. From the experimental image, it is evident that there is a large variation in color as well as a characteristic fingerprint texture throughout the micrograph. The model that corresponds to the experimental drying rate shows tilted helices which manifest into irregularly spaced fingerprint textures. These textures distort the selective reflectance which is in agreement with the experiment. Similar to the results in **Figure 6.8**, an increased drying rate causes more defects. At Sh_{eff} = 30 it is evident that homeotropic helices have formed as a result of the drying front. The fastest drying rate also shows

mesogens that did not relax from their initially shear aligned state. From these results, it can be concluded that the increased drying time needed for the relaxation of initially shear aligned samples has a greater impact on the final structure than the effects of surface anchoring as seen in both **Figure 6.8** and **Figure 6.9.**

6.7 Conclusion

In this work we used a Landau-de Gennes formalism coupled with a mass transfer equation to capture the final microstructure that forms as a result drying a chiral liquid crystalline dispersion to its gelation state. Our study was compared with previous and current experimental work and verified that the largest domains of planar helical orientation are generated from biphasic dispersions that are dried slowly in a high relative humidity environment with a secondary surface anchoring supplied by a coverslip. The effects of chiral strength were also studied, and systems with increased chiral strength appear to be more prone to develop defects whereas low chiral strength can alter the preferred orientation of the helix depending on the initial concentration of the system. This comparison, while qualitative, verifies many of the claims concluded in the experiments and holds importance in predicting future self-assembly of chiral mesogens in liquid crystalline thin film processing. In the coming years, we aim to accomplish the nontrivial task of introducing fluid flow into the LdG formalism in conjunction with constitutive equations to determine the hydrodynamic effect of an initial orbital shear. We also hope to provide an in-depth study of increased relaxation time relative to drying times in the

experiment and in the simulations. The goal of this future work is to determine if larger domains, of more uniform planar microstructures are possible in samples that are initially isotropic or liquid crystalline.

CHAPTER VII

CONCLUSIONS AND FUTURE WORK

7.1 Conclusions

In this thesis, the orientation of helical configurations as a function of different processing parameters was explored through dynamic finite element based simulations of the Landau de Gennes theory. The purpose of these simulations was to generate theoretical predictions of microstructure to compare with experiments. In this chapter, results from the Chapter 5 and 6 are summarized and future extensions of this work are suggested.

Dynamic Study of Initially Shear Aligned Dispersions

In Chapter 5, we study the effects of wall confinement and chiral strength on initially shear aligned dispersions. These dynamic simulations capture the mesogen relaxation of fully liquid crystalline dispersions using a 3D Landau de Gennes formalism. The evolution of chiral microstructures in these dispersions is caused by the chiral elastic forces overcoming the gradient penalizing elastic terms. The added influence of confinement preferentially selects homeotropic helical configurations to be exhibited in the model. These results are verified by experimental results that also show that smaller gap heights develop larger uniform domains of homeotropic helices with constant pitch.

The degree of chiral strength in the dispersion was also shown to heavily influence the orientation of the equilibrium microstructure. Low values of chiral strength generate microstructures with large pitch values which preferentially form homeotropic helices whereas high values of chiral strength develop complex defective structures. Finally, the dynamics of homeotropic helices is captured. Formation of these helices occurs from defects that form near the boundary due to spatial gradients. The break in uniformity in a shear aligned sample serves as a nucleation point for the system to evolve into homeotropic helical structures.

Planar Helical Microstructure Development in Thin Film Processing

In Chapter 6, we study the effects of multiple processing parameters in the generation of thin films from chiral liquid crystalline dispersions. This was accomplished using a similar Landau de Gennes formalism to the equation used in Chapter 5 in addition to a mass transfer equation and differential height equation to capture the evaporation of water from the sample. These simulations were run until the local concentration throughout the sample reached the gelation state. Previous experimental data was in agreement with the claims based on the results of the simulations. It was determined by both the experiment and the model that biphasic dispersions that are not initially shear aligned form the largest domains of uniform planar helices when dried slowly with additional surface anchoring. Chiral strength was also varied in the simulations and had the largest influence in initially nematic dispersions.

7.2 Future Work

It is possible to extend the dynamic simulations of Chapter 6 to three dimensional systems like the simulation in Chapter 5. Based on the degree of nonlinearity in model and the coupling of two additional partial differential equations would require more computational resources than those available at this time.

A simple extension of both models also includes substituting strong boundary conditions with weak boundary conditions along the substrate. It is has been assumed theoretically and confirmed experimentally that different substrate effects can be captured using weak anchoring .[113,114] In practice, the addition of weak anchoring in the Landau de Gennes equation requires another free energy contribution to be implemented along the boundary and minimized. The use of weak anchoring in this manner could mimic the effects of rubbing the substrate with different polymers in which mesogens align in different directions subject to the electrostatic interaction.[115]

A novel area of contribution to the formation of thin films includes a thorough study of gelation and its influence on the mesogen orientation. Current theoretical work assumes a zero torque boundary condition at the free surface interface of the dispersion.[94] This boundary condition completely ignores the interfacial energy contribution to the orientation of mesogens. A more realistic boundary condition can be employed using the

interfacial energy expression used by Croxton *et al.*[116] In addition to surface tension, increases in viscosity as a result of evaporation also need to be considered.

Finally, an incorporation of flow terms and a constitutive relationship with viscosity could be used to determine the effects of an initial linear and/or orbital shear. This would require rigorous experimental work to determine the free parameters in the constitutive equation. This becomes even more difficult as there are many experimental complexities including polydispersity of the rods and non-uniform concentrations in the dispersion. In either case, these complexities would cause non uniform viscosity measurements making it hard to determine the fitting parameters. An average could be taken of many experimental samples as a first approximation, but the consistency of results would vary based the feed stock and the degree in which the biomass was hydrolyzed. Assuming that the fitting parameters could be determined, a velocity profile of the dispersion could be determined and then solved as part of the system of equations to describe the hydrodynamic tensor.

REFERENCES

(1) Revol, J.-F.; Bradford, H.; Giasson, J.; Marchessault, R.; Gray, D. Helicoidal self-ordering of cellulose microfibrils in aqueous suspension. *International journal of biological macromolecules* **1992**, *14*, 170-172.

(2) Dong, S.; Roman, M. Fluorescently Labeled Cellulose Nanocrystals for Bioimaging Applications. *Journal of the American Chemical Society* **2007**, *129*, 13810-13811.

(3) Dumanli, A. G. m.; van der Kooij, H. M.; Kamita, G.; Reisner, E.; Baumberg, J. J.; Steiner, U.; Vignolini, S. Digital color in cellulose nanocrystal films. *ACS applied materials & interfaces* **2014**, *6*, 12302-12306.

(4) Finkelmann, H.; Kim, S. T.; Munoz, A.; Palffy-Muhoray, P.; Taheri, B. Tunable mirrorless lasing in cholesteric liquid crystalline elastomers. *Advanced Materials* **2001**, *13*, 1069-1072.

(5) Zhang, Y. P.; Chodavarapu, V. P.; Kirk, A. G.; Andrews, M. P. Nanocrystalline cellulose for covert optical encryption. *Journal of Nanophotonics* **2012**, *6*, 063516-063511-063516-063519.

(6) He, X.; Xiao, Q.; Lu, C.; Wang, Y.; Zhang, X.; Zhao, J.; Zhang, W.; Zhang, X.; Deng, Y. Uniaxially aligned electrospun all-cellulose nanocomposite nanofibers reinforced with cellulose nanocrystals: scaffold for tissue engineering. *Biomacromolecules* **2014**, *15*, 618-627.

(7) Espinha, A.; Guidetti, G.; Serrano, M. C.; Frka-Petesic, B.; Dumanli, A. G. m.; Hamad, W. Y.; Blanco, Á.; López, C.; Vignolini, S. Shape memory cellulose-based photonic reflectors. *ACS applied materials & interfaces* **2016**, *8*, 31935-31940.

(8) Zhang, Y. P.; Chodavarapu, V. P.; Kirk, A. G.; Andrews, M. P. Structured color humidity indicator from reversible pitch tuning in self-assembled nanocrystalline cellulose films. *Sensors and Actuators B: Chemical* **2013**, *176*, 692-697.

(9) Reinitzer, F. Beiträge zur Kenntniss des Cholesterins. *Monatshefte für Chemie und verwandte Teile anderer Wissenschaften* **1888**, *9*, 421-441.

(10) Lehmann, O.: Über fliessende Krystalle. In *Zeitschrift für Physikalische Chemie*, 1889; Vol. 4U; pp 462.

(11) Onsager, L. The effects of shape on the interaction of colloidal particles. *Annals of the New York Academy of Sciences* **1949**, *51*, 627-659.

(12) Frenkel, D. Order through entropy. *Nature Materials* **2014**, *14*, 9.

(13) Doi, M. Molecular dynamics and rheological properties of concentrated solutions of rodlike polymers in isotropic and liquid crystalline phases. *Journal of Polymer Science: Polymer Physics Edition* **1981**, *19*, 229-243.

(14) Wang, P.-X.; MacLachlan, M. J. Liquid crystalline tactoids: ordered structure, defective coalescence and evolution in confined geometries. *Philosophical Transactions of the Royal Society A: Mathematical, Physical and Engineering Sciences* **2018**, *376*, 20170042.

(15) Bahr, C.; Kitzerow, H.-S.: *Chirality in liquid crystals*; Springer, 2001.

(16) Hyde, S. T. Identification of lyotropic liquid crystalline mesophases.

(17) Liquid Crystalline Soft Matter. http://www.lcsoftmatter.com/page76/page1/styled-22/order.html (accessed November 5 2019).

(18) Goodby, J. W.: Materials and Phase Structures of Calamitic and Discotic Liquid Crystals. In *Handbook of Visual Display Technology*; Chen, J., Cranton, W., Fihn, M., Eds.; Springer Berlin Heidelberg: Berlin, Heidelberg, 2012; pp 1243-1287.

(19) Lesac, A.; Loc Nguyen, H.; Narančić, S.; Baumeister, U.; Diele, S.; Bruce, D. W. Bent-core mesogens based on semi-flexible dicyclohexylmethane spacers. *Liquid Crystals* **2006**, *33*, 167-174.

(20) Batchelor, G.: K. 1967 An Introduction to Fluid Dynamics. Cambridge University Press, 1970.

(21) Pasquali, M. Polymer composites: Swell properties and swift processing. *Nature materials* **2004**, *3*, 509.

(22) Davis, V. A.; Ericson, L. M.; Parra-Vasquez, A. N. G.; Fan, H.; Wang, Y.; Prieto, V.; Longoria, J. A.; Ramesh, S.; Saini, R. K.; Kittrell, C.; Billups, W. E.; Adams, W. W.; Hauge, R. H.; Smalley, R. E.; Pasquali, M. Phase Behavior and Rheology of SWNTs in Superacids. *Macromolecules* **2004**, *37*, 154-160.

(23) Lettinga, M. P.; Dogic, Z.; Wang, H.; Vermant, J. Flow behavior of colloidal rodlike viruses in the nematic phase. *Langmuir* **2005**, *21*, 8048-8057.

(24) Haywood, A. D.; Weigandt, K. M.; Saha, P.; Noor, M.; Green, M. J.; Davis, V. A. New insights into the flow and microstructural relaxation behavior of biphasic cellulose nanocrystal dispersions from RheoSANS. *Soft Matter* **2017**, *13*, 8451-8462.

(25) G. Larson, R.: *The Structure and Rheology of Complex Fluids*, 1998; Vol. 1.

(26) Montesi, A.; Peña, A. A.; Pasquali, M. Vorticity Alignment and Negative Normal Stresses in Sheared Attractive Emulsions. *Physical Review Letters* **2004**, *92*, 058303.

(27) Marrucci, G.; Maffettone, P. Nematic phase of rodlike polymers. II. Polydomain predictions in the tumbling regime. *Journal of rheology* **1990**, *34*, 1231-1244.

(28) Wissbrun, K. F. Rheology of rod-like polymers in the liquid crystalline state. *Journal of Rheology* **1981**, *25*, 619-662.

(29) Rienäcker, G.; Hess, S. Orientational dynamics of nematic liquid crystals under shear flow. *Physica A: Statistical Mechanics and its Applications* **1999**, *267*, 294-321.

(30) Baek, S. G.; Magda, J.; Larson, R.; Hudson, S. Rheological differences among liquid-crystalline polymers. II. Disappearance of negative N 1 in densely packed lyotropes and thermotropes. *Journal of Rheology* **1994**, *38*, 1473-1503.

(31) Echeverria, C.; Almeida, P. L.; Aguilar Gutierrez, O. F.; Rey, A. D.; Godinho, M. H. Two negative minima of the first normal stress difference in a cellulose-based cholesteric liquid crystal: Helix uncoiling. *Journal of Polymer Science Part B: Polymer Physics* **2017**, *55*, 821-830.

(32) Wensink, H. H.; Jackson, G. Cholesteric order in systems of helical Yukawa rods. *Journal of Physics: Condensed Matter* **2011**, *23*, 194107.

(33) Dierking, I. Chiral Liquid Crystals: Structures, Phases, Effects. *Symmetry* **2014**, *6*, 444.

(34) Friedel, G. In *Tilte*1922.

(35) Sucrowt, W.; Appel, L. Liquid C rystalline N orcholesterylesters: Influence of the A xial M ethylgroups on the Phase T ransitions and the C holesteric H elix H. Stegemeyer and K. Siemensmeyer Institute of Physical Chemistry, University Paderborn.

(36) Slaney, A. J.; Nishiyama, I.; Styring, P.; Goodby, J. W. Twist inversion in a cholesteric material containing a single chiral centre. *Journal of Materials Chemistry* **1992**, *2*, 805-810.

(37) Styring, P.; Vuijk, J. D.; Nishiyama, I.; Slaney, A. J.; Goodby, J. W. Inversion of chirality-dependent properties in optically active liquid crystals. *Journal of Materials Chemistry* **1993**, *3*, 399-405.

(38) Dierking, I.; Gieβelmann, F.; Zugenmaier, P.; Kuczynskit, W.; Lagerwall, S. T.; Stebler, B. Investigations of the structure of a cholesteric phase with a temperature induced helix inversion and of the succeeding Sc* phase in thin liquid crystal cells. *Liquid Crystals* **1993**, *13*, 45-55.

(39) Loubser, C.; Wessels, P.; Styring, P.; Goodby, J. W. Helix Inversion in the chiral nematic phase of a ferroelectric liquid crystal containing a single chiral centre. *Journal of Materials Chemistry* **1994**, *4*, 71-79.

(40) Zheng, Z.-g.; Li, Y.; Bisoyi, H. K.; Wang, L.; Bunning, T. J.; Li, Q. Three-dimensional control of the helical axis of a chiral nematic liquid crystal by light. *Nature* **2016**, *531*, 352.

(41) Kamien, R. D.; Selinger, J. V. Order and frustration in chiral liquid crystals. *Journal of Physics: Condensed Matter* **2001**, *13*, R1.

(42) Ao, G.; Nepal, D.; Aono, M.; Davis, V. A. Cholesteric and Nematic Liquid Crystalline Phase Behavior of Double-Stranded DNA Stabilized Single-Walled Carbon Nanotube Dispersions. *ACS Nano* **2011**, *5*, 1450-1458.

(43) Pospisil, M. J.; Saha, P.; Abdulquddos, S.; Noor, M. M.; Davis, V. A.; Green, M. J. Orientation Relaxation Dynamics in Cellulose Nanocrystal Dispersions in the Chiral Liquid Crystalline Phase. *Langmuir* **2018**.

(44) Ranby, B. G.: Aqueous colloidal solutions of cellulose micelles. MUNKSGAARD INT PUBL LTD 35 NORRE SOGADE, PO BOX 2148, DK-1016 COPENHAGEN, DENMARK, 1949; Vol. 3; pp 649-650.

(45) Habibi, Y.; Lucia, L. A.; Rojas, O. J. Cellulose nanocrystals: chemistry, self-assembly, and applications. *Chemical reviews* **2010**, *110*, 3479-3500.

(46) Davidson, G. 9—THE RATE OF CHANGE IN THE PROPERTIES OF COTTON CELLULOSE UNDER THE PROLONGED ACTION OF ACIDS. *Journal of the Textile Institute Transactions* **1943**, *34*, T87-T96.

(47) Araki, J.; Wada, M.; Kuga, S.; Okano, T. Flow properties of microcrystalline cellulose suspension prepared by acid treatment of native cellulose. *Colloids and Surfaces A: Physicochemical and Engineering Aspects* **1998**, *142*, 75-82.

(48) Rusli, R.; Eichhorn, S. J. Determination of the stiffness of cellulose nanowhiskers and the fiber-matrix interface in a nanocomposite using Raman spectroscopy. *Applied Physics Letters* **2008**, *93*, 033111.

(49) Lagerwall, J. P. F.; Schütz, C.; Salajkova, M.; Noh, J.; Hyun Park, J.; Scalia, G.; Bergström, L. Cellulose nanocrystal-based materials: from liquid crystal self-assembly and glass formation to multifunctional thin films. *Npg Asia Materials* **2014**, *6*, e80.

(50) Hamad, W. Y.; Hu, T. Q. Structure–process–yield interrelations in nanocrystalline cellulose extraction. *The Canadian Journal of Chemical Engineering* **2010**, *88*, 392-402.

(51) Rajala, S.; Siponkoski, T.; Sarlin, E.; Mettänen, M.; Vuoriluoto, M.; Pammo, A.; Juuti, J.; Rojas, O. J.; Franssila, S.; Tuukkanen, S. Cellulose nanofibril film as a piezoelectric sensor material. *ACS applied materials & interfaces* **2016**, *8*, 15607-15614.

(52) Oseen, C. The theory of liquid crystals. *Transactions of the Faraday Society* **1933**, *29*, 883-899.

(53) Frank, F. C. I. Liquid crystals. On the theory of liquid crystals. *Discussions of the Faraday Society* **1958**, *25*, 19-28.

(54) Priestley, E. B.; Wojtowicz, P. J.; Sheng, P.: *Introduction to Liquid Crystals*; Basic Books, 1975.

(55) Stephen, M. J.; Straley, J. P. Physics of liquid crystals. *Reviews of Modern Physics* **1974**, *46*, 617.

(56) Doi, M.; Edwards, S. F.: *The theory of polymer dynamics*; oxford university press, 1988; Vol. 73.

(57) Mottram, N. J.; Newton, C. J. Introduction to Q-tensor theory. *arXiv preprint arXiv:1409.3542* **2014**.

(58) Leslie, F. M. Some constitutive equations for liquid crystals. *Archive for Rational Mechanics and Analysis* **1968**, *28*, 265-283.

(59) Leslie, F. M. Some constitutive equations for anisotropic fluids. *The Quarterly Journal of Mechanics and Applied Mathematics* **1966**, *19*, 357-370.

(60) Ericksen, J. Anisotropic fluids. *Archive for Rational Mechanics and Analysis* **1959**, *4*, 231.

(61) Parodi, O. Stress tensor for a nematic liquid crystal. *Journal de Physique* **1970**, *31*, 581-584.

(62) Green, M. J. Computational studies of the phase behavior and dynamics of rodlike liquid crystals. Massachusetts Institute of Technology, 2007.

(63) Bhave, A. V. Kinetic theory for dilute and concentrated polymer solution study of nonhomogeneous effects. Massachusetts Institute of Technology, 1992.

(64) Onogi, S.; Asada, T.: Rheology and rheo-optics of polymer liquid crystals. In *Rheology*; Springer, 1980; pp 127-147.

(65) Doi, M.; Edwards, S. Dynamics of concentrated polymer systems. Part 1.—Brownian motion in the equilibrium state. *Journal of the Chemical Society, Faraday Transactions 2: Molecular and Chemical Physics* **1978**, *74*, 1789-1801.

(66) Doi, M.; Edwards, S. Dynamics of concentrated polymer systems. Part 2.—Molecular motion under flow. *Journal of the Chemical Society, Faraday Transactions 2: Molecular and Chemical Physics* **1978**, *74*, 1802-1817.

(67) Landau, L. D. On the theory of phase transitions. *Ukr. J. Phys.* **1937**, *11*, 19-32.

(68) De Gennes, P. Short range order effects in the isotropic phase of nematics and cholesterics. *Molecular Crystals and Liquid Crystals* **1971**, *12*, 193-214.

(69) Wang, M.; Wang, W.; Zhang, Z. From the Q-Tensor Flow for the Liquid Crystal to the Harmonic Map Flow. *Archive for Rational Mechanics and Analysis* **2017**, *225*, 663-683.

(70) Tóth, G.; Denniston, C.; Yeomans, J. M. Hydrodynamics of Topological Defects in Nematic Liquid Crystals. *Physical Review Letters* **2002**, *88*, 105504.

(71) Noroozi, N.; Grecov, D.; Shafiei-Sabet, S. Estimation of viscosity coefficients and rheological functions of nanocrystalline cellulose aqueous suspensions. *Liquid Crystals* **2014**, *41*, 56-66.

(72) Kuzuu, N.; Doi, M. Constitutive Equation for Nematic Liquid Crystals under Weak Velocity Gradient Derived from a Molecular Kinetic Equation. *Journal of the Physical Society of Japan* **1983**, *52*, 3486-3494.

(73) Larson, R. G. On the relative magnitudes of viscous, elastic and texture stresses in liquid crystalline PBG solutions. *Rheologica Acta* **1996**, *35*, 150-159.

(74) Kuzuu, N.; Doi, M. Constitutive Equation for Nematic Liquid Crystals under Weak Velocity Gradient Derived from a Molecular Kinetic Equation. II.–Leslie Coefficients for Rodlike Polymers–. *Journal of the Physical Society of Japan* **1984**, *53*, 1031-1038.

(75) Ondris-Crawford, R.; Boyko, E. P.; Wagner, B. G.; Erdmann, J. H.; Žumer, S.; Doane, J. W. Microscope textures of nematic droplets in polymer dispersed liquid crystals. *Journal of Applied Physics* **1991**, *69*, 6380-6386.

(76) Bisoyi, H. K.; Kumar, S. Liquid-crystal nanoscience: an emerging avenue of soft self-assembly. *Chemical Society Reviews* **2011**, *40*, 306-319.

(77) Lekkerkerker, H. N. W.; Vroege, G. J. Liquid crystal phase transitions in suspensions of mineral colloids: new life from old roots. *Philos Trans A Math Phys Eng Sci* **2013**, *371*, 20120263.

(78) Shafiei-Sabet, S.; Hamad, W. Y.; Hatzikiriakos, S. G. Rheology of Nanocrystalline Cellulose Aqueous Suspensions. *Langmuir* **2012**, *28*, 17124-17133.

(79) Passantino, J. M.; Haywood, A. D.; Goswami, J.; Davis, V. A. Effects of Polymer Additives and Dispersion State on the Mechanical Properties of Cellulose Nanocrystal Films. *Macromolecular Materials and Engineering* **2017**, *302*, 1600351-n/a.

(80) Reising, A. B.; Moon, R. J.; Youngblood, J. P. Effect of particle alignment on mechanical properties of neat cellulose nanocrystal films. **2012**.

(81) Diaz, J. A.; Wu, X.; Martini, A.; Youngblood, J. P.; Moon, R. J. Thermal Expansion of Self-Organized and Shear-Oriented Cellulose Nanocrystal Films. *Biomacromolecules* **2013**, *14*, 2900-2908.

(82) Reising, A. R.; Moon, R.; Youngblood, J.: *Effect of particle alignment on mechanical properties of neat cellulose nanocrystal films*, 2012; Vol. 2.

(83) Chowdhury, R. A.; Clarkson, C.; Youngblood, J. Continuous roll-to-roll fabrication of transparent cellulose nanocrystal (CNC) coatings with controlled anisotropy. *Cellulose* **2018**.

(84) Park, J. H.; Noh, J.; Schütz, C.; Salazar-Alvarez, G.; Scalia, G.; Bergström, L.; Lagerwall, J. P. F. Macroscopic Control of Helix Orientation in Films Dried from Cholesteric Liquid-Crystalline Cellulose Nanocrystal Suspensions. *ChemPhysChem* **2014**, *15*, 1477-1484.

(85) Ličen, M.; Majaron, B.; Noh, J.; Schütz, C.; Bergström, L.; Lagerwall, J.; Drevenšek-Olenik, I. Correlation between structural properties and iridescent colors of cellulose nanocrystalline films. *Cellulose* **2016**, *23*, 3601-3609.

(86) Cranston, E. D.; Gray, D. G. Formation of cellulose-based electrostatic layer-by-layer films in a magnetic field. *Science and Technology of Advanced Materials* **2006**, *7*, 319-321.

(87) Dong, X. M.; Gray, D. G. Induced Circular Dichroism of Isotropic and Magnetically-Oriented Chiral Nematic Suspensions of Cellulose Crystallites. *Langmuir* **1997**, *13*, 3029-3034.

(88) Singh, A. P.; Rey, A. Microstructure constitutive equation for discotic nematic liquid crystalline materials. *Rheologica acta* **1998**, *37*, 30-45.

(89) Singh, A. P.; Rey, A. D. Computer simulation of dynamics and morphology of discotic mesophases in extensional flows. *Liquid Crystals* **1995**, *18*, 219-230.

(90) Singh, A. P.; Rey, A. D. Effect of long-range elasticity and boundary conditions on microstructural response of sheared discotic mesophases. *Journal of non-newtonian fluid mechanics* **2000**, *94*, 87-111.

(91) Tsuji, T.; Rey, A. D. Effect of long range order on sheared liquid crystalline materials Part 1: compatibility between tumbling behavior and fixed anchoring. *Journal of non-newtonian fluid mechanics* **1997**, *73*, 127-152.

(92) Cui, Z.; Calderer, M. C.; Wang, Q. Mesoscale structures in flows of weakly sheared cholesteric liquid crystal polymers. *DISCRETE AND CONTINUOUS DYNAMICAL SYSTEMS SERIES B* **2006**, *6*, 291.

(93) Venhaus, D. G.; Conatser, K. S.; Green, M. J. Dynamics of chiral liquid crystals under applied shear. *Liquid Crystals* **2013**, *40*, 846-853.

(94) Aguilar Gutierrez, O. F.; Rey, A. D. Biological plywood film formation from para-nematic liquid crystalline organization. *Soft Matter* **2017**, *13*, 8076-8088.

(95) Dong, X. M.; Gray, D. G. Effect of Counterions on Ordered Phase Formation in Suspensions of Charged Rodlike Cellulose Crystallites. *Langmuir* **1997**, *13*, 2404-2409.

(96) Dong, X. M.; Kimura, T.; Revol, J.-F.; Gray, D. G. Effects of ionic strength on the isotropic− chiral nematic phase transition of suspensions of cellulose crystallites. *Langmuir* **1996**, *12*, 2076-2082.

(97) Haywood, A. D.; Davis, V. A. Effects of liquid crystalline and shear alignment on the optical properties of cellulose nanocrystal films. *Cellulose* **2017**, *24*, 705-716.

(98) Ebeling, T.; Paillet, M.; Borsali, R.; Diat, O.; Dufresne, A.; Cavaillé, J. Y.; Chanzy, H. Shear-Induced Orientation Phenomena in Suspensions of Cellulose Microcrystals, Revealed by Small Angle X-ray Scattering. *Langmuir* **1999**, *15*, 6123-6126.

(99) Saha, P.; Ansari, N.; Kitchens, C. L.; Ashurst, W. R.; Davis, V. A. Microelectromechanical Systems from Aligned Cellulose Nanocrystal Films. *ACS Applied Materials & Interfaces* **2018**, *10*, 24116-24123.

(100) Schütz, C.; Agthe, M.; Fall, A. B.; Gordeyeva, K.; Guccini, V.; Salajkova, M.; Plivelic, T. s. S.; Lagerwall, J. P.; Salazar-Alvarez, G.; Bergström, L. Rod packing in chiral nematic cellulose nanocrystal dispersions studied by small-angle X-ray scattering and laser diffraction. *Langmuir* **2015**, *31*, 6507-6513.

(101) Shafiei-Sabet, S.; Hamad, W.; Hatzikiriakos, S. Ionic strength effects on the microstructure and shear rheology of cellulose nanocrystal suspensions. *Cellulose* **2014**, *21*, 3347-3359.

(102) Vermant, J.; Moldenaers, P.; Mewis, J.; Picken, S. Band formation upon cessation of flow in liquid-crystalline polymers. *Journal of rheology* **1994**, *38*, 1571-1589.

(103) Lonberg, F.; Fraden, S.; Hurd, A. J.; Meyer, R. E. Field-induced transient periodic structures in nematic liquid crystals: the twist-Fréedericksz transition. *Physical review letters* **1984**, *52*, 1903.

(104) Moon, R. J.; Martini, A.; Nairn, J.; Simonsen, J.; Youngblood, J. Cellulose nanomaterials review: structure, properties and nanocomposites. *Chemical Society Reviews* **2011**, *40*, 3941-3994.

(105) Beyene, D.; Chae, M.; Dai, J.; Danumah, C.; Tosto, F.; Demesa, A. G.; Bressler, D. C. Characterization of Cellulase-Treated Fibers and Resulting Cellulose Nanocrystals Generated through Acid Hydrolysis. *Materials (Basel)* **2018**, *11*, 1272.

(106) Saha, P.; Davis, V. A. Photonic Properties and Applications of Cellulose Nanocrystal Films with Planar Anchoring. *ACS Applied Nano Materials* **2018**, *1*, 2175-2183.

(107) de Vries, H.: *Rotatory Power and Other Optical Properties of Certain Liquid Crystals*, 1951; Vol. 4.

(108) John Wd, S.; J. Fritz, W.; J. Lu, Z.; Yang, D. K.: *Bragg reflection from cholesteric liquid crystals*, 1995; Vol. 51.

(109) Dumanli, A. G.; van der Kooij, H. M.; Kamita, G.; Reisner, E.; Baumberg, J. J.; Steiner, U.; Vignolini, S. Digital color in cellulose nanocrystal films. *ACS applied materials & interfaces* **2014**, *6*, 12302-12306.

(110) Wilts, B. D.; Dumanli, A. G.; Middleton, R.; Vukusic, P.; Vignolini, S. Invited Article: Chiral optics of helicoidal cellulose nanocrystal films. *APL Photonics* **2017**, *2*, 040801.

(111) Silvestre, N. M.; Pereira, M. C. F.; Bernardino, N. R.; da Gama, M. M. T. Wetting of cholesteric liquid crystals. *The European Physical Journal E* **2016**, *39*, 13.

(112) Dogic, Z.; Fraden, S. Cholesteric Phase in Virus Suspensions. *Langmuir* **2000**, *16*, 7820-7824.

(113) Kim, S.-J.; Kim, J.-H.: *The interaction of colloidal particles with weak homeotropic anchoring energy in homogeneous nematic liquid crystal cells*, 2014; Vol. 10.

(114) Dhara, S.; Madhusudana, N. V. Enhancement of the orientational order parameter of nematic liquid crystals in thin cells. *The European Physical Journal E* **2004**, *13*, 401-408.

(115) Stöhr, J.; Samant, M. G. Liquid crystal alignment by rubbed polymer surfaces: a microscopic bond orientation model. *Journal of Electron Spectroscopy and Related Phenomena* **1999**, *98-99*, 189-207.

(116) Croxton, C. A. A Landau-De Gennes Theory of the Nematic Liquid Crystal Surface. *Molecular Crystals and Liquid Crystals* **1981**, *66*, 223-240.